© Copyright by Rafik Borji 2010

All Rights Reserved

MODELING ULTRASOUND WAVE PROPAGATION FOR TISSUE CHARACTERIZATION

A Dissertation

Presented to

the Faculty of the Department of Mechanical Engineering

University of Houston

In Partial Fulfillment

of the Requirements for the Degree

Doctor of Philosophy

in Mechanical Engineering

by

Rafik Borji

December 2010

UMI Number: 3467014

All rights reserved

INFORMATION TO ALL USERS
The quality of this reproduction is dependent upon the quality of the copy submitted.

In the unlikely event that the author did not send a complete manuscript
and there are missing pages, these will be noted. Also, if material had to be removed,
a note will indicate the deletion.

UMI®
Dissertation Publishing

UMI 3467014
Copyright 2011 by ProQuest LLC.
All rights reserved. This edition of the work is protected against
unauthorized copying under Title 17, United States Code.

ProQuest®

ProQuest LLC
789 East Eisenhower Parkway
P.O. Box 1346
Ann Arbor, MI 48106-1346

MODELING ULTRASOUND WAVE PROPAGATION FOR TISSUE CHARACTERIZATION

Rafik Borji

Approved:

Chair of the Committee
Matthew A. Franchek, Professor,
Mechanical Engineering

Committee Members:

Karolos Grigoriadis, Professor,
Mechanical Engineering

Kirill Larin, Associate Professor,
Biomedical Engineering
and Mechanical Engineering

Ralph Metcalfe, Professor,
Mechanical Engineering

Leang-San Shieh, Professor,
Electrical and Computer
Engineering

Suresh K. Khator, Associate Dean,
Cullen College of Engineering

David Zimmerman, Professor
and Interim Chair,
Mechanical Engineering

Acknowledgments

First and foremost, all praises and thanks be to the one God (Allah) for His faithfulness and unconditional love as He led me perfectly to the completion of this work.

This research work would not have been possible without the support of many people.

First, I would like to express my gratitude to my supervisor, Dr. Matthew A. Franchek, who was abundantly helpful and offered invaluable assistance and support. He was not only the supervisor; he was also the friend and the supportive person in all stages of this work.

My deepest gratitude is also due to the members of the supervisory committee for their valuable feedback, especially in the defense.

I would like to dedicate all this work to my beloved mother and father, to my brothers and sisters.

With gratitude and love I would like to devote this dissertation to my dearly loved wife, her family and to my adorable son, Abdullah.

Special thanks also to all my friends who always have been there for me, especially Tunisian graduates at the University of Houston and Tunisian Houstonian friends at large.

MODELING ULTRASOUND WAVE PROPAGATION FOR TISSUE CHARACTERIZATION

An Abstract

of a

Dissertation

Presented to

the Faculty of the Department of Mechanical Engineering

University of Houston

In Partial Fulfillment

of the Requirements for the Degree

Doctor of Philosophy

in Mechanical Engineering

by

Rafik Borji

December 2010

Abstract

There is an unfilled need for new health prognostic methods and technologies with a real opportunity to integrate cost effective imaging methods with accurate health prognostics. By enhancing the capability of imaging methods to cover health prognostics, total cardiovascular disease (CVD) health care costs would be dramatically reduced and the quality of human life would be significantly improved. One clinically accepted cost effective CVD diagnostics method is the intravascular ultrasound (IVUS). State-of-the-art in ultrasound imaging, it is based on the reflection of ultrasound waves (frequencies up to 50 MHz) sent from the ultrasound transducer. Despite the wide use of IVUS as a primary tool for CVD diagnosis, especially in determining the plaque prone to form in the arterial wall, an objective plaque composition classification is not reached yet. Since this composition is fundamental to determine the degree of severity of the CVD, computational models have been developed to simulate the propagation and behavior of the ultrasonic waves inside the arterial wall.

This research seeks to develop computational model-based ultrasound imaging as a first step to enable CVD prognosis. Physics-based transmission line matrix (TLM) computational model is created where a fundamental understanding of ultrasound wave propagation in living tissue is captured. Moreover the ultrasound wave propagation through healthy and plaque burden (hard and soft plaque) segments is fundamentally understood and modeled.

The second primary step in this work is the development of advanced adaptive image recovery modeling techniques (time domain system identification techniques) that characterize the tissue properties. Plaque burden and composition (such as hard and soft plaque) within the artery wall are modeled using parametric techniques. The outcome from these computations is the assignment of traditional lumped parameter mechanical (tissue) elements (first order system) to artery composition detected from the ultrasound wave. These parameters are paramount in the determination of the plaque acoustic and

mechanical properties. These first order models have shown the ability of quantitatively characterizing different plaques based on their acoustic properties.

Table of contents

Acknowledgments v

Abstract vii

Table of contents ix

List of Figures xii

List of Tables xix

Chapter 1 Introduction 1

1.1. Motivation 2

1.2. Clinical needs 3

1.3. Overview of Intravascular Ultrasound 7

1.4. Objectives and Outline 12

Chapter 2 IVUS developments and modeling 14

2.1. IVUS clinical developments 14

2.2. Ultrasound wave propagation in biological tissue models 24

Chapter 3 Regular transmission line matrix (TLM) method and ultrasound propagation 33

3.1. Regular TLM Method 33

3.1.1. Introduction to TLM 34

3.1.2. One Dimensional Regular TLM 37

3.1.3. 1D TLM Model: 43

3.1.4. Two Dimensional Regular TLM 45

3.2. Analogy between EMF, Sound Waves and TLM 54

3.3. TLM model of the ultrasound propagation in tissues 58

3.3.1. IVUS regular TLM model 58

3.3.2. Model Validation: 64

3.3.3. Plaque model 65

3.4. Summary 71

Chapter 4 Irregular transmission line matrix model for intravascular ultrasound 72

4.1. Irregular TLM model Formulation 73

4.1.1. Governing Equations 73

4.1.2. Cartesian two-dimensional irregular TLM 76

4.1.3. Cylindrical Irregular TLM 81

4.1.4. Scattering and traveling processes of the irregular TLM 83

4.2. Irregular TLM validation 88

4.2.1. Sine Wave propagation 88

4.2.2. Ultrasound Wave Behavior against an obstacle 92

4.3. IVUS TLM model 96

4.3.1. Auto-generated mesh grid for the IVUS TLM model 97

4.3.2. IVUS TLM model for a healthy artery 100

4.3.3. IVUS TLM model for abnormal artery 103

4.4. Summary 106

Chapter 5 Tissue characterization using digital signal processing techniques 108

5.1. Introduction to system identification technique for an artery tissue 109

5.1.1. System identification overview 109

5.1.2. Arterial tissues and system identification 110

5.1.3. System identification process of the artery tissue components 113

5.2. Tissue characterization using regular and cylindrical irregular TLM models 118

5.2.1. Tissue characterization using regular TLM model 119

5.2.2. Tissue characterization using cylindrical irregular TLM model 127

5.3. Soft and hard plaque characterization: 131

5.4. Summary 133

Chapter 6 Conclusions 135

6.1. Contributions 136

6.2. Future work 137

References 138

List of Figures

Figure 1-1 Anatomy of normal coronary artery cross-section (http://commons.wikimedia.org/wiki/File:Anatomy_artery.png) 4

Figure 1-2 plaque build-up and partial blockage of the blood flow (http://www.healthfinder.gov/prevention/printtopic.aspx?topicid=27) 5

Figure 1-3 IVUS unit 8

Figure 1-4 Schematic if IVUS catheter (www.bostonscientific.com) 9

Figure 1-5 IVUS pullback sled (www.volcanocorp.com) 9

Figure 1-6 Imaged arterial wall by IVUS (http://www.bme.duke.edu/personal/friedman/research/images/) 10

Figure 1-7 Reflection and transmission on the ultrasound pulse at each boundary layer . 11

Figure 1-8 Calcified plaque characterized by a bright color with a shadow behind (http://campar.in.tum.de/Main/ArashTaki) 12

Figure 2-1 time domain and frequency domain patterns of the recorded echo for different plaques (NL: normal, FA: fatty, FF: fibro-fatty, FI: Fibrous and FC: fibrous with calcification)(7) 16

Figure 2-2 Integrated backscatter values for different plaque compositions (7) 17

Figure 2-3 Conventional IVUS images vs. color-coded maps constructed by IB IVUS (9) 18

Figure 2-4 (A) 3D color-coded maps of the arterial plaques using IB IVUS. (B) Assigned color map to each plaque type (10). 19

Figure 2-5 (a) RF echoes before and after compression; (b) cross-correlation function between the two RF waves (11). 20

Figure 2-6 Conventional IVUS image vs. constructed elastogram (upper images) and histological sections (lower images) (12). 20

Figure 2-7 Strain values of different plaques in femoral and coronary artery (13) 21

Figure 2-8 Spectral parameters computation from the RF echo frequency content (15) .. 22

Figure 2-9 Automated steps for tissue color-coded maps construction (15) 22

Figure 2-10 Comparison of IVUS images (left) vs. VH IVUS images (middle) and histology sections (right) (15) 23

Figure 2-11 Coordinate system for calculating the incident field (22) 31

Figure 3-1 A simple transmission line circuit between points x and x+Δx 34

Figure 3-2 Schematics of the Huygens principle for wave propagation (www.cliffsnotes.com) 35

Figure 3-3 Propagation in TLM model 35

Figure 3-4 TLM circuit between two nodes 35

Figure 3-5 Thevenin equivalent circuit 38

Figure 3-6 VTHand Req calculation 38

Figure 3-7 Lossless transmission line 39

Figure 3-8 Equivalent Thevenin Circuit 42

Figure 3-9 Lossy transmission line 42

Figure 3-10 a) Line segment b) TLM model based on Thevenin Equivalent circuit 43

Figure 3-11 Thevenin equivalent circuit for 1-D transmission line network 44

Figure 3-12 One-dimensional TLM scattering process 45

Figure 3-13 The series TLM node 47

Figure 3-14 Lines intersecting a single node 47

Figure 3-15 Discretization of the domain in a TLM mesh 48

Figure 3-16 Shunt TLM node 49

Figure 3-17 Shunt line for the propagation in the x direction 50

Figure 3-18 Shunt line for the propagation in the y direction 50

Figure 3-19 Thevenin equivalent circuit for the 4 lines intersecting in the ith node of the mesh 52

Figure 3-20 Thevenin equivalent circuit for the 4 lines intersecting the shunt node of the mesh 53

Figure 3-21 Rectangular approximation of a portion of the artery cross-section 58

Figure 3-22 Auto-generated mesh of 51 by 51 nodes 59

Figure 3-23 Boundary walls (red lines) terminating the rectangular medium 60

Figure 3-24 Reflection of the voltages (or sound waves pressure amplitudes) from the boundary walls 60

Figure 3-25 Examples of different source waves designed by SIMULINK 62

Figure 3-26 Traveling process of the wave between the nodes 63

Figure 3-27 Validation model of the regular TLM 64

Figure 3-28 Generated waves for different locations of the medium 65

Figure 3-29 Validation of the results for the developed TLM code versus an established literature model 65

Figure 3-30 Plaque in the artery (http://yoursurgery.com) 66

Figure 3-31 Structure of the TLM model where a plaque is inserted 67

Figure 3-32 Reflection and transmission of the wave at the four edges of the plaque 68

Figure 3-33 Plaque example generated by the developed 2-D TLM model 69

Figure 3-34 plaque effect on the signals at different locations ($ZHardinclusion = 7.4ZHealthyartery$ and $ZSoftinclusion = 0.074ZHealthyartery$) 70

Figure 3-35 Comparison of the time signals ($ZHardinclusion = 7.4ZHealthyartery$ and $ZSoftinclusion = 0.074ZHealthyartery$) 70

Figure 4-1 Irregularly spaced element 73

Figure 4-2 Time synchronism of the traveling process (T is constant) 76

Figure 4-3 Stub represented by a new line added to the mesh at each node 80

Figure 4-4 Circular geometry of the artery cross-section 81

Figure 4-5 Irregular structure of a circular element of the cylindrical TLM model 81

Figure 4-6 Added stub line to a circular element 82

Figure 4-7 Shunt node for irregular Cartesian TLM 83

Figure 4-8 Lines intersecting an arbitrary node of irregularly spaced mesh 84

Figure 4-9 Thevenin equivalent circuit for the 5 lines intersecting an arbitrary node of the irregular mesh 84

Figure 4-10 Scattering process of the voltages 86

Figure 4-11 Traveling process in irregular Cartesian TLM mesh 86

Figure 4-12 Traveling process in cylindrical TLM mesh 87

Figure 4-13 Generated regular model by conventional regular TLM 89

Figure 4-14 Sine wave propagation from the center of the medium (picture taken every three sample times) 89

Figure 4-15 Sine wave propagation in the irregular mesh (picture taken every three time samples) 90

Figure 4-16 Propagation of the sine wave using the irregular Cartesian TLM model (picture taken every three time samples) 91
Figure 4-17 A 100 by 100 nodes rectangular medium created by irregular cylindrical TLM 91
Figure 4-18 Simulated sine wave propagation in the irregular cylindrical TLM model (picture taken every three time samples) 92
Figure 4-19 Medium composed of 200 by 100 nodes 93
Figure 4-20 Wave propagation and behavior of the sound wave against a totally reflective obstacle. 93
Figure 4-21 Ultrasound wave propagation and behavior against a totally reflective obstacle using irregular Cartesian TLM (pictures are taken every five time samples) .. 94
Figure 4-22 Ultrasound wave propagation and behavior against a totally reflective obstacle using irregular cylindrical TLM (pictures are taken every five time samples) 95
Figure 4-23 Rectangular medium construction using cylindrical TLM model 96
Figure 4-24 Conic propagation of the sent wave through the circular medium 98
Figure 4-25 Angular direction of the propagation of the wave 98
Figure 4-26 Impedance ratio function of the radial position 99
Figure 4-27 Propagation of the wave in radial direction with a conic shape 100
Figure 4-28 Boundary termination of the modeled artery cross-section 101
Figure 4-29 Snapshots of the spatial distribution of the wave amplitudes on the artery cross-section (pictures taken every 8 time samples) 102
Figure 4-30 Time signals record of the wave propagation at different locations 103

Figure 4-31 Inclusion inserted in the circular medium between the 70th and 130th angular nodes and 20th and 30th radial nodes 104

Figure 4-32 Common edges between the healthy artery (blue region) and the inclusion (red region) 104

Figure 4-33 Reflection/transmission of the wave components between the inclusion and the artery 105

Figure 4-34 Time signals record of the wave propagation at different locations having different inclusion 106

Figure 5-1 Dynamic system characterized by an input signal, an output response and a disturbance term 109

Figure 5-2 Schematic of the different steps for system identification 110

Figure 5-3 Input and output signals to a portion of a soft tissue 111

Figure 5-4 System identification approach applied to the plaque portion using regular TLM model 112

Figure 5-5 System identification approach applied to the plaque using cylindrical irregular TLM model 112

Figure 5-6 a) Swept sine signal, b) Swept sine power spectrum 114

Figure 5-7 Swept sine signal where the frequency range is between $\lfloor 10^4, 10^7 \rfloor Hz$ 114

Figure 5-8 Constructed swept sine pulse 115

Figure 5-9 Flowchart of the orthogonal least squares method 117

Figure 5-10 Plaque inserted in the regular medium 119

Figure 5-11 Input signal to healthy plaque that has a delay of 10 time samples 120

Figure 5-12 Output signal to healthy plaque that has a delay of 30 time samples 120

Figure 5-13 Preprocessing of the input and output signals to the plaque 121

Figure 5-14 model and actual outputs for a healthy tissue 122

Figure 5-15 Error histogram between the model output and the actual output 122

Figure 5-16 Plaque inserted in the circular irregular medium and transformed to a rectangular medium 127

Figure 5-17 Plaque inserted in the circular irregular medium 128

Figure 5-18 Reflection/transmission across the plaque edges 128

Figure 5-19 RL low pass filter 132

List of Tables

Table 3-1 Analogy between EMF and Sound waves parameters 55

Table 3-2 Analogy between EMF and TL parameters 57

Table 4-1 Analogy between EMF and TL parameters 75

Table 5-1 DC gain variation as function of the acoustic impedance of the plaque (regular TLM model) 125

Table 5-2 Time constant variation as function of the acoustic impedance of the plaque (regular TLM model) 126

Table 5-3 DC gain variation in percentage (regular TLM model) 126

Table 5-4 Time constant variation in percentage (regular TLM model) 126

Table 5-5 DC gain variation as function of the acoustic impedance of the plaque (cylindrical irregular TLM model) 129

Table 5-6 Pole location variation as function of the acoustic impedance of the plaque (cylindrical irregular TLM model) 130

Table 5-7 DC gain variation in percentage (cylindrical irregular TLM model) 130

Table 5-8 Time constant variation in percentage (cylindrical irregular TLM model) 131

Table 5-9 Model coefficients variation as function of the plaque type (regular TLM model) 131

Table 5-10 Model coefficients variation as function of the plaque type (cylindrical irregular TLM model) 131

Chapter 1 Introduction

One of the leading mortal diseases is Cardiovascular Disease (CVD). According to the World Health Organization (WHO) reports in 2001, 16.7 million human death situations occur in the world due to CVD each year. This number accounts for one third of the total deaths. These high-count statistics are more important in the United States. Since 1900, CVD has been the number one killer for every year but 1918 (1,2). With a daily rate of death exceeding 2,500, 27% of them happen before reaching the hospital. The continuous increase of heart attack deaths and hospitalization has led scientists and medical specialists to work on finding ways of an early assessment of such pathological phenomenon.

Therefore advanced imaging techniques have seen the light due to numerous efforts aiming at the development of a preventive diagnosis methodology of coronary arteries before plaque aggravation and advanced stenosis development. Two major categories of these imaging methods were established which are invasive and non-invasive technologies. Despite the convenience of the non-invasive techniques to the patient, many challenges can take place (in the scanning process) especially when it comes to cardiac motion as well as calcium deposits. To tackle such limitations, many invasive imaging devices were developed. One of the recent invasive imaging methods is the intravascular ultrasound (IVUS).

IVUS has gained a wide clinical acceptance. Thanks to its ability of providing quantitative and qualitative information on the structure of the artery cross-section, IVUS presents one of the essential tools used for CVD identification. With IVUS all the artery components can be visualized including arterial narrowing, calcium deposits and evaluation of aneurysms. This information is acquired based on the recorded back-scattered radio-frequency waves where the variation in the amplitudes determines the acoustic characteristics of each layer in the artery.

Despite the great amount of useful information offered by this imaging modality, there still is no clear and quantitative classification of all the plaques that could form in

the artery. Since the composition, the size and the mechanical properties of each plaque is essential for assessing the degree of severity of the CVD, it is important to have a more detailed and accurate classification of these plaques. One effective way for classification purposes is to study theoretically the behavior and propagation of the ultrasound inside the artery cross-section. Unfortunately an analytical solution for the sound wave equation could not be obtained due to the complexity of these structures (irregular shape, different mechanical and acoustic properties). Consequently numerical techniques have been adopted as an alternative to solve for these cases of wave propagation equations. Within this context, the development of a multi-domain computational model has been driven. This work has been motivated by the need of a meticulous investigation on the behavior of the ultrasound waves against a wide range of plaques.

This introductory chapter will be divided into four main parts. Motivational factors for the development of computational model based ultrasound imaging will first be enumerated. In the second part clinical needs of the imaging modality of coronary artery will be developed. After that an overview on intravascular ultrasound will be detailed. In the last part objectives and the outline of the dissertation will be presented.

1.1. Motivation

The reported yearly worldwide death tolls and especially in the US about cardio-vascular disease is the leading factor that motivated scientists to invest time and money in order to find innovative ways that enable accurate and early detection of such diseases. Since CVD occurs within the human body, imaging modalities were invented to present a picture of the artery as close as possible to its real status. These imaging methods accompanied with continuous developments have helped tremendously in the improvement of proactive health care and early interventions before aggravations. Intravascular Ultrasound is one of the modalities that have been extensively used for diagnostics purposes. Although IVUS has the advantage of differentiating between all the artery cross-section components in terms of geometry, the composition and mechanical properties of each component is still a subject of discussion and research. In fact, an objective classification of plaques based on both mechanical and acoustic properties is not reached yet. For instance, echogenicity of luminal tissue in most cases is the same for

a plaque composed of high lipid depositions. Thus ultrasound wave propagation and transmission should be studied fundamentally in the human tissues and specifically through the artery cross-sections. The only way these ultrasonic waves could be studied meticulously is by solving the propagation governing equations, i.e., through the wave equation. Finding the analytical solution of these waves contributes definitely in understanding the propagation fashion and behavior inside the medium. Finding analytical solution of the wave equation is highly dependent on the medium. In the case of artery cross-section in a human body, there exist numerous geometric irregularities. These irregular shaped components of the artery make the wave equation unsolvable analytically. Consequently numerical methods are employed to find discrete solutions of the ultrasound waves.

Motivated by establishing a robust computational model for ultrasound propagation, physics-based transmission line matrix (TLM) method was developed and adapted to the medium of interest (1). The multi-domain nature of this model provides both temporal and spatial information about the waves that are propagating in the designated medium. This type of information will allow a detailed study of the behavior of the ultrasound waves in different locations, mechanical and acoustic properties. Moreover the ultrasound wave propagation through healthy and plaque burden (hard and soft plaque) segments will be fundamentally understood and modeled. Plaque burden and composition within the artery wall will be modeled using parametric techniques. Many issues associated with IVUS including signal scattering due to blood flow and sensor noise will be addressed. The outcome from these computations is the assignment of traditional lumped parameter mechanical (tissue) elements such as mass, stiffness and damping to artery composition detected from the ultrasound wave. Hence ***quantifiable parameters*** will be associated with different compositions and properties of each artery wall segment.

1.2. Clinical needs

There is an unfilled need for new health prognostic methods and technologies with a real opportunity to integrate cost effective imaging methods with accurate health prognostics. By enhancing the capability of imaging methods to cover health

prognostics, total CVD health care costs would be dramatically reduced and the quality of human life would be significantly improved. This early detection allows for proactive health care through diet, exercise and pharmaceuticals thereby extend the quality of life for people. One clinically accepted cost effective CVD diagnostics methods is the intravascular ultrasound (4,5).

A CVD event occurs when coronary artery is facing an abnormal transformation. This abnormal configuration that occurs in the artery is known as plaque formation. Normally a healthy artery is composed of three concentric main components; the inner wall of the artery which is known as the intima is connected to the lumen of the artery (interior space of the artery). The outer layer of the artery called the adventitia is responsible for the stability and connection to the organs surrounding the artery. The layer in-between which is known as the media is composed of smooth muscle cells. Figure 1-1 describes the different components of the arterial wall.

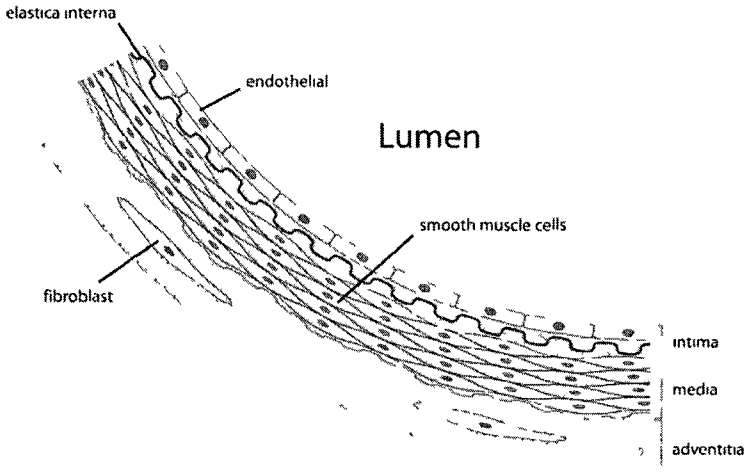

Figure 1-1 Anatomy of normal coronary artery cross-section
(http://commons.wikimedia.org/wiki/File·Anatomy_artery.png)

Any build-ups that form in the artery may lead to coronary events. These build-ups or accumulations are accompanied with a thickening and hardening of the arterial wall known as ***atherosclerosis***. This atherosclerosis is caused by the formation of what is called ***plaques*** within the arteries. The term ***plaque*** was attributed to the material that is

formed by the fat, fibrous tissue, calcified debris and other substances. This is created by the transport occurring in the bloodstream. These transported materials start to adhere on the artery walls thereby forming these plaques. Depending on the size and composition of these plaques, this atherosclerosis may cause partial or total blockage of blood flow nourishing the heart. Shown in Figure 1-2 in the second artery is a plaque, and how plaque could block partially the blood flow.

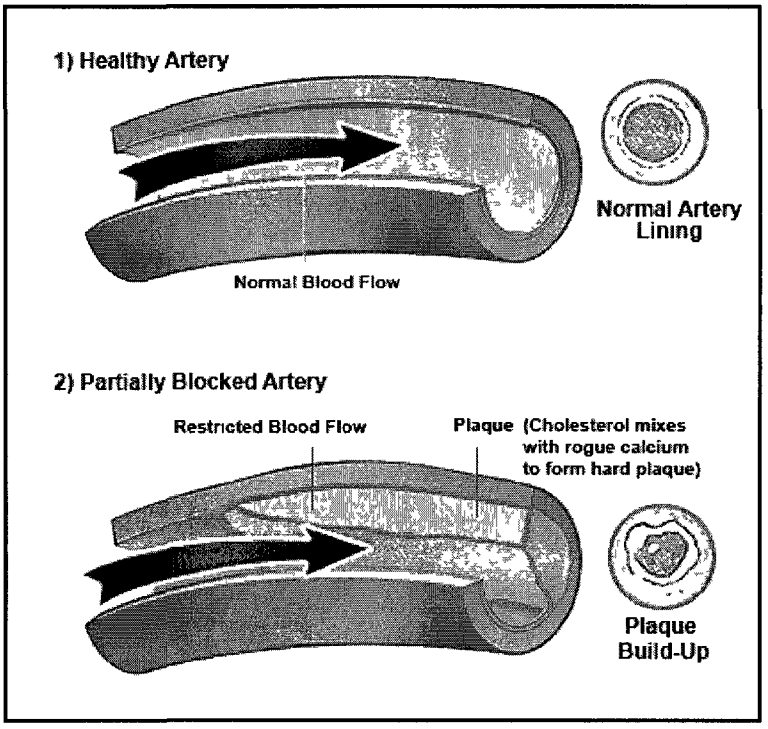

Figure 1-2 plaque build-up and partial blockage of the blood flow
(http://www.healthfinder.gov/prevention/printtopic.aspx?topicid=27)

IVUS has shown its ability of visualizing the full and detailed geometry of the artery cross-section (artery wall) at any given position of the artery. Since then, IVUS was employed as an adjunct tool to angiography. The development and continuous use of this imaging modality, has led scientists in the medical field to gain an increasing knowledge about the plaque characterization. IVUS was first used as a complimentary tool for diagnostics purposes of the artery along with angiography. Its diagnostics role was extended to interventional applications due to the useful and accurate information offered by this modality. Therefore its clinical use has become necessary for CVD patients.

IVUS showed a notable advantage compared to angiography. Numerous studies have recorded the ability of IVUS to detect occult disease in suspected arteries undetectable by angiography. Moreover an accurate tomography of lesions is obtained via IVUS whereas some types of lesions are indeterminate for angiography. IVUS diagnosis of the diseased transplanted coronary artery has shown its ability of detecting intimal thickening in its first stage in opposition to angiography (angiography captures 10% to 20% of the thickening in patients in the first year whereas IVUS detects 50% of the patients with such thickening). In addition to that, intravascular ultrasound identifies atheromas at risk of rupture.

Interventional applications of IVUS have also touched numerous aspects. In fact ultrasound has been utilized for device selection in the interventional process. Knowledge generated by IVUS on the lesions' size and composition had helped to make decisions on the choice of suitable intervention devices. IVUS also played an important role in using angioplasty and atherectomy. Angioplasty is the technique of widening narrowed arteries by inserting a wire-guided balloon that is inflated in the region to be treated. Using ultrasound for plaque visualization before and after angioplasty intervention has changed direct plaque compression approach to axial distribution and vessel wall stretching to regain wider lumen configuration. With regard to atherectomy (surgical method for plaque removal), IVUS has facilitated the lesions selection in terms of composition specifically calcified regions. Ultrasound has been also employed for stent therapy (artificial tube insertion inside the artery) guidance in terms of assisting pressure dilatation for expansion purposes. Restenosis has also been monitored by IVUS after stent intervention.

IVUS has shown its usefulness as a tool for both diagnostic and intervention purposes. Its clinical need has grown and become necessary in the last decades due to the IVUS equipments improvement that was accompanied with a better precision and robustness. Safety and cost effectiveness of this imaging method are also promoting factors which contributed to its clinical wide use.[1]

[1] References for the clinical needs regarding diagnostics and interventions are detailed in Chapter 2.

1.3. Overview of Intravascular Ultrasound

Intravascular Ultrasound is an imaging method that uses ultrasound waves to image coronary arteries from the lumen for atherosclerotic disease identification purposes. Ultrasound waves are characterized by frequency that is higher than what is heard by humans. Every sound wave that has a frequency larger than 20 KHz is considered as ultrasonic. Ultrasound waves are mechanical and longitudinal that cause particles to oscillate producing compressions and rarefactions. Numerous studies have shown that these waves are safe and do not cause any harm for living cells and tissues.

The idea of detecting different components of the arterial wall came from the properties of the ultrasound waves. In fact, this detection is highly related to the size of the object to be imaged and the wave length. These waves are characterized by the velocity or speed of the wave c, the frequency f and the wavelength λ. These parameters are related by

$$c = \lambda f. \tag{1-1}$$

Since the objects of interest have small sizes (components inside the artery), the ultrasound wave length should be smaller than these components sizes. From equation (1-1) the wavelength and frequency are inversely proportional. Therefore high frequencies will lead to small wavelengths. The higher the frequency the better the resolution is. Despite the high resolution of high frequency waves, the penetration depth is reduced. Ultimately what is recovered from IVUS is an estimated image of the artery cross-section not a characterization of the artery tissue properties. Generally the frequency range of IVUS is between 10 and 50 MHz.

In IVUS, ultrasound is generated by the transducer. These transducers produce ultrasound waves and at the same time detect the sound reflected back from the scanned areas of interest. The central feature of the transducer is the piezoelectric crystal. This crystal is characterized by its ability of converting electrical energy to mechanical energy and vice-versa. In fact an alternating current applied to the piezoelectric crystal causes this piece to bend back and forth producing a mechanical movement (known as piezoelectric effect). This mechanical movement will create a pressure difference that is

the origin of the ultrasonic wave. The same thing applies for the backscattered ultrasound wave. When this wave encounters the piezoelectric crystal, the latter starts to grow and shrink. This movement of the crystal produces a mechanical energy that is converted into electrical energy. This electrical-energy wave form is related to what is reflected back from the different components of the imaged arterial wall.

The way that IVUS images the interior of the arterial wall is by miniaturizing this transducer to a size where it can be inserted in the coronary artery. This tiny transducer is mounted on the tip of a flexible catheter (diameter usually equals 0.36mm). These IVUS catheters are inserted in the femoral artery and then guided to the coronary arteries. Once the equipment is placed in the region of interest, the transducer starts to emit ultrasound waves and receive echoes, respectively. The transducer has the capability of rotating with a fixed speed (usually 1800 rpm) in order to sweep all the artery cross-section. IVUS can also generate a longitudinal view of the vessel by using a pullback sled that makes the catheter move at a fixed and slow speed (0.5mm/sec).

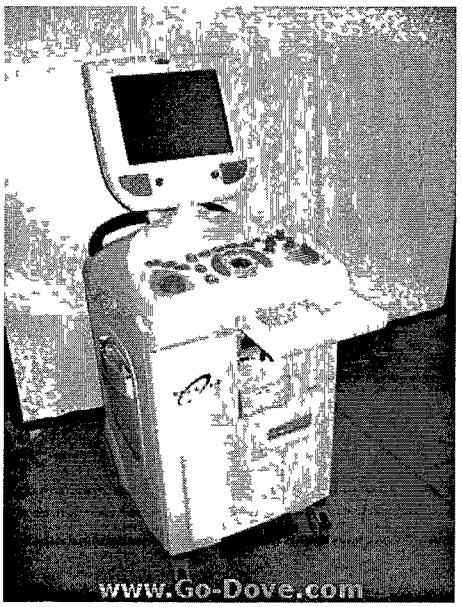

Figure 1-3 IVUS unit

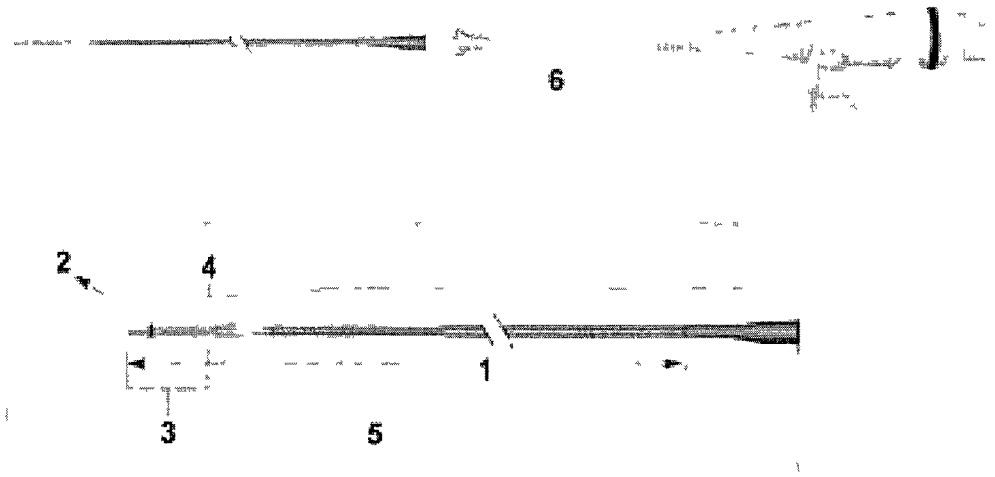

1 135 cm usable length
2. Marker band 2 5F
3. 1 5 cm guide wire rail length
4. 2 1 cm marker band to transducer
5. Imaging window profile 3.2F
6. 15 cm imaging core pullback

Figure 1-4 Schematic if IVUS catheter (www.bostonscientific.com)

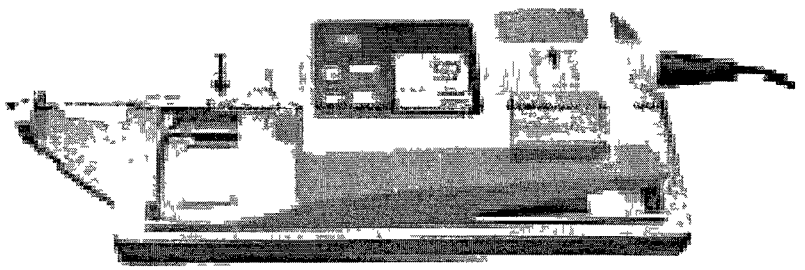

Figure 1-5 IVUS pullback sled (www.volcanocorp.com)

Shown in Figure 1-3, Figure 1-4 and Figure 1-5 are the different components of the IVUS system. A cross-section image is recovered from IVUS and can be seen directly on the screen of the IVUS system in Figure 1-3. Figure 1-6 illustrates an image that is recovered from IVUS for an artery cross-section.

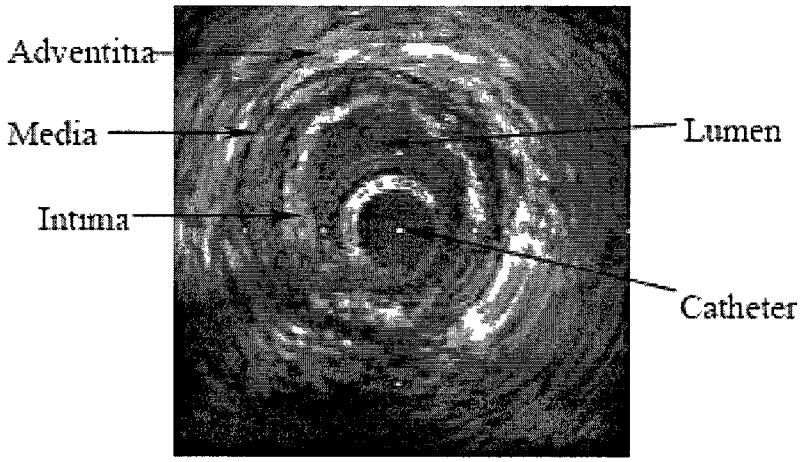

Figure 1-6 Imaged arterial wall by IVUS
(http://www.bme.duke.edu/personal/friedman/research/images/)

The above image is recovered based on the change in acoustic properties of each layer or component of this arterial wall. The initiated sound wave (pulse) travels through the tissue until a boundary layer is encountered. At this interface, part of the sound wave is reflected back toward the transducer while the remaining part of the signal continues to travel outward toward the next tissue interface. The reflected wave is sensed by the IVUS tip and changed into an electrical signal. The amount of time, denoted by t, between the emitted signal and the reflected signal is used to determine an approximate radial location of the tissue interface. Specifically, the speed of sound within a tissue is approximately *1,540 m/sec*. Thus, the approximate distance of the sensed tissue interface is $d=(1{,}540\ m/s)*t$. See Figure 1-7 where the Z variables denote acoustic impedance.

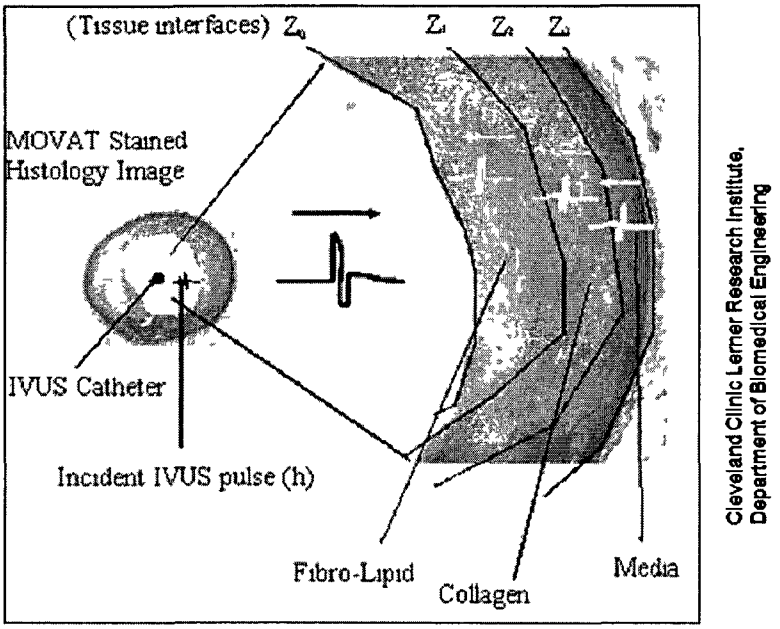

Figure 1-7 Reflection and transmission on the ultrasound pulse at each boundary layer

The *gray-scale* picture associated IVUS images (also shown in Figure 1-7) are based on the reflected signal intensity. As the sound wave propagates through the tissue and is reflected, the intensity of the pulse (amplitude) returning to the IVUS tip is attenuated. The amount of attenuation relative to the initial pulse size is used to determine its gray-scale color. The gray scale range is from light to dark. The denser the tissue matter, the lighter the gray scale. Hence the overall IVUS image has a gray scale image that is spatially located (pixel location on the screen) based on the approximate interface location estimated above. For example, calcification that occurs in the arterial wall or heavy calcium deposits is characterized by a high reflection effect due to their high density. Consequently the reflected ultrasound wave component is predominant compared to the transmitted wave. This is why in the IVUS image a brighter color is assigned to the backscattered wave of a calcified area with shadows behind the calcified region as the transmitted wave is negligible. See Figure 1-8.

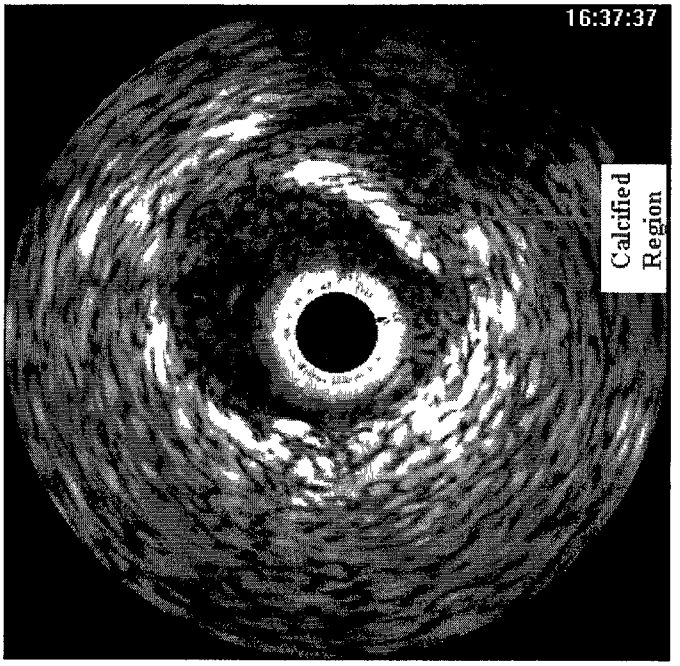

Figure 1-8 Calcified plaque characterized by a bright color with a shadow behind (http://campar.in.tum.de/Main/ArashTaki)

1.4. Objectives and Outline

The ultimate objective of this dissertation is to study the dynamic response of the arterial wall to ultrasound excitation, specifically the dynamics of the plaque. Parametric models of these atherosclerotic formations will be derived and linked to the mechanical and acoustic properties of these plaques. The identification techniques used to construct these models necessitate time signature of the ultrasound waves. Therefore, a multi-domain (temporal and spatial) physics based computational model for IVUS is developed. This model will be considered as a source to collect ultrasound data in a simulated fashion. This data will be used to recover a parametric model for each plaque where its coefficients are highly correlated to the dynamics of this plaque. These models will be of a great importance in terms of identifying the nature of the plaque. In fact, the value of the model coefficients will be mapped to each plaque composition.

This dissertation will be divided into 6 main chapters. In chapter 1, the motivation, the clinical need, an overview about the IVUS and the outline are developed. Chapter 2 contains two parts. The latest developments in IVUS will be first detailed. Then a review on IVUS modeling will be given. Chapter 3 details the foundation of the computational

method (Transmission Line Matrix Method) that is used to model IVUS in a simple regular medium (rectangular shape). Chapter 4 is dedicated to a new Transmission Line Matrix model for the IVUS in an irregular shape (circular shape to model the artery cross-section). Chapter 5 gives the system identification methodology used to construct a parametric model that characterizes a plaque for specific mechanical and acoustic properties. Chapter 6 is devoted to the conclusions and future directions in the research work.

Chapter 2 IVUS developments and modeling

Intravascular Ultrasound is a technique that was patented in the early seventies and has been introduced for clinical use in the late eighties. Since its first use, IVUS has undergone considerable developments. Starting as a diagnostics complementary tool to angiography, it has gained more importance clinically. In fact IVUS has shown its ability of imaging tomographically the arterial wall. Since then, the clinical use has evolved from geometric structure imaging to assessment of atherosclerotic plaque areas and even plaque composition to a certain extent. Clinical interventions have also been developed using IVUS for treatments of plaques.

On the other hand, along with these clinical developments, efforts have been put to understand analytically the ultrasound behavior in biological tissues. Many ultrasound models have been constructed to capture the ultrasound propagation in these tissues. The ultimate goal behind constructing these models is to study physically and analytically ultrasound waves behavior towards various components of the biological tissues and specifically the arterial wall components including atherosclerotic formations.

Fusing both experimental data from IVUS and developed numerical models of ultrasound waves inside the arterial wall will form a solid and robust ground for understanding and characterizing the mechanical and acoustic properties of each arterial wall component including all the formations and plaques that are prone to develop.

This chapter will be divided into two main parts. Developments of IVUS in diagnostics applications will be first enumerated. The ultrasound wave propagation modeling in biological tissues and in IVUS specifically will then be developed.

2.1. IVUS clinical developments

Based on the transmission and the reception of ultrasound waves (high frequency waves) (6,7), IVUS was proven to be a powerful method by which the scanning process can reach deep structures of the artery. Its extensive use in the biomedical field comes from its ability to visualize the cross-section of the artery by which both plaque and different layers can be evaluated. In addition to that, IVUS images provide a huge variety

of qualitative information such as the severity of the arterial narrowing, the recognition of calcium deposits, and the evaluation and diagnosis of the arterial aneurysms as well as fissures (this characterization includes the location, dimensions, type and composition).

IVUS was first used in the 1990s as a supplementary tool to angiography for the examination of coronary arteries. Angiography was the most predominant technique used for more than 50 years to characterize coronary anatomy. This technique provides angiograms which are planar projections of the arteries. These projections can lead to a misrepresentation of the real irregularities in the artery. These discrepancies between angiograms and post-mortem findings have been demonstrated in numerous studies (2). IVUS with its inherent characteristics mentioned previously gave insights in evaluating coronary disease and became increasingly an essential tool for artery diagnosis.

The concept of vulnerable plaques was introduced, to refer to a subgroup of stenotic plaques that are prone to rupture or erosion (3). These rupture-prone plaques have specific characteristics: a thin fibrous cap, a large lipid-rich pool and an increased macrophage activity (4). The use of IVUS for the detection of the vulnerable plaques has provided insight into the extent and distribution of these atherosclerotic plaques, precisely the characterization of vessel wall and plaque morphology (5).

Since the composition of the arterial plaque is the most determinant factor of the CVD severity, a continuous focus was spent on tissue characterization via IVUS imaging. Extensive use of IVUS by clinicians during the last decades has shown some difficulties and discrepancies in classifying the plaque composition. For example, the grayscale IVUS images are unable to distinguish accurately among plaque components such as fibrous tissue, fibro-fatty tissue and various stages of thrombus (12-14). IVUS also underestimates the total calcified plaque cross-sectional area as well as the depth of calcium (6).

The inability of discriminating most of the plaque types from the grayscale images, has enhanced researchers to think about the content and information that the backscattered radio-frequency (RF) ultrasound waves could offer. As illustrated in Figure 2-1, RF signals possess valuable information in terms of plaque composition. It can be

seen that there is a difference between these RF echoes coming from various plaque types.

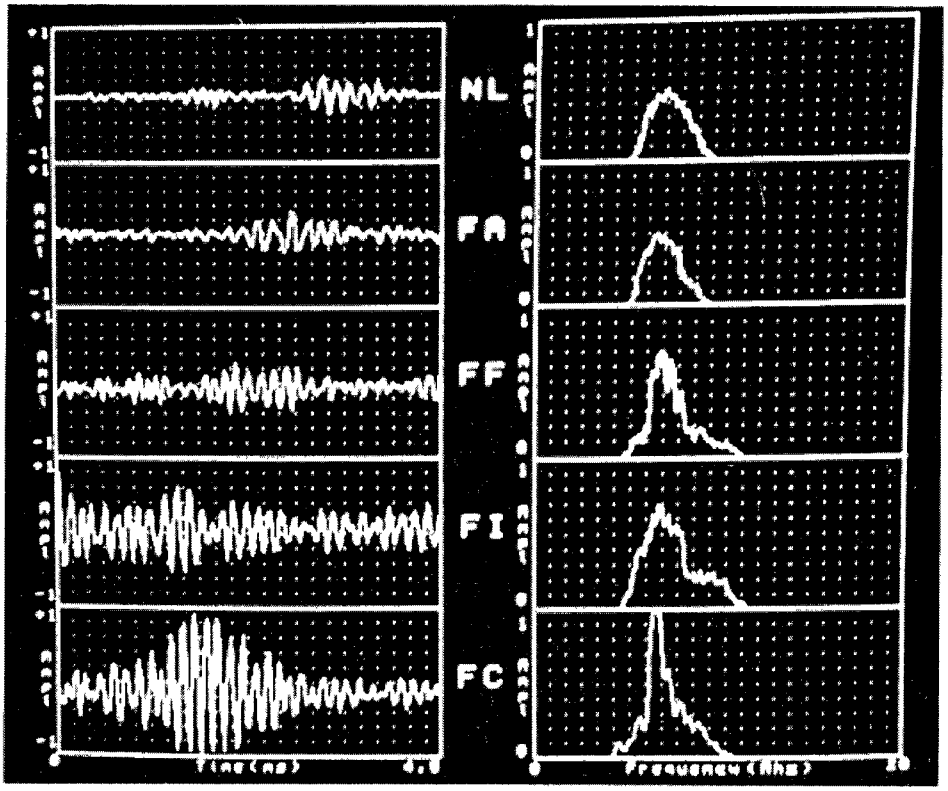

Figure 2-1 time domain and frequency domain patterns of the recorded echo for different plaques (NL: normal, FA: fatty, FF: fibro-fatty, FI: Fibrous and FC: fibrous with calcification)(7)

Numerous investigations have been conducted in a first phase with ultrasound transducers characterized by a relatively low frequency (7 to 15 MHz) (16-22). What is called integrated backscatter IVUS (IB IVUS) was introduced. In fact each collected RF signal corresponds to the two dimensional selected region of interest (ROI). This signal is first digitized. After that what is called 2-D integrated backscatter (IB) index is calculated based on these digital signals (7). Finally a mean IB value is recovered through the ratio of the IB value by the number of pixels composing the imaged ROI, i.e. $V = IB/NP$ (NP is the number of pixels). This IB is expressed in decibels by $IBD = 20log10(V/V_r)$, where V_r is an IB value of a chosen reference reflection.

Values of Integrated Backscatter Index in Different Plaques

Subset	No. of Observations	Integrated Backscatter, dB (mean±SD)
Intraluminal thrombosis	5	−42±5.1
Fatty	11	−40.3±5.4
Fibrous	12	−23.8±5.0
Calcified	26	−11.5±5.2

Figure 2-2 Integrated backscatter values for different plaque compositions (7)

Shown in Figure 2-2 is the different IB values in decibels for the plaques. IB IVUS has shown its ability to differentiate between fatty, fibrous and calcified plaques. Nevertheless most of the conducted studies were limited to the narrow frequency band which affects the RF echoes in terms of phase cancellation and fluctuations of the IB due to the heterogeneity property of the tissue. Additionally these results are highly affected by the distortion and the deformation of the plaque.

With the introduction of high frequency transducers that could reach up to 40MHz, investigations on plaque characterization using IV has been carried out over again. The use of IB IVUS has in fact shown its capability of detecting lipid core which is one of the major factors of vulnerable plaque. In fact one of the investigations has shown that IB in the group with lipid core is greater than the one without lipid core (increase in the IB of 6.22%) (8). Although this method has detected the lipid core component, this experimental process was presenting a major limitation. In fact the cardiac and transducer motions influence highly the measured RF ultrasonic echoes which affect directly the calculated IB values.

IB IVUS has been extended to a broader quantitative characterization of coronary plaques (9). In fact RF content has been stored directly without image visualization. After that the IB calculation step is performed. Then color-coded maps were constructed based in the calculated IB values for each plaque type. Finally a comparison between the constructed color-coded images and the B-mode IVUS cross-section images has revealed

a perfect agreement in the structure characterization (9). Shown in Figure 2-3 is a comparison between IVUS images and reconstructed images based on IB.

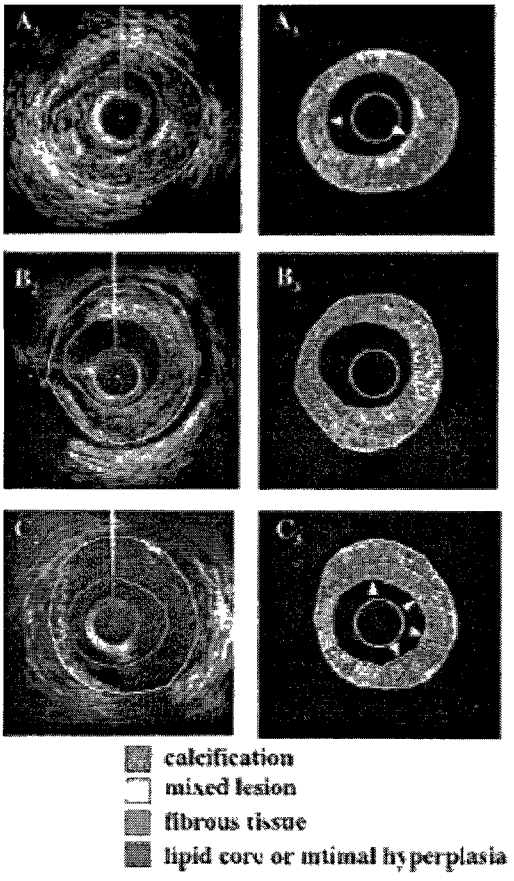

Figure 2-3 Conventional IVUS images vs. color-coded maps constructed by IB IVUS (9)

Despite the accurate differentiation between all plaque types (calcification, mixed lesion, fibrous tissue, lipid core and thrombus), the angle dependency between ROI's and catheter axis makes this classification unstable and sensitive. Moreover the high resolution dictated for plaque detection necessitates high frequency ultrasound signals which affect the penetration depth of these transmitted ultrasonic pulses.

Some of the researchers have extended the use of the IB IVUS to three-dimensional reconstruction by using available software. This 3D reconstruction is characterized by color-coded maps that are found by IB where each color refers to a certain plaque composition (10). Illustrated in Figure 2-4 are 3D color-coded maps of arterial plaques.

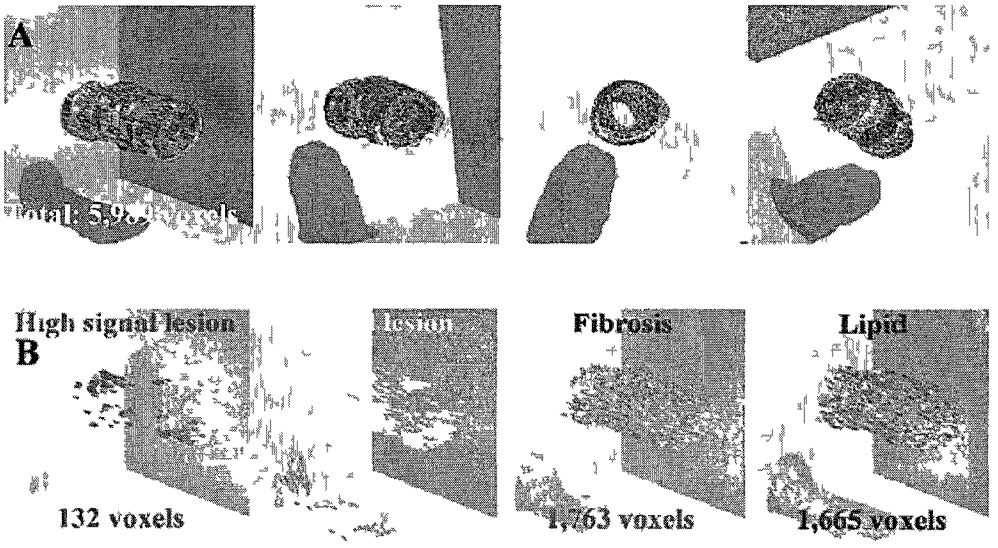

Figure 2-4 (A) 3D color-coded maps of the arterial plaques using IB IVUS (B) Assigned color map to each plaque type (10)

Limitation of this study lies into two main factors. First the 3D images are not a true spatial reconstruction of the plaque geometry but simply a connection of consecutive IB IVUS images captured using motorized pull-back system. Second the reflective property of calcified region makes the calculation of its volume inaccurate.

In addition to the use of IB as a determinant parameter by which plaques were classified, new research directions has been inspired from the elastic property that could characterize each plaque type. This gave rise to what is called **intravascular elastography** (also known as **IVUS elastography**) In fact, investigators have taken advantage of the possibility of recording the RF echoes to use them for displacements or strain determination. The procedure is composed of four main steps (11). First a set of RF ultrasonic waves (A-lines) was acquired. Second, compression was applied to the ROI of the tissue using the transducer. After that, a second set of RF waves after compression was recorder for the same ROI. Finally, cross-correlation estimates of times shifts between these two A-lines were performed using Fast Fourier Transform (FFT) The time shift T is simply the temporal location of the maximum peak of the cross-correlation function.

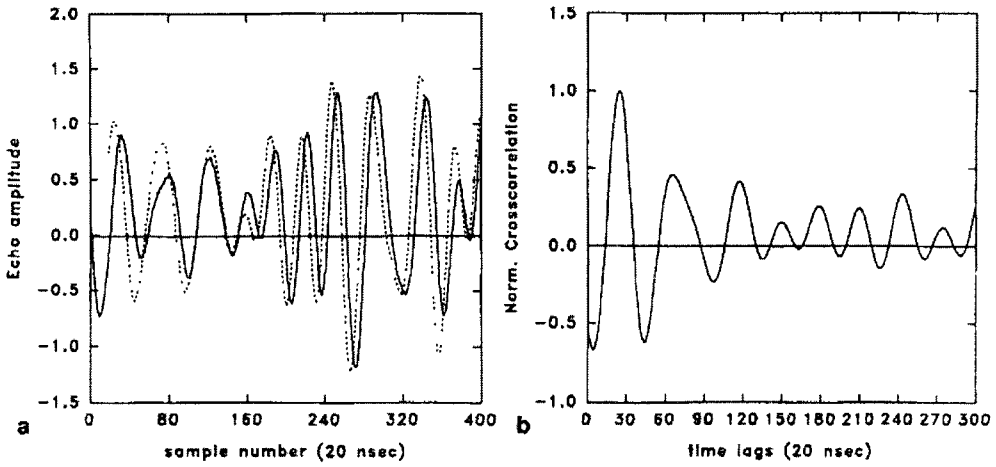

Figure 2-5 (a) RF echoes before and after compression; (b) cross-correlation function between the two RF waves (11).

The way the strain is calculated is by the following; if the compression rate applied to the ROI is constant and equal to a distance d, then the shift between the compressed and original waves is equal to $T = 2d/c$, where c is the sound speed in the tissue. Thus the strain is calculated using the following formula; $s_i = (t_{i+1} - t_i)/T$ (11). The t_i's are the time shifts between successive compressions applied to the ROI. Once the strain is calculated a color-coded map is given to the whole arterial cross-section known as elastograms.

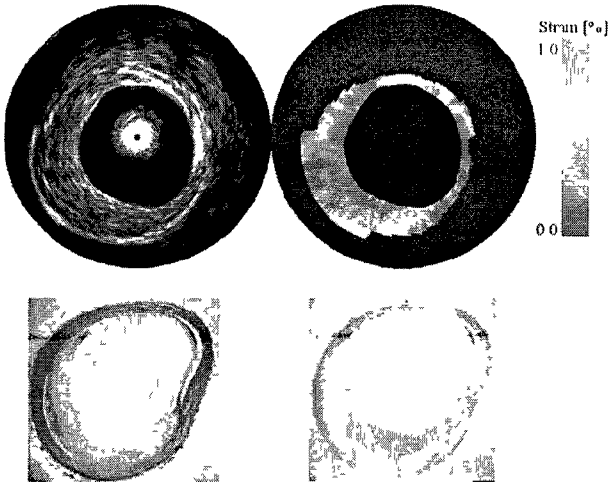

Figure 2-6 Conventional IVUS image vs. constructed elastogram (upper images) and histological sections (lower images) (12).

Shown in Figure 2-6 is elastogram of femoral artery that captured an eccentric fibrous plaque which was confirmed by histology (12). Other numerous studies have shown the ability of elastography in identifying soft and hard plaques independently of echogenicity contrast (28-32). More specifically IVUS elastography improved the discrimination between lipid rich and fibrous plaques.

	All Data (n)	Femoral (n)	Coronary (n)
Fibrous tissue	0.27 (62)	0.27 (48)	0.30 (14)
Fibro-fatty tissue	0.45 (34)	0.41 (25)	0.50 (9)
Fatty tissue	0.60 (13)	0.66 (7)	0.57 (6)
Normal vessel wall	0.44 (16)	0.44 (16)	– (–)
Total regions, n	125	96	29

Figure 2-7 Strain values of different plaques in femoral and coronary artery (13)

Despite the striking difference of the strain values for various plaques, as shown in Figure 2-7, most of the studies were performed in vitro where the temperature is different from in vivo case. Additionally excised arteries were used after freezing and thawing which influences the values of elastic modulus. Elastography has also been criticized for its inability of discriminating between normal artery and Fibrous caps which is illustrated in Figure 2-7 (13).

The use of the RF echoes content has also been used further. A method called **virtual histology** (also called **VH IVUS**) based on these IVUS-RF-ultrasonic waves has been developed (14). This tissue characterization technique is based on the calculation of the frequency spectrum analysis. In fact these frequency spectra were generated using auto-regressive models. From these spectra some parameters were obtained (15). Illustrated in Figure 2-8 is how these parameters are generated from a given frequency domain plot. Based on the values of these parameters tissue and plaque classification has been made. Based on this numerical classification, these ROI's were compared to histological findings, linked to plaque types and given color-coded maps.

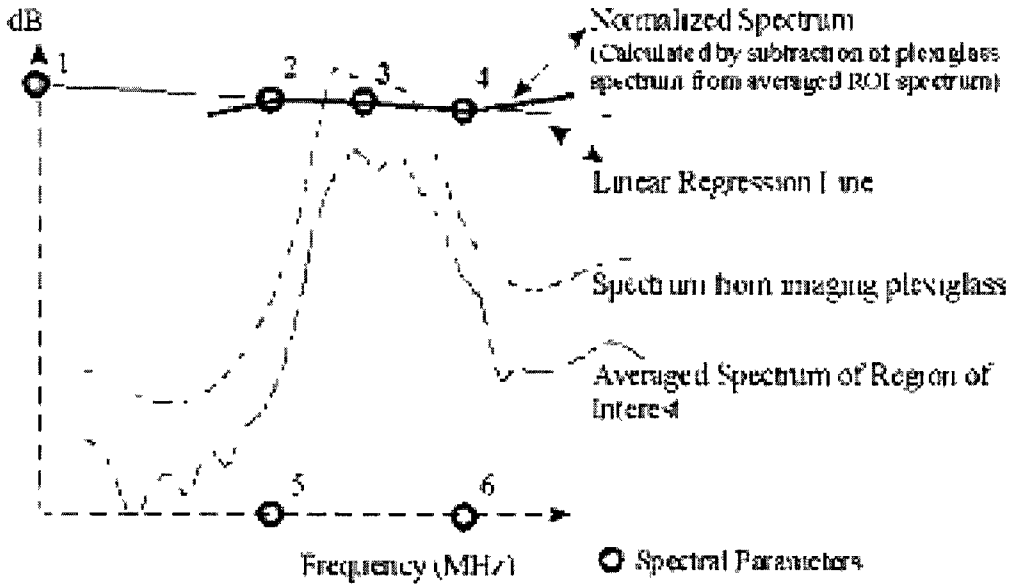

Figure 2-8 Spectral parameters computation from the RF echo frequency content (15)

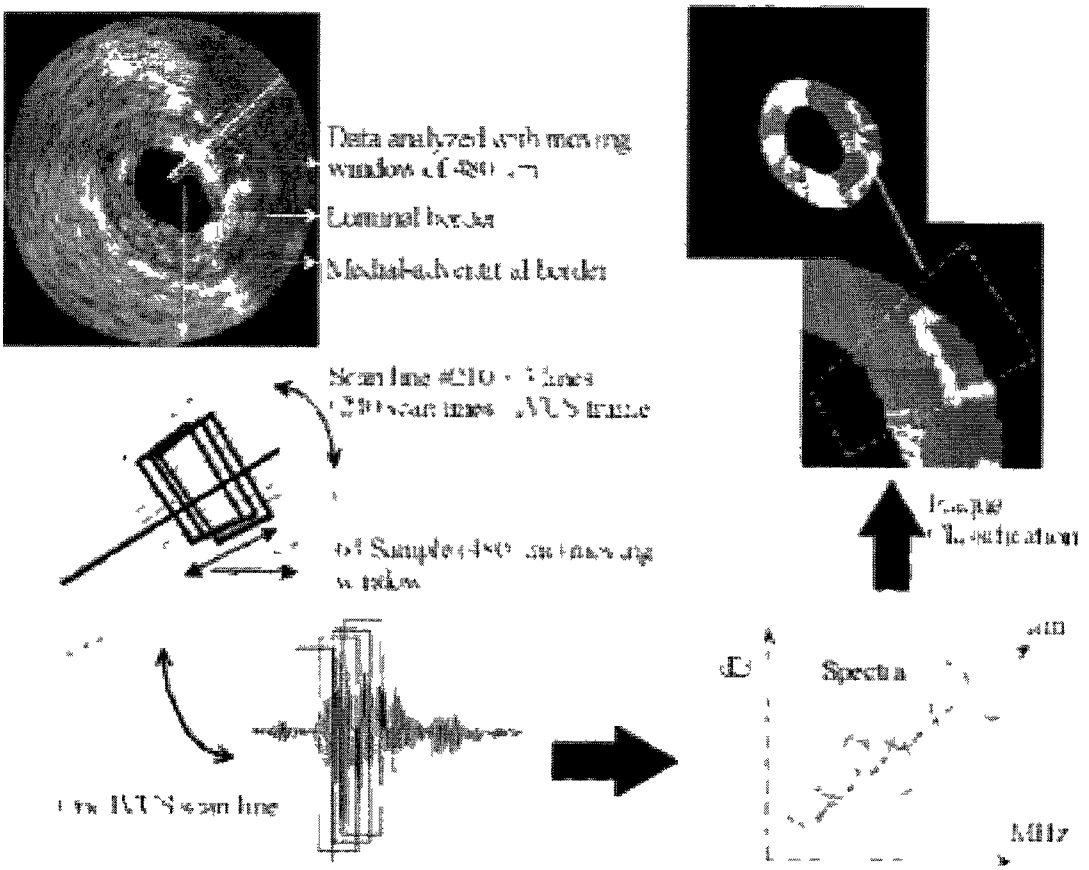

Figure 2-9 Automated steps for tissue color-coded maps construction (15)

Shown in Figure 2-9 are the different steps from acquiring the original RF echoes to the construction of color-coded maps for ROI's. VH IVUS through the images illustrated in Figure 2-10 has shown its full potential to distinguish accurately between different plaques. Several limitations accompanied the development of VH IVUS. In fact, virtual histology gives an axial resolution which is too low to detect fibrous cap thickness. In addition the detection between soft plaque material and thrombus is not possible. To circumvent the problem of small-sized areas detection, efforts has to be put on augmenting the resolution of the IVUS equipments.

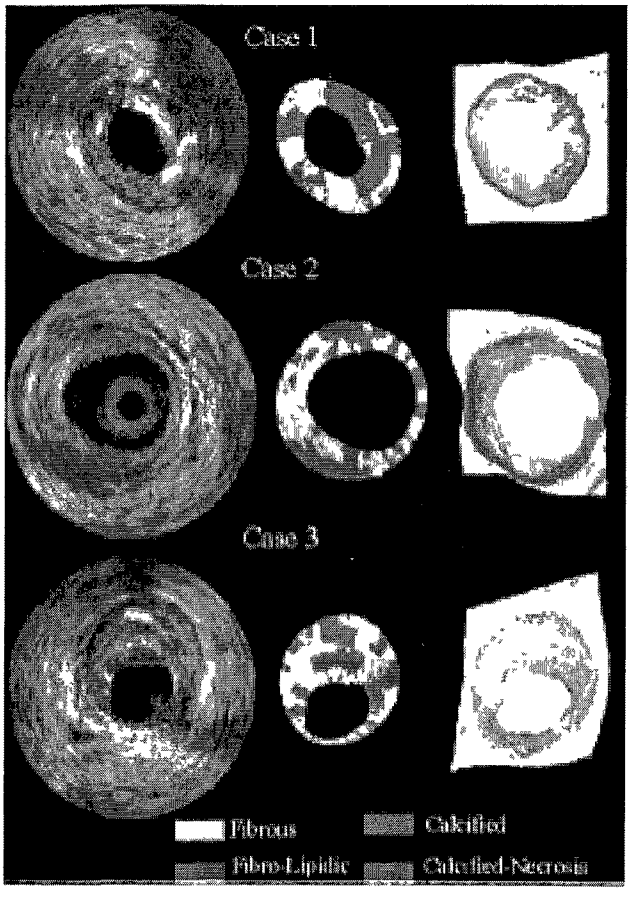

Figure 2-10 Comparison of IVUS images (left) vs. VH IVUS images (middle) and histology sections (right) (15).

Many other IVUS developments involving therapeutic and interventional functions have been introduced in the clinical world (16). Most of these applications were mentioned in the introductory chapter. Since the object of this work in primary and

ultimately tissue characterization, these interventional aspects will not be addressed in this review chapter.

Despite this simplicity of image construction from IVUS and the development of some signal processing procedures to overcome the lack of plaque characterization, there are significant challenges which limited the accuracy and clarity of the images produced via IVUS. These challenges are always present in the imaging process. For example, the omnipresence of noise related to the acquisition of the ultrasound waves (due to electronic devices) plays an important role on hiding useful information during the detection process. Moreover uncertainties due to sound speed variation, eccentricity of the transducer as well as scattering (related to small particles such as cells, and irregular surfaces) are important factors which contribute to the limitations of the developed IVUS techniques for the identification of vulnerable plaques. This certainly influences the issues of resolution and inability to adequately discriminate between fibrous and lipid-rich plaques.

The nature of this imaging modality (irregularities in the geometry of the tissues and movement of the catheter tips) and the sensitivity of the recorded RF echoes has encouraged and motivated other research groups to work on modeling the ultrasound wave propagation in biological tissues and specifically IVUS.

2.2. Ultrasound wave propagation in biological tissue models

Since the IVUS imaging method is based on ultrasound wave propagation, the only way to sketch a model for this propagation will be dictated from the constitutive laws that govern these waves. To know the complete behavior of the waves towards each tissue component, a solution should be found in time and space for these signals.

The most widely used model for modeling finite amplitude sound beam propagation is the so-called Khokhlov, Zabolotskaya and Kuznetsov (KZK) equation (17)

$$\frac{\partial^2 P}{\partial z \partial t'} = \frac{c_0}{2}\nabla_\perp^2 P + \frac{\delta}{2c_0^3}\frac{\partial^3 P}{\partial t'^3} + \frac{\beta}{2\rho_0 c_0^3}\frac{\partial^2 P^2}{\partial t'^2}. \tag{2-1}$$

P is the sound pressure, z is the coordinate along the beam axis, $\nabla_{\perp}^{2}$ is the Laplacian operator, $t' = t - \frac{z}{c_0}$ is the retarded time, c_0 is the sound speed, δ is the diffusivity of sound for thermo-viscous fluid, β is the coefficient of nonlinearity and ρ_0 is the ambient fluid density.

In (18) Yan-Sub Lee et al took the cylindrical case of the KZK and performed a numerical solution of this model, i.e., $\nabla_{\perp}^{2} P = \frac{\partial^2 P}{\partial r^2} + \frac{1}{r}\frac{\partial P}{\partial r}$. r is the radial transverse coordinate.

Intermediate transformations, involving the introduction of three new variables, were carried out in order to solve the KZK model

$$p = (1+\sigma)\frac{P}{P_0}$$

$$\rho = \frac{\frac{r}{a}}{1+\sigma} \tag{2-2}$$

$$\tau = \omega_0 t' - \frac{\left(\frac{r}{a}\right)^2}{1+\sigma},$$

where $\sigma = \frac{z}{z_0}$, $z_0 = \frac{\omega_0 a^2}{2c_0}$, P_0 is the characteristic source pressure, a is the radius of the source and ω_0 is the source angular frequency.

Substituting these new variables and integrating with respect to time has given

$$\frac{\partial p}{\partial \sigma} = \frac{1}{4(1+\sigma)^2}\int_{-\infty}^{\tau}\left(\frac{\partial^2 p}{\partial \rho^2} + \frac{1}{\rho}\frac{\partial p}{\partial \rho}\right)d\tau' + A\frac{\partial^2 p}{\partial \tau^2} + \frac{Np}{1+\sigma}\frac{\partial p}{\partial \tau}, \tag{2-3}$$

where $A = \alpha_0 z_0$ and $N = \frac{z_0}{\tilde{z}}$, such that $\alpha_0 = \frac{\delta\omega_0^2}{2c_0^3}$ and $\tilde{z} = \frac{\rho_0 c_0^3}{\beta\omega_0 P_0}$.

This modified version of the KZK equation is solved numerically by discretizing the new variable $p(\rho,\sigma,\tau)$ in space and time.

Discretization, by a sufficiently small increment $\Delta\sigma$, makes the decoupling of the three terms in the right hand side of the modified KZK equation permissible. The solution of this equation is achieved by simply solving these three terms in three different equations referring respectively to diffraction, absorption and nonlinear effects (18)

$$\begin{cases} \dfrac{\partial p}{\partial \sigma} = \dfrac{1}{4(1+\sigma)^2} \displaystyle\int_{-\infty}^{\tau} \left(\dfrac{\partial^2 p}{\partial \rho^2} + \dfrac{1}{\rho}\dfrac{\partial p}{\partial \rho} \right) d\tau' \\ \dfrac{\partial p}{\partial \sigma} = A \dfrac{\partial^2 p}{\partial \tau^2} \\ \dfrac{\partial p}{\partial \sigma} = \dfrac{Np}{1+\sigma}\dfrac{\partial p}{\partial \tau} \end{cases} \tag{2-4}$$

The two first equations has been solved numerically using implicit backward difference method in the near field and crank-Nicolson method (based on central difference approximation) in far field of the transducer. Applying these finite difference schemes has yielded to a system of linear equations which are solved easily. For the first equation the trapezoidal rule was used to evaluate the time integration. The third equation has been solved numerically based on the analytical solution $p(\sigma,\tau) = F[\tau + Np\ln(1+\sigma)]$ where $F(\tau) = p(0,\tau)$ is the source waveform.

The KZK equation has been solved by implementing independently the three numerical schemes of the three equations. The final solution was obtained using the following methodology; the solution of the diffraction equation at step $k+1$ is used to initiate the absorption at the previous step k. After that the same approach is adopted to initiate the nonlinear numerical algorithm at step k from what was found for the diffraction solution at step $k+1$. Finally what was recovered from the nonlinearity effect algorithm is including all the three effects in the propagating pressure solution.

Although the KZK model contains all the effects (diffraction, nonlinearity and absorption phenomena) that occur during the sound propagation in biological tissue, this

model is restricted to thermo-viscous fluids. The viscous absorption term of the model dictates that the attenuation coefficient is proportional to the square of the frequency which is not the case for the soft tissues where this relation is linear.

In (19) another time domain model for the sound wave propagation in tissues is developed based on a second order operator splitting. In fact based on general wave theory, differential equations of the evolution type were adopted to model ultrasound propagation

$$\frac{\partial v(\tau, z)}{\partial z} \equiv \hat{L}.v, \tag{2-5}$$

where v is the particle velocity, z is the coordinate in the direction of wave propagation, $\tau = t - \frac{z}{c_0}$ is the retarded time, c_0 is the wave speed and $\hat{L}$ is the operator that accounts for the effects influencing the wave form.

For example the absorption effect is characterized by

$$\hat{L}_A.v \equiv \int_{-\infty}^{\tau} K(z, \tau - \tau').v(z, \tau')d\tau', \tag{2-6}$$

where K is found based on the dependence of the attenuation.

Nonlinearity was also characterized by

$$L_N.v \equiv \frac{\beta}{c_0^2} v \frac{\partial v}{\partial \tau}, \tag{2-7}$$

where β is the coefficient of medium nonlinearity.

Diffraction effect was as well characterized by the following operator

$$\hat{L}_D.v \equiv \nabla_{\perp}^2 \int_{-\infty}^{\tau} v d\tau', \tag{2-8}$$

where $\nabla_{\perp}^{2}$ is the 2D transverse Laplacian and v is the axial component of the particle velocity.

In this model each operator effect was studied independently. Thus each evolution differential equation was solved separately. First the solution to the absorption equation was found using a digital filter model. This filter was characterized by a transfer function $G(e^{j\Omega})$, $\Omega = \omega T$ where T is the time sampling period. The waveform was calculated using the discrete convolution

$$v_n(z+\Delta z) = \sum_{k=-\infty}^{+\infty} v_k(z).g_{n-k}(\Delta z), \tag{2-9}$$

where $g_n(\Delta z) = \frac{1}{2\pi}\int_{-\pi}^{\pi} G(e^{i\Omega})e^{i\Omega n}d\Omega$.

The nonlinearity equation has an analytical solution as has been shown in the KZK model. This function is discretized to get a solution in the same space and temporal points of interest of the absorption equation. Finally the diffraction was solved using the Rayleigh integral. In (19), during the propagation process, all these effects contribute to the form of the ultrasonic wave. Hence an operator splitting algorithm is employed to apply these effects sequentially. In fact this algorithm is composed of three main steps. The Rayleigh integral is used first to solve for the pressure and particle velocity. Then the absorption effect is applied to the same variables. Finally the nonlinearity effect is introduced to get the final values of the pressure and particle velocity. After that the step counter is incremented and the same three-step procedure is iterated.

One of the difficulties for these numerical models was the computational aspect. Huge memory and supercomputing machines have to be allocated for the implementation of such nonlinear models. Even using advanced equipments in terms of performance, the computation process of these models can take several hours and even days. This is far from simulating a real time propagation of the ultrasonic waves.

Given the complexity in solving these nonlinear models, other groups of researchers have resorted to the adoption of simple linear wave equation models. In fact

ultrasound that is propagating in biological tissues generates small fluctuations. The propagation of these fluctuations is governed by what is called the wave equation. The solution of this equation is a time-dependent pressure field $p(t,x)$, $t \geq 0$ and $x \in \Omega$ where Ω is the set of points inside the medium to be simulated.

The wave equation is a second order linear partial differential equation

$$p_{tt} = c^2 \Delta p + f \,, \tag{2-10}$$

where $p_{tt} = \dfrac{\partial^2 p}{\partial t^2}$, $\Delta = \nabla.\nabla = \dfrac{\partial^2}{\partial x^2} + \dfrac{\partial^2}{\partial y^2} + \dfrac{\partial^2}{\partial z^2}$, c is the speed of sound which is function of the density and compressibility of the medium, p is the pressure field and $f(t,x)$ is the source of disturbances in pressure.

The closed form solution of the wave equation here above is unavailable. Thus two main numerical methods were proposed; which are the finite differences and the finite element methods.

In the finite differences case, discretization of time and space should be done. First derivatives were approximated by backward, forward or central differences (20). After that second derivatives were obtained from Taylor series expansion. The continuous variable p was converted to p_h as a vector of the same value of p but just evaluated in points of the medium that are equally spaced. Then the discrete first and second order derivatives were constructed as defined earlier. These discrete operators are denoted respectively by $D_h p_h$ and $\Delta_h p_h$. The initial wave equation is reduced to a system of ordinary equations of unknowns $p_h : p_h'' = c^2 \Delta_h p_h + f_h$, f_h are the values of f at the different nodes that are equally spaced and p_h'' are the time second derivatives.

This semi-discrete equation has been solved by integration methods with respect to time. Explicit methods like Euler method and more generally Runge-Kutta methods were used for integration purposes. But these methods were criticized for the stability issues. Therefore implicit methods were used to help overcome this instability. Implicit

Euler method and especially Crank-Nicolson method, which has been proven to be one of the most accurate schemes, were adopted (20).

Finite element method has also been used to solve for the linear wave equation. The idea is to construct the solution as a finite linear combination of basis functions. These basis functions, generally denoted by $\phi_i(x)$, correspond to each space node x_i and are characterized by a value equal to one at that node and a ramp decreasing linearly to zero in the adjacent nodes. The discretized solution has thus the following form $p_h = \sum_{i=1}^{N} \zeta_i(t)\phi_i(x) \cong p$. In a second phase, the variational formulation of the wave equation was performed in (21). By substituting the approximation made for the discretized solution in the variational formulation, a linear system of ordinary differential equations was produced. This system was solved by time integration schemes mentioned in the finite difference approach.

Jorgen Arendt Jensen has proposed a direct solution using Green's function (22). In fact for a given transducer surface the solution of the wave is given by

$$\psi(\vec{r}_1 + \vec{r}_2, t) = \int_S \int_T v(\vec{r}_2 + \vec{r}_3, t_2) g(\vec{r}_1, t \mid \vec{r}_2 + \vec{r}_3, t_2) dt_2 d^2\vec{r}_3, \tag{2-11}$$

where ψ is the potential velocity which related to the pressure field by $p(\vec{r}, t) = \rho_0 \frac{\partial \psi(\vec{r}, t)}{\partial t}$ where ρ_0 is the density of the medium.

The Green's function is $g(\vec{r}_1, t \mid \vec{r}_2 + \vec{r}_3, t_2) = \dfrac{\delta\left(t - t_2 - \dfrac{|\vec{r}_1 - \vec{r}_2 - \vec{r}_3|}{c_0}\right)}{2\pi|\vec{r}_1 - \vec{r}_2 - \vec{r}_3|}$.

$|\vec{r}_1 - \vec{r}_2 - \vec{r}_3|$ is the distance from the transducer surface to the point where the field is calculated, T is the integration over time, δ is the Dirac delta function and $v(\vec{r}_2 + \vec{r}_3, t_3)$ is the particle velocity normal to the transducer. Shown in Figure 2-11, is the coordinate system for performing the incident field calculation.

With the assumption that v is uniform separation of temporal and spatial integrals was made; $\psi(\vec{r}_1+\vec{r}_2,t)=\int_T v(t_2)\int_S g(\vec{r}_1,t\mid\vec{r}_2+\vec{r}_3,t_2)d^2\vec{r}_3dt_2$.

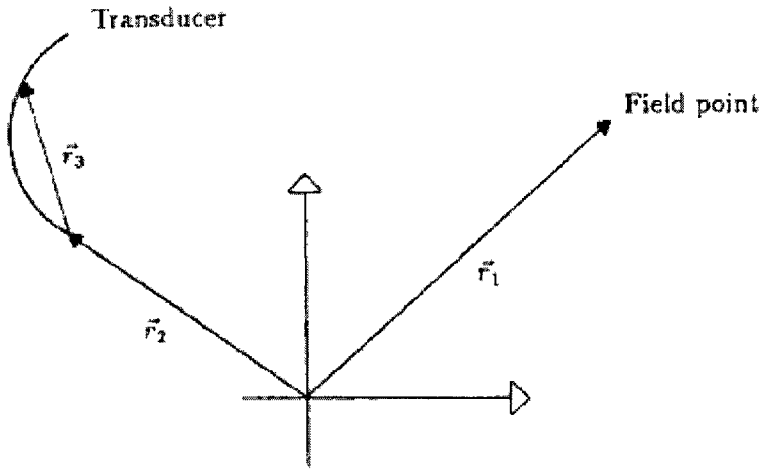

Figure 2-11 Coordinate system for calculating the incident field (22).

A spatial impulse response was defined to be

$$h(\vec{r}_1,\vec{r}_2,t-t_2)=\int_S g(\vec{r}_1,t\mid\vec{r}_2+\vec{r}_3,t_2)d^2\vec{r}_3\,. \tag{2-12}$$

Thus the solution ψ was found by the time convolution $\psi(\vec{r}_1+\vec{r}_2,t)=v(t)\underset{t}{*}h(\vec{r}_1,\vec{r}_2,t)$.

Jensen et al. approximated the impulse response numerically (23). Since it is integration over surface, this integral was approximated by a summation over small rectangles or squares that are forming the whole transducer surface:

$$h(\vec{r}_1,\vec{r}_2,t)\approx\sum_S\frac{\delta\left(t-\frac{|\vec{r}_1-\vec{r}_2-\vec{r}_3|}{c_0}\right)}{2\pi|\vec{r}_1-\vec{r}_2-\vec{r}_3|}\,.$$

These models were under the assumption of homogeneous areas which is a significant limitation since tissues boundaries are inhomogeneous. In addition to that simulation speed was much higher than real-time scale.

Rosales et al. have used Rayleigh scattering formula to simulate real IVUS images (24). In this approach it has been assumed that the reflected signal from a finite number N of scatterers at a given position $[R,\theta,Z]$ is

$$S(R,\theta,Z,T,\tau) \cong \sum_{i=1}^{N} \sigma_i(R,\theta,Z)\xi_i(t,\tau), \tag{2-13}$$

where $\sigma_i(R,\theta,Z)$ is the spatial distribution of the differential backscattering located at the ith scatterer (25). $\xi_i(t,\tau)$ is the transducer impulse function and τ is the delay time. In this study absorption effect by scatterers was neglected. These acoustical shadows could not be simulated.

Substantial effort has been made to design and establish numerical models that simulate the propagation of ultrasound waves in biological tissues. Most of these models were summarized in this review. The complexity of some of the models presented problems in terms of real time simulation and computational burden. A simpler model called Transmission Line matrix method will adopted in this work to simulate the ultrasound wave propagation. The foundation of this model will be detailed in chapter 3 and chapter 4.

Chapter 3 Regular transmission line matrix (TLM) method and ultrasound propagation

Development of physics and analytical laws (governing equations) has led to a significant understanding and explanation of many natural phenomena. Amongst these, a noteworthy effort was spent for understanding the behavior and propagation laws of Electro-Magnetic Fields (EMF) and Sound Waves. As a result, governing equations have been established for such waves. Since propagation could occur in a wide variety of media (different geometries, different properties), complex cases (that involves especially irregular geometries) are still challenging the engineering sciences for analytical solutions to these equations. In this study, interest is given to ultrasound waves propagation through human tissue, more specifically arteries. In general, this media has irregular geometry where the wave equation is impossible to solve analytically. To circumvent the inability of finding closed form solutions, numerical methods are used to estimate the unknown solutions based on a discrete representation of the continuous media. One of these numerical techniques applied to EMF and sound waves problems is the physics-based method called Transmission Line Matrix (TLM) method. TLM was first applied to the EMF problems and several published studies demonstrated the accuracy of TLM solutions (3,46). Since the sound wave propagation equations and the EMF governing equations have similarities, this method has been extended to numerous sound propagation problems and showed very good agreement with previously work appearing in the literature (3,46). In this chapter, a tutorial on the regular TLM method and its foundation will be detailed. An analogy between the EMF and Ultrasound waves will then be derived. To conclude this introduction, a regular TLM model will be developed for the simulation of the ultrasound propagation in a rectangular medium mimicking the ultrasound propagation in a portion of an artery cross-section.

3.1. Regular TLM Method

Presented are the basic definitions related to the TLM method. First a one dimensional TLM will be developed followed by a two dimensional TLM. The utility of

this approach will be demonstrated on a numerical model of ultrasound propagation later on since the propagation occurs in a 2-D medium. (1)

3.1.1. Introduction to TLM

Lumped parameter, electrical elements are used to realize the basic TLM model. These definitions along with the associated constitutive relationships will be provided.

3.1.1.1. Transmission Line Definition

Transmission Lines (TL) are defined to be coaxial cables, waveguides, or other systems of conductors that transfer electrical signals from one location to another. The most common TL is the RLC circuit (Figure 3-1).

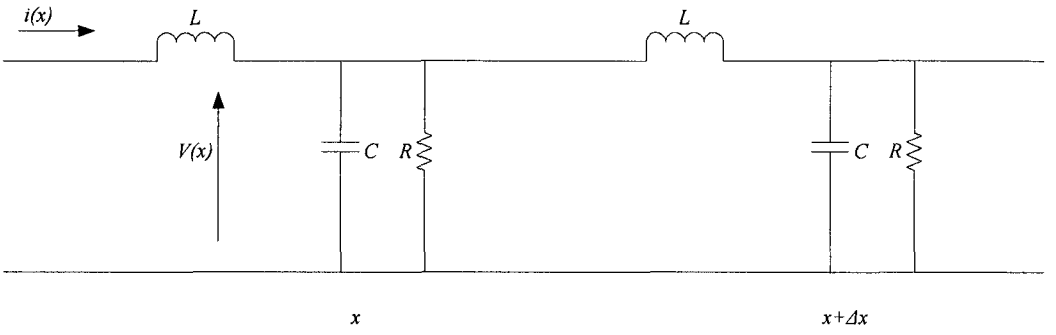

Figure 3-1 A simple transmission line circuit between points x and x+Δx

3.1.1.2. TLM Definition

Transmission Line Matrix concept was based on transmission lines. The idea of using electrical circuits for TLM came from the analogy that was established between the current or voltage propagating in this line from one point to another and the EMF governing equations. Besides this analogy, TLM was based on the Huygens principle where each point of a wave front is regarded as a secondary wave source point and the surface tangent to the secondary wave fronts is used to determine the future position of wave front (Figure 3-2). TLM models this physics by discretizing the medium into a mesh grid and replacing the wave amplitudes by voltages and currents traveling from one node to another (Figure 3-3).

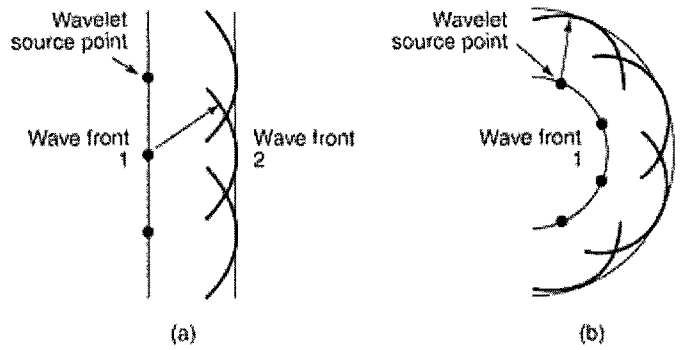

Figure 3-2 Schematics of the Huygens principle for wave propagation (www.cliffsnotes.com)

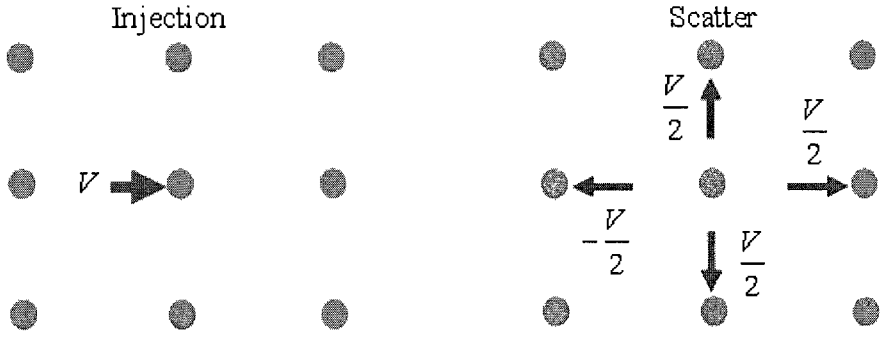

Figure 3-3 Propagation in TLM model

3.1.1.3. Analogy between TLM and EMF

Kirchhoff's voltage law applied to the circuit ABCD in Figure 3-4 gives

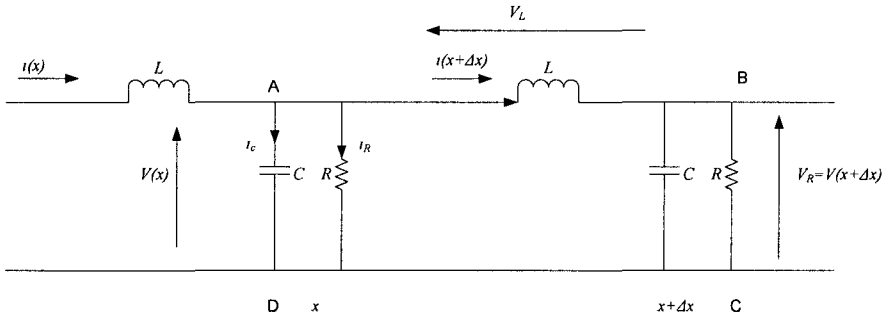

Figure 3-4 TLM circuit between two nodes

$$V(x) - V_L - V_R = 0$$

$$\Leftrightarrow V(x) - L\frac{\partial i(x+\Delta x)}{\partial t} - V(x+\Delta x) = 0$$

$$\Leftrightarrow -[V(x+\Delta x) - V(x)] = L\frac{\partial i(x+\Delta x)}{\partial t}$$

$$\Leftrightarrow -\frac{[V(x+\Delta x) - V(x)]}{\Delta x}\Delta x = L\frac{\partial i(x+\Delta x)}{\partial t} \tag{3-1}$$

$$\Leftrightarrow -\frac{\partial V(x)}{\partial x}\Delta x = L\frac{\partial i(x)}{\partial t}, \Delta x \to 0.$$

Kirchhoff's current law applied to the same circuit in Figure 3-4 gives

$$i(x) = i_c + i_R + i(x+\Delta x)$$

$$\Leftrightarrow i(x) - i(x+\Delta x) = C\frac{\partial V(x)}{\partial t} + \frac{V(x)}{R}$$

$$\Leftrightarrow \frac{i(x) - i(x+\Delta x)}{\Delta x}\Delta x = C\frac{\partial V(x)}{\partial t} + \frac{V(x)}{R} \tag{3-2}$$

$$\Leftrightarrow \frac{\partial i(x)}{\partial x}\Delta x = C\frac{\partial V(x)}{\partial t} + \frac{V(x)}{R}, \Delta x \to 0.$$

To recapitulate, Kirchhoff's laws are given by the following equations

$$-\frac{\partial V(x)}{\partial x}\Delta x = L\frac{\partial i(x)}{\partial t}, \tag{3-3}$$

$$-\frac{\partial i(x)}{\partial x}\Delta x = C\frac{\partial V(x)}{\partial t} + \frac{V}{R}. \tag{3-4}$$

Combining Equations (3-3) and (3-4) the following expression is obtained as a function of current only

$$\frac{\partial^2 i}{\partial x^2} = \frac{LC}{(\Delta x)^2}\frac{\partial^2 i}{\partial t^2} + \frac{L}{(\Delta x)^2 R}\frac{\partial i}{\partial t}. \tag{3-5}$$

It can be shown that the one-dimensional EM field problem in terms of the current density j [Amperes per square meters, Am^{-2}] is

$$\frac{\partial^2 j}{\partial x^2} = \mu\varepsilon\frac{\partial^2 j}{\partial t^2} + \mu\sigma\frac{\partial j}{\partial t}, \tag{3-6}$$

where μ [Henry per meter, Hm^{-1}], ε [Farads per meter, Fm^{-1}] and σ[Siemens per meter, Sm^{-1}] are the magnetic permeability, electric permittivity and electrical conductivity of the medium.

Equations (3-5) and 3-6) are similar thus there is analogy between the circuit and EMF problems.

3.1.2. One Dimensional Regular TLM

This section will be divided into three main parts. First Thevenin theorem will be introduced. Then 1-D TLM line will be developed for a lossless line (no resistance) as well as lossy line (presence of the resistance term). Finally a 1-D regular TLM model will be established for unidirectional wave propagation.

3.1.2.1. Thevenin Theorem

Since the Thevenin theorem is essential in TLM formulation, this section will be employed to explain this theorem. The Thevenin Theorem states that any combination of linear circuit elements and active sources connected to a given load R_L may be replaced by a simple two terminal network consisting of a single voltage source of V_{TH} and a single resistance R_{eq} in series with the voltage source, across the two terminals of the load R_L (Figure 3-5) (26).

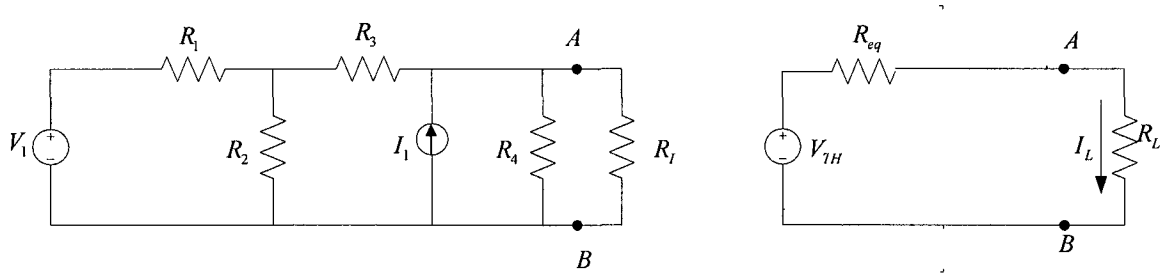

Figure 3-5 Thevenin equivalent circuit

The voltage V_{TH} is the open circuit voltage measured at the two terminals of interest with load resistance R_L removed. This voltage is called Thevenin's equivalent voltage. The equivalent resistance R_{eq} is the resistance of the given network as viewed through the terminals where R_L is connected, but with R_L removed and all active sources are replaced by their internal resistances (Figure 3-6).

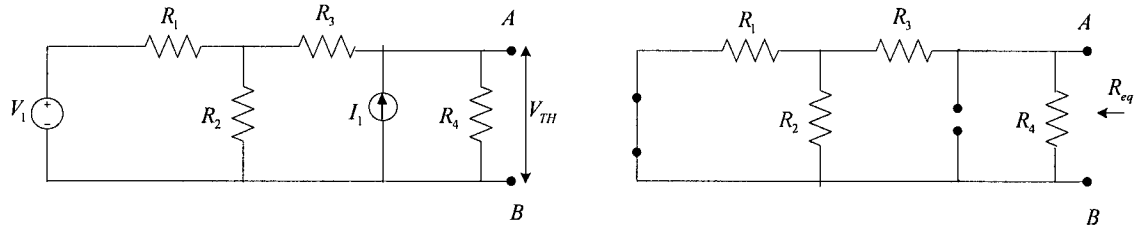

Figure 3-6 V_{TH} and R_{eq} calculation

The Thevenin voltage is obtained across the terminals A-B after removing the resistance R_L as shown in Figure 3-6. The resistence R_{eq} is the equivalent resistance as viewed through the terminals A-B after removing R_L and replacing voltage sources by short circuits and current sources by open circuits.

In the next two sections Thevenin equivalent circuits will be derived for different types of lines.

3.1.2.2. Lossless Line

A lossless line is characterized by an LC circuit between two nodes without the presence of any resistance term (Figure 3-7). In this section a detailed formulation of the

TLM on a simple line relating two consecutive nodes will be studied. Hence several key parameters of these lines will be defined. For instance, the line characteristic impedance will be derived. Moreover the incident and reflected voltages that propagate through this line will be calculated. The speed of propagation will be also determined. These parameters are functions of the inductance, capacitance and voltage source terms of this line. These incident and reflected voltages as well as the characteristic impedance and transmission speed are primordial in defining the transmission that occurs in this line between the two nodes.

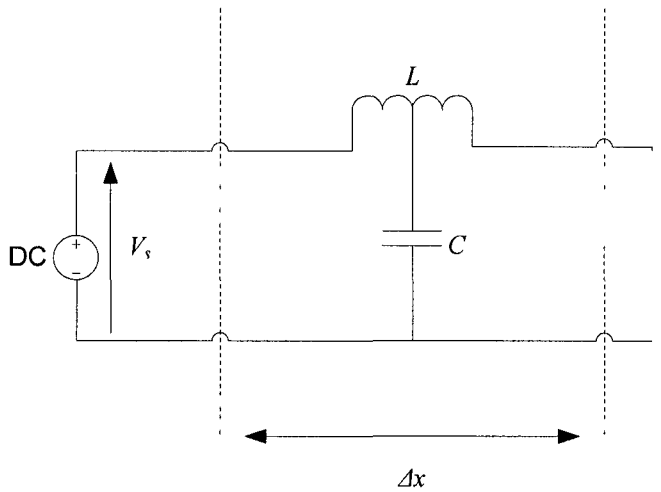

Figure 3-7 Lossless transmission line

Given the DC source of voltage V_s which penetrated the distance Δx into the line, the capacitance segment $C\Delta x$ [Farads, F] is charged. This charge is $\Delta Q = C\Delta x V_s$.

Hence the current is

$$i = \frac{\Delta Q}{\Delta t} = CV_s \frac{\Delta x}{\Delta t} = CV_s u\,, \tag{3-7}$$

where u is the velocity of propagation along the line of the disturbance caused by the introduction of the source. Due to the existence of both current and velocity a flow of current is created. The flow of this current will induce a magnetic flux Φ coming from the inductance $L\Delta x$ [Henry H]

$$\Phi = L\Delta x i = L\Delta x C V_s u \,. \tag{3-8}$$

On the other hand, the Faraday's law stating that **"the flux rate change must equal the line voltage"** will give

$$V_s = \frac{\Delta\Phi}{\Delta t} = LCV_s u^2$$

$$\Leftrightarrow 1 = LCu^2$$

$$\Leftrightarrow u = \frac{1}{\sqrt{LC}}[m/\sec]. \tag{3-9}$$

Replacing the velocity by its expression in equation (3-7) $i = \frac{V_s}{\sqrt{L/C}} = \frac{V_s}{Z}$, Z is the characteristic impedance of the line,

$$Z = \sqrt{\frac{L}{C}}\Omega \,. \tag{3-10}$$

Now if a transmission line of length l is considered to have an open-circuit termination, then the current at the open-circuit must be zero. So there must be a current, $-\frac{V_s}{Z}$ starting from the termination of the circuit and traveling toward the source so that the current goes to zero as it approaches the termination position. A voltage V' is associated with the current $-\frac{V_s}{Z}$. The overall voltage at the source after reflection from the circuit termination along the line is then $V_s + V'$ and the current is zero these values take place at time 2τ, where $\tau = \frac{l}{u}$.

To determine the expression of V' the energy conservation principle: **"Energy Stored in the line=Energy supplied by the source"** is used.

The energy stored in the line is associated with the capacitance

$$E_c = \frac{1}{2}(Cl)(V_s + V')^2 . \tag{3-11}$$

The energy supplied by the source

$$E_s = V_s i 2\tau = \frac{2\tau V_s^2}{Z} . \tag{3-12}$$

Equating both of the energies (3-11) and (3-12) will lead to

$$\begin{aligned} &\frac{1}{2}Cl(V_s + V')^2 = V_S \frac{V_S}{Z} 2\tau \\ &\Leftrightarrow C\frac{l}{\tau}(V_s + V')^2 = 4\frac{V_s^2}{Z} \\ &\Leftrightarrow Cu(V_s + V')^2 = 4\frac{V_s^2}{Z} \end{aligned} .$$

Recall equation (3-7) $i = \frac{\Delta Q}{\Delta t} = CV_s \frac{\Delta x}{\Delta t} = CV_s u \Leftrightarrow Cu = \frac{i}{V_s} = \frac{1}{Z}$

$$\Rightarrow \frac{1}{Z}(V_s + V')^2 = \frac{(V_s + V_s)^2}{Z}$$

$$V' = V_s . \tag{3-13}$$

So an incident voltage pulse to an open circuit termination is reflected back so that the total voltage is twice the incident. By denoting I for incident pulse and R for reflected pulse we have

$$\begin{cases} V^I = V_s \\ V^R = V_s \\ i^I = \frac{V_s}{Z} \\ i^R = -\frac{V_s}{Z} \end{cases} . \tag{3-14}$$

Using Thevenin Theorem, the open circuit can be, consequently, replaced by the Thevenin equivalent circuit shown in Figure 3-8.

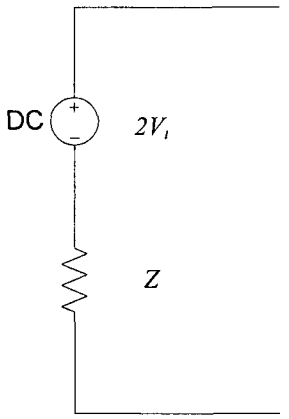

Figure 3-8 Equivalent Thevenin Circuit

The voltage source of the Thevenin circuit is equal to the open circuit voltage which is

$$2V_s = 2V_i. \tag{3-15}$$

The impedance of the Thevenin circuit is equal to the input impedance of the line which is Z.

3.1.2.3. Lossy Line

A lossy line is illustrated by the following circuit

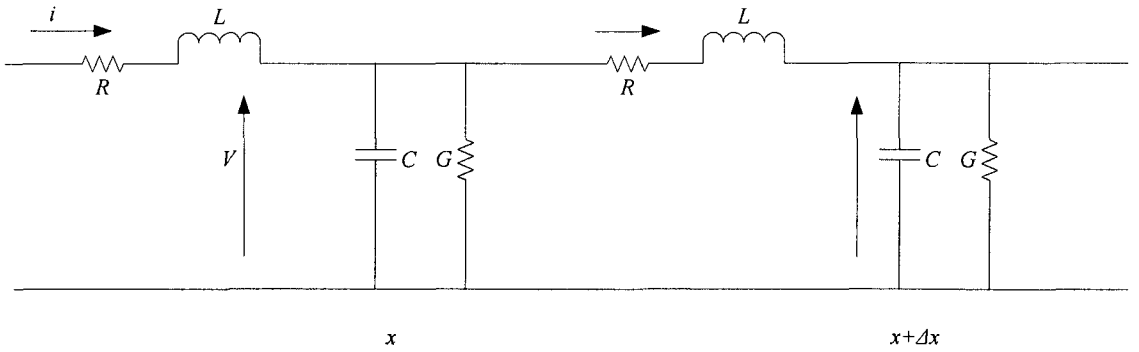

Figure 3-9 Lossy transmission line

R and G are the series resistance and shunt admittance, and L and C are the series inductance and shunt capacitance per section of length Δx.

Applying Kirchhoff's laws as seen in the previous section, these expressions are obtained

$$\Delta x \frac{\partial V(x)}{\partial x} = -L \frac{\partial i(x)}{\partial t} - iR, \tag{3-16}$$

$$\Delta x \frac{\partial i(x)}{\partial x} = -GV(x) - C \frac{\partial V(x)}{\partial t}. \tag{3-17}$$

Combining equations (3-16) and (3-17) either voltage or current can be eliminated to lead to

$$\frac{\partial^2 i(x)}{\partial x^2} = \frac{GR}{(\Delta x)^2} i(x) + \frac{1}{(\Delta x)^2}(GL + RC)\frac{\partial i(x)}{\partial t} + \frac{LC}{(\Delta x)^2}\frac{\partial^2 i(x)}{\partial t^2}, \tag{3-18}$$

$$\frac{\partial^2 V(x)}{\partial x^2} = \frac{GR}{(\Delta x)^2} V(x) + \frac{1}{(\Delta x)^2}(GL + RC)\frac{\partial V(x)}{\partial t} + \frac{LC}{(\Delta x)^2}\frac{\partial^2 V(x)}{\partial t^2}. \tag{3-19}$$

As seen previously, the inductance and capacitance can be replaced by the equivalent Thevenin circuit, consequently, the following line segment (Figure 3-10 a)) can be replaced by its Thevenin circuit (Figure 3-10 b))

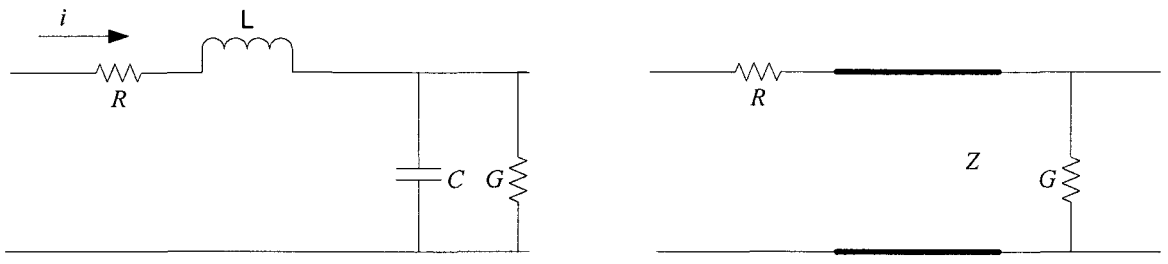

Figure 3-10 a) Line segment b) TLM model based on Thevenin Equivalent circuit

3.1.3. 1D TLM Model:

If a one dimensional line section is to be modeled by a series of basic line elements n, then a finite number of connecting nodes between these elements are exposed

to Thevenin equivalent voltages coming from both sides (right and left). A typical node will be presented by the following circuit (if resistances R and G are included)

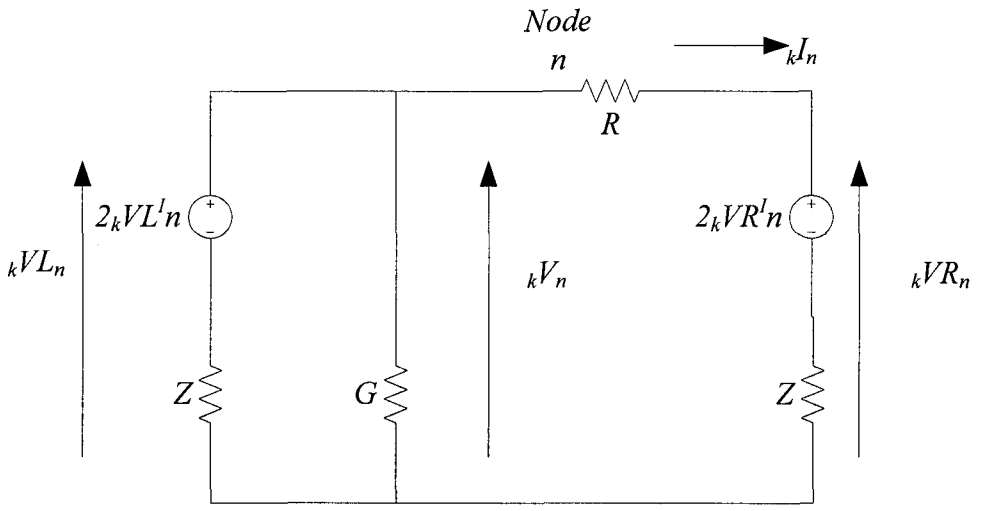

Figure 3-11 Thevenin equivalent circuit for 1-D transmission line network

From the above circuit the total voltage ${}_kV_n$ at node n at time step k is the result of the incident voltages coming from the left $\left({}_kVL_n^I\right)$ and the right $\left({}_kVR_n^I\right)$ of this node (suffix I stands for incident). Using Millman's Theorem the voltage ${}_kV_n$ is given by

$$ {}_kV_n = \frac{\dfrac{2_kVL_n^I}{Z} + \dfrac{2_kVR_n^I}{Z+R}}{\dfrac{1}{Z} + \dfrac{1}{Z+R} + G}, \tag{3-20} $$

and the current ${}_kI_n$ is given by

$$ {}_kI_n = \frac{{}_kV_n - 2_kVR_n^I}{R+Z}. \tag{3-21} $$

The total voltages of the left and right lines of the node are

$$ {}_kVL_n = {}_kV_n \tag{3-22} $$

$$ {}_kVR_n = 2\,{}_kVR_n^I + {}_kI_nZ\,. \tag{3-23} $$

The voltages reflected back to the left and right line are

$$ {}_kVL_n^R = {}_kVL_n - {}_kVL_n^I \tag{3-24} $$

$$ {}_kVR_n^R = {}_kVR_n - {}_kVR_n^I\,. \tag{3-25} $$

These relations show that all the reflected voltages can be known once the incident voltages are given. Generally the incident voltages at time $k = 0$ are equal to zero. Now to derive the values of voltages as function of time, the following is obtained

$$ {}_{k+1}VL_n^I = {}_kVR_{n-1}^R \tag{3-26} $$

$$ {}_{k+1}VR_n^I = {}_kVL_{n+1}^R\,. \tag{3-27} $$

Equations (3-24) and (3-25) show how the reflected (or scattered) voltages in both sides of a given node are calculated given the incident voltages at a certain time step. This is called the scattering process. Equations (3-26) and (3-27) determine the propagation evolution in time. In fact the reflected voltages will serve as incident voltages to the surrounding nodes from the right and left directions (Figure 3-12).

Figure 3-12 One-dimensional TLM scattering process

The blue arrow represents the initial incident voltage (or wave) to node 2 at instant t_0. At the same instant, this incident voltage is reflected in the direction of node 1 and node 3 (left and right direction to node 2). These reflected voltages are presented by the green arrows. These voltages will travel to the next nodes to serve as the incident voltages to nodes 1 and 3 (red arrows) at the next time instant t_1.

3.1.4. Two Dimensional Regular TLM

The 2-D TLM method has been widely developed and studied in the literature because of its importance in terms of treating wave propagation in the two dimensional

space. As mentioned previously the use of TLM method for wave propagation purposes was first inspired from the analogy that was found between the electric circuit variables and the EMF problem.

3.1.4.1. EMF 2-D problem

TLM method showed very interesting results for solving the EMF problem in 2-D. In this part the EMF governing equations in 2-D will be introduced and its TLM model will be derived. In the two dimensional case the Maxwell's equations can be reduced to two possible configurations, the TE mode (the H_z component is different from zero) $\frac{\partial^2 H_z}{\partial x^2} - \frac{\partial^2 H_z}{\partial y^2} = \mu\varepsilon \frac{\partial^2 H_z}{\partial t^2}$ and the TM mode (the E_z component is different from zero) $\frac{\partial^2 E_z}{\partial x^2} + \frac{\partial^2 E_z}{\partial y^2} = \mu\varepsilon \frac{\partial^2 E_z}{\partial t^2}$.

3.1.4.2. TLM circuit structure for TE mode:

The TE mode will be developed in this section. This mode is given by the following system of equations

$$\begin{aligned} \frac{\partial E_y}{\partial x} - \frac{\partial E_x}{\partial y} &= -\mu \frac{\partial H_Z}{\partial t} \\ \frac{\partial H_Z}{\partial y} &= \varepsilon \frac{\partial E_x}{\partial t} \\ \frac{\partial H_Z}{\partial x} &= \varepsilon \frac{\partial E_y}{\partial t} \end{aligned} \quad . \tag{3-28}$$

These three equations can be reduced to the following

$$\frac{\partial^2 H_z}{\partial x^2} - \frac{\partial^2 H_z}{\partial y^2} = \mu\varepsilon \frac{\partial^2 H_z}{\partial t^2}. \tag{3-29}$$

The circuit structure describing a node in the x-y plane is shown in Figure 3-13.

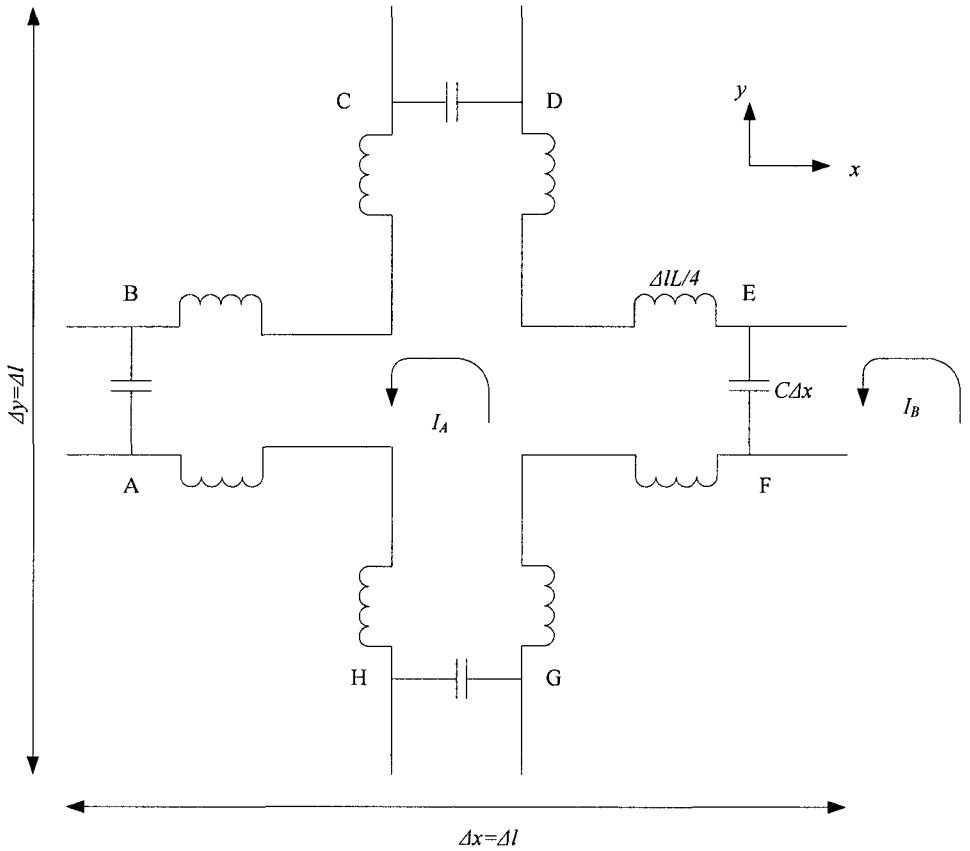

Figure 3-13 The series TLM node

These basic LC circuits are modeling the transmission of currents and voltages that occur in the four lines intersecting a node (Figure 3-14).

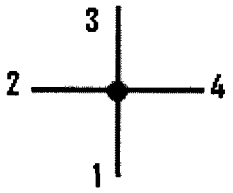

Figure 3-14 Lines intersecting a single node

The sum of the capacitances voltages is given by

$$V_{AB} + V_{CD} + V_{EF} + V_{GH} = 2L\Delta l \frac{\partial I_A}{\partial t} \tag{3-30}$$

$$-(V_{FE}-V_{AB})+(V_{CD}-V_{HG})=2L\Delta l\frac{\partial I_A}{\partial t}$$

$$\Leftrightarrow -[E_y(x+\Delta x)-E_y(x)]\Delta y+[E_x(y+\Delta y)-E_x(y)]\Delta x=2L\Delta l\frac{\partial I_A}{\partial t}.$$

$$\Leftrightarrow -\frac{E_y(x+\Delta x)-E_y(x)}{\Delta x}+\frac{E_x(y+\Delta y)-E_x(y)}{\Delta y}=2L\frac{\Delta l}{\Delta x\Delta y}\frac{\partial I_A}{\partial t}$$

Taking into account that $\Delta x = \Delta y = \Delta z = \Delta l$ and substituting $I_A = H_z\Delta z = H_z\Delta l$

$$\Rightarrow \frac{\Delta E_x}{\Delta y}-\frac{\Delta E_y}{\Delta x}=2L\frac{\partial H_z}{\partial t}. \tag{3-31}$$

Moreover the condition across the capacitor EF gives $I_A - I_B = C\Delta x\frac{\partial V_{EF}}{\partial t}$, which is equivalent to

$$\frac{[H_z(x+\Delta x)-H_z(x)]}{\Delta x}=-C\frac{\Delta x\Delta y}{\Delta x}\frac{\partial E_y}{\partial t}, \tag{3-32}$$

when $\Delta l \to 0$, $\frac{\partial H_z}{\partial x}=-C\frac{\partial E_y}{\partial t}$.

This calculation is performed for just one node in the $x-y$ plane. However to characterize the entire $\Delta x\Delta y$ domain, the whole medium is discretized into a finite number of nodes interconnected to each other (Figure 3-15). Then each node is substituted by its Thevenin equivalent circuit in order to calculate the characteristic impedance of each line.

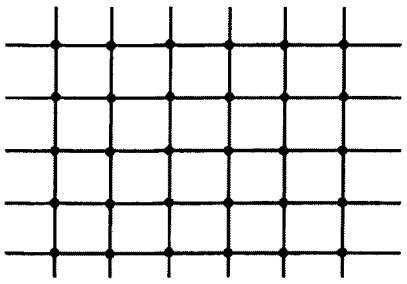

Figure 3-15 Discretization of the domain in a TLM mesh

3.1.4.3. TLM circuit structure for TM mode:

The TM mode will be developed in this section. This mode is given by the following system of equations

$$\begin{aligned} \frac{\partial H_y}{\partial x} - \frac{\partial H_x}{\partial y} &= \varepsilon \frac{\partial E_Z}{\partial t} \\ \frac{\partial E_Z}{\partial y} &= -\mu \frac{\partial H_x}{\partial t} \\ -\frac{\partial E_Z}{\partial x} &= -\mu \frac{\partial H_y}{\partial t} \end{aligned} \quad . \tag{3-33}$$

These three equations can be reduced to the following

$$\frac{\partial^2 E_z}{\partial x^2} + \frac{\partial^2 E_z}{\partial y^2} = \mu\varepsilon \frac{\partial^2 E_z}{\partial t^2} \, . \tag{3-34}$$

The circuit structure describing a node in the x-y plane is shown in Figure 3-16.

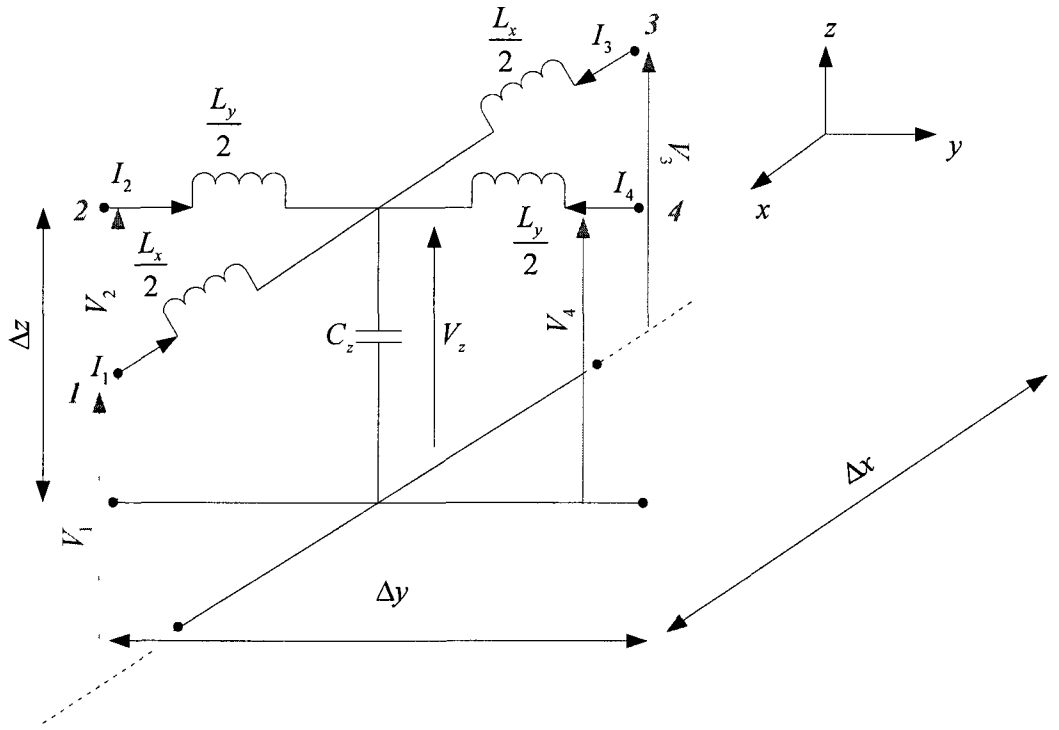

Figure 3-16 Shunt TLM node

The propagation in x and y directions will be examined. For the case where the propagation occurs in x direction, the equivalent circuit can be represented by Figure 3-17

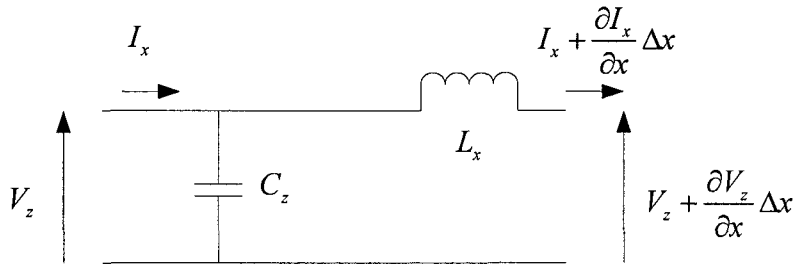

Figure 3-17 Shunt line for the propagation in the x direction

Using Kirchhoff's law and current laws, $L_x \frac{\partial I_x}{\partial t} = -\frac{\partial V_z}{\partial x}\Delta x$ and $C_x \frac{\partial V_z}{\partial t} = -\frac{\partial I_x}{\partial x}\Delta x$. Taking the partial derivative of the first equation with respect to x and the second equation with respect to t, we obtain

$$\frac{\partial^2 V_z}{\partial x^2}\frac{(\Delta x)^2}{L_x} = \frac{\partial^2 V_z}{\partial t^2}. \tag{3-35}$$

Applying the same approach for the propagation in y direction (Figure 3-18), gives

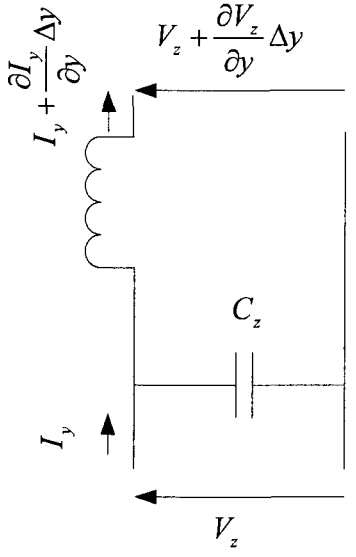

Figure 3-18 Shunt line for the propagation in the y direction

$$\frac{\partial^2 V_z}{\partial y^2}\frac{(\Delta y)^2}{L_y} = \frac{\partial^2 V_z}{\partial t^2}. \tag{3-36}$$

Combining equations (3-35) and (3-36)

$$\frac{\partial^2 V_z}{\partial x^2}\frac{(\Delta x)^2}{L_x} + \frac{\partial^2 V_z}{\partial y^2}\frac{(\Delta y)^2}{L_y} = 2C_z\frac{\partial^2 V_z}{\partial t^2}. \tag{3-37}$$

Compared to equation (3-34), the circuit parameters can be calculated the same way as for the series node case $L_x = \mu\frac{\Delta x\Delta z}{\Delta y}, L_y = \mu\frac{\Delta y\Delta z}{\Delta x}, C_z = \varepsilon\frac{\Delta x\Delta y}{\Delta z}$.

Substituting these quantities in equation (3-37),

$$\frac{\partial^2}{\partial x^2}\left(\frac{V_z}{\Delta z}\right) + \frac{\partial^2}{\partial y^2}\left(\frac{V_z}{\Delta z}\right) = (2\varepsilon)\mu\frac{\partial^2}{\partial t^2}\left(\frac{V_z}{\Delta z}\right). \tag{3-38}$$

Comparing the above equation to the EMF TM modes the following equivalences can be extracted

$$\begin{aligned} -\frac{V_z}{\Delta z} &\leftrightarrow E_z \\ +\frac{I_x}{\Delta y} &\leftrightarrow H_y \\ -\frac{I_y}{\Delta x} &\leftrightarrow H_x \end{aligned}. \tag{3-39}$$

3.1.4.4. 2-D TLM scattering in a regular mesh for TE mode:

In a regular mesh, each node is characterized by equally spaced nodes related to each other by four lines (in the x and y directions) as illustrated in Figure 3-16. This series node in a Cartesian regular mesh is presented by four transmission line segments each of characteristic impedance $Z_i, i = 1,2,3,4$. These four lines have the same length (i.e. same impedance). The scattering is calculated based on the incident $\left({}_kV_i^I\right)$ and reflected $\left({}_kV_i^R\right)$ pulses to the node and the relationship between them. This relationship between $\left({}_kV_i^I\right)$ and $\left({}_kV_i^R\right)$ will be derived using a general approach based on replacing each of the

line segment by its Thevenin equivalent. For each segment, this consists of a voltage $2_kV_i^I$ in series with the impedance Z_i (derived from 1-D TLM model). The equivalent circuit for the regular mesh is the following (using the same technique seen for the 1-D case)

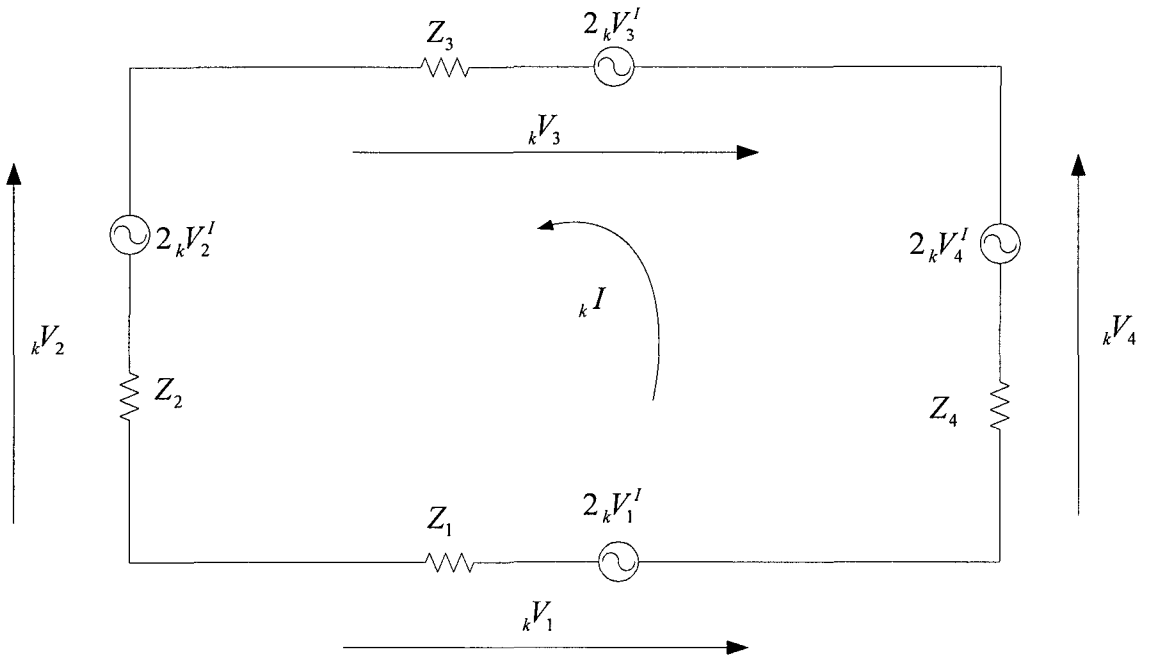

Figure 3-19 Thevenin equivalent circuit for the 4 lines intersecting in the ith node of the mesh

Using the same methodology in the one dimensional TLM modeling, the current in the circuit is

$$_kI = \frac{2_kV_1^I + 2_kV_4^I - 2_kV_3^I - 2_kV_2^I}{Z_1 + Z_2 + Z_3 + Z_4}. \tag{3-40}$$

The reflected voltages can be obtained from the general expression

$$_kV_i^R = {}_kV_i - {}_kV_i^I,\ i = 1,2,3,4, \tag{3-41}$$

where $_kV_i$ is the total voltage at time step k in the segment i.

Since $\begin{matrix} _kV_i = 2_kV_i^I + {}_kIZ_i, i = 2,3 \\ _kV_i = 2_kV_i^I - {}_kIZ_i, i = 1,4 \end{matrix}$, thus

$$
\begin{aligned}
{}_kV_i^R &= {}_kV_i^I + {}_kIZ_i, i = 2,3 \\
{}_kV_i^R &= {}_kV_i^I - {}_kIZ_i, i = 1,4
\end{aligned}
\tag{3-42}
$$

Substituting ${}_kI$ by its expression we obtain the following

$$
\begin{aligned}
{}_kV_i^R &= {}_kV_i^I + \frac{2Z_i}{Z_1+Z_2+Z_3+Z_4}\left({}_kV_1^I + {}_kV_4^I - {}_kV_3^I - {}_kV_2^I\right), i = 2,3 \\
{}_kV_i^R &= {}_kV_i^I - \frac{2Z_i}{Z_1+Z_2+Z_3+Z_4}\left({}_kV_1^I + {}_kV_4^I - {}_kV_3^I - {}_kV_2^I\right), i = 1,4
\end{aligned}
\tag{3-43}
$$

Finally the scattering matrix is

$$
\begin{bmatrix} {}_kV_1^R \\ {}_kV_2^R \\ {}_kV_3^R \\ {}_kV_4^R \end{bmatrix} = 0.5 \begin{bmatrix} 1 & 1 & 1 & -1 \\ 1 & 1 & -1 & 1 \\ 1 & -1 & 1 & 1 \\ -1 & 1 & 1 & 1 \end{bmatrix} \begin{bmatrix} {}_kV_1^I \\ {}_kV_2^I \\ {}_kV_3^I \\ {}_kV_4^I \end{bmatrix}.
\tag{3-44}
$$

3.1.4.5. 2-D TLM scattering in a regular mesh for TM mode

The same parameters and notation as for the "***2-D TLM scattering in a regular mesh for TE mode***" section will be used. The scattering properties will be derived using the same approach where each line is replaced by its Thevenin circuit.

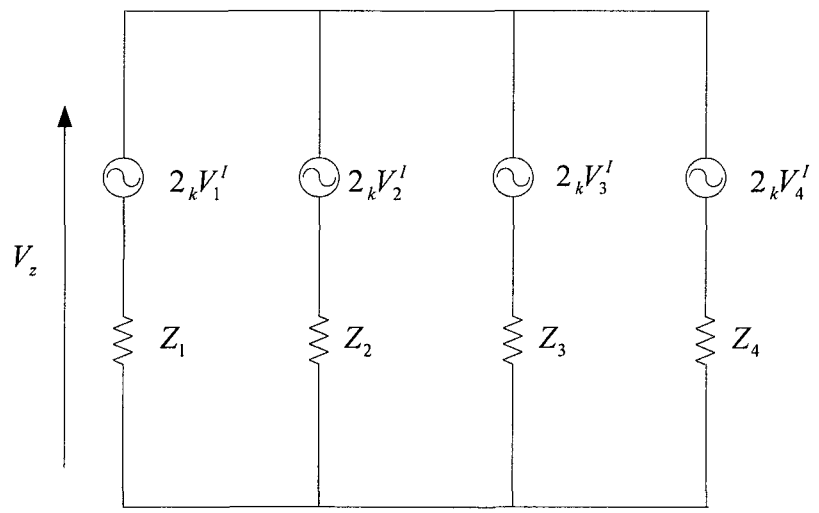

Figure 3-20 Thevenin equivalent circuit for the 4 lines intersecting the shunt node of the mesh

From Figure 3-20 the following relationship can be derived

$$V_z = 0.5\left({}_kV_1^I + {}_kV_2^I + {}_kV_3^I + {}_kV_4^I\right). \tag{3-45}$$

The scattered voltages are obtained from the relationship used in the previous section ${}_kV_i^R = {}_kV_i - {}_kV_i^I, i = 1,2,3,4$ but with just substituting ${}_kV_i$ by V_z

$${}_kV_i^R = 0.5\left({}_kV_1^I + {}_kV_2^I + {}_kV_3^I + {}_kV_4^I\right) - {}_kV_i^I, i = 1,2,3,4. \tag{3-46}$$

The scattering matrix for the shunt node

$$\begin{bmatrix} {}_kV_1^R \\ {}_kV_2^R \\ {}_kV_3^R \\ {}_kV_4^R \end{bmatrix} = 0.5\begin{bmatrix} -1 & 1 & 1 & 1 \\ 1 & -1 & 1 & 1 \\ 1 & 1 & -1 & 1 \\ 1 & 1 & 1 & -1 \end{bmatrix}\begin{bmatrix} {}_kV_1^I \\ {}_kV_2^I \\ {}_kV_3^I \\ {}_kV_4^I \end{bmatrix}. \tag{3-47}$$

3.2. Analogy between EMF, Sound Waves and TLM

Recall that the governing equations for EMF and Sound wave problems in the 2-D configuration are the following (27). The Maxwell equations describing the EMF waves are

$$\begin{cases} \dfrac{\partial E_z}{\partial x} = \mu \dfrac{\partial H_y}{\partial t} \\ \dfrac{\partial E_z}{\partial y} = -\mu \dfrac{\partial H_x}{\partial t} \\ \dfrac{\partial H_y}{\partial x} - \dfrac{\partial Hx}{\partial y} = \varepsilon \dfrac{\partial E_z}{\partial t} \end{cases}, \tag{3-48}$$

where E and H are the Electric and magnetic fields, μ and ε are the permeability and permittivity of the space.

The sound wave set of equations is

$$\begin{cases} \dfrac{\partial P}{\partial x} = -\rho \dfrac{\partial U_x}{\partial t} \\ \dfrac{\partial P}{\partial y} = -\rho \dfrac{\partial U_y}{\partial t} \\ -\dfrac{\partial U_x}{\partial x} - \dfrac{\partial U_y}{\partial y} = \sigma \dfrac{\partial P}{\partial t} \end{cases} . \tag{3-49}$$

From these two set of equations an analogy can be made

EMF parameters	Sound wave parameters
E_z	P
$-H_y$	U_x
H_x	U_y
μ	ρ
ε	σ

Table 3-1 Analogy between EMF and Sound waves parameters

Here, P [Pascal, P] is the pressure, U_x and U_y [meters per second, ms^{-1}] are the pressure velocity components in x and y directions, ρ [Kilograms per cubic meters, Kgm^{-3}] is the density of the medium and σ [P^{-1}] is the compressibility of the medium.

On the other hand a two dimensional element of a medium of dimensions u and v, is represented by a node intersected by two transmission lines in the x and y directions. If C is the total capacitance of this element and L_x, L_y are the total inductances for the two lines in x and y directions respectively, then the voltage/current differential equations are

$$\begin{cases} \dfrac{\partial V_z}{\partial x} = -\dfrac{L_x}{u}\dfrac{\partial I_x}{\partial t} \\ \dfrac{\partial V_z}{\partial y} = -\dfrac{L_y}{v}\dfrac{\partial I_y}{\partial t} \\ -u\dfrac{\partial I_x}{\partial x} - v\dfrac{\partial I_y}{\partial y} = C\dfrac{\partial V_z}{\partial t} \end{cases} . \tag{3-50}$$

Taking the system of equations in (3-50), some intermediate modifications should be done to conclude about the analogy with EMF or Sound Waves.

Here w is an arbitrary distance inserted to retain the correct dimensionality when dividing I_x and I_y by v and u respectively,

$$\begin{cases} w\dfrac{\partial\left(\dfrac{V_z}{w}\right)}{\partial x} = v\dfrac{L_x}{u}\dfrac{\partial\left(-\dfrac{I_x}{v}\right)}{\partial t} \\ w\dfrac{\partial\left(\dfrac{V_z}{w}\right)}{\partial y} = -u\dfrac{L_y}{v}\dfrac{\partial\left(\dfrac{I_y}{u}\right)}{\partial t} \\ uv\dfrac{\partial\left(-\dfrac{I_x}{v}\right)}{\partial x} - vu\dfrac{\partial\left(\dfrac{I_y}{u}\right)}{\partial y} = wC\dfrac{\partial\left(\dfrac{V_z}{w}\right)}{\partial t} \end{cases} . \tag{3-51}$$

This is equivalent to

$$\begin{cases} \dfrac{\partial\left(\dfrac{V_z}{w}\right)}{\partial x} = \dfrac{L_x v}{uw}\dfrac{\partial\left(-\dfrac{I_x}{v}\right)}{\partial t} \\ \dfrac{\partial\left(\dfrac{V_z}{w}\right)}{\partial y} = -\dfrac{L_y u}{vw}\dfrac{\partial\left(\dfrac{I_y}{u}\right)}{\partial t} \\ \dfrac{\partial\left(-\dfrac{I_x}{v}\right)}{\partial x} - \dfrac{\partial\left(\dfrac{I_y}{u}\right)}{\partial y} = \dfrac{Cw}{uv}\dfrac{\partial\left(\dfrac{V_z}{w}\right)}{\partial t} \end{cases} . \tag{3-52}$$

Equation (3-52) compared to equation (3-48) will give the following analogy

EMF Parameters	Electric Circuit Parameters for the Transmission Line (TL)
E_z	$\dfrac{V_z}{w}$
$-H_y$	$\dfrac{I_x}{v}$
H_x	$\dfrac{I_y}{u}$
μ	$\dfrac{L_y u}{vw}$ or $\dfrac{L_x v}{uw}$
ε	$\dfrac{Cw}{uv}$

Table 3-2 Analogy between EMF and TL parameters

From this analogy the electric and magnetic fields of the EMF problem could be solved through the TLM method by considering them as the transmission line voltage and currents respectively. The same thing applies for the sound wave problem (wave

equation), where the amplitudes are calculated via the voltages traveling in the TLM model.

3.3. TLM model of the ultrasound propagation in tissues

Ultrasound waves have the same properties as sound waves. They obey the same wave propagation law. The interest that ultrasonics have gained is due to the increase in its diverse applications. Amongst that, ultrasonic techniques were applied in medicine, both as a diagnostic tool and as a therapeutic modality. Although ultrasound has been used in medicine since the 1930's, it is only recently that these techniques have been widely used and their ability fully recognized. Most of the time an image of the organ to be examined is offered. Radio-frequency signals could be also recorded for post-processing purposes. All of this data is purely experimental and most of the time there is no clear knowledge on how and why these ultrasonic waves are propagating.

In this section a physics-based numerical model is developed using TLM method to mimic the ultrasound wave propagation and behavior in a rectangular medium. Since we are interested in IVUS and the medium is circular, a small portion of the artery cross-section that has a rectangular shape can be studied independently.

3.3.1. IVUS regular TLM model

A section of the artery is modeled by a rectangular shape using TLM (Figure 3-21). The code was developed in Matlab. In order to construct the TLM model many basic parameters should be provided. The size of the medium, the gridding rate, the boundary termination and the wave source location are the most important data to be known in the modeling process.

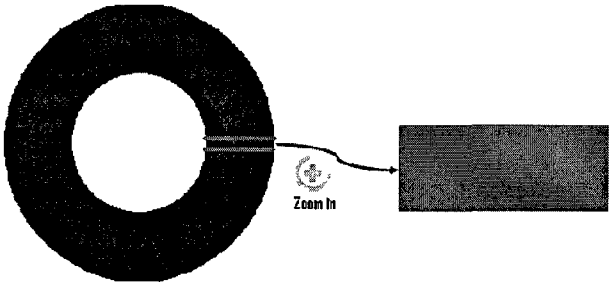

Figure 3-21 Rectangular approximation of a portion of the artery cross-section

3.3.1.1. Auto-generated regular mesh

It will be shown that the medium will be automatically generated from the developed TLM code once the dimensions are specified. Given the inner and outer radii of the artery cross-section, an automated rectangular mesh is generated. Since TLM model is based on the nodes and lines of the discretized medium, the number of horizontal and vertical nodes as well as the lines lengths are function of the indicated gridding rates. The model is based on regular TLM; therefore the lines are equal in length in both directions. Figure 3-22 illustrates a discretized medium that is composed of a 51 by 51 nodes mesh. The developed code was designed in a manner where the user can input both the dimensions and the gridding rate of the rectangular medium to guarantee the flexibility in using these parameters to cover a wide range of arteries.

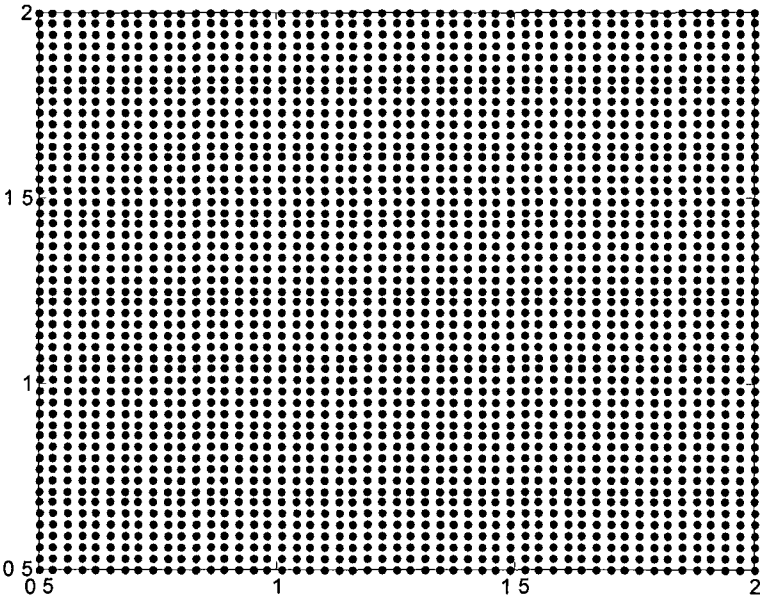

Figure 3-22 Auto-generated mesh of 51 by 51 nodes

3.3.1.2. Boundary termination

As the TLM is a numerical method, the medium should be of a finite size. This is known as medium termination. This is presented by a wall that is characterized by the same acoustic impedance of the terminated medium. For example if the external medium

that comes after the artery is air, then the wall that models the termination of air is characterized by the acoustic impedance of the air.

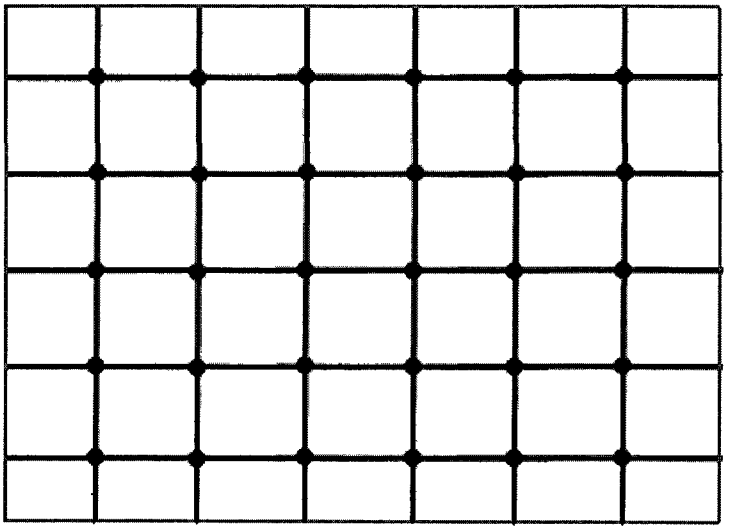

Figure 3-23 Boundary walls (red lines) terminating the rectangular medium

Taking one element of the above Figure 3-23, that lies next to the boundary wall of the medium (upper right corner) as illustrated in Figure 3-24, the reflection of the voltages components obey to

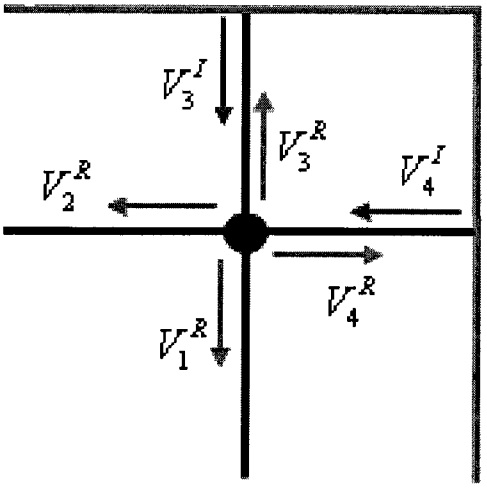

Figure 3-24 Reflection of the voltages (or sound waves pressure amplitudes) from the boundary walls

$$V_3^I = \frac{Z_{out} - Z_{medium}}{Z_{out} - Z_{medium}} V_3^R,$$
$$V_4^I = \frac{Z_{out} - Z_{medium}}{Z_{out} - Z_{medium}} V_4^R, \tag{3-53}$$

where Z_{out} is the acoustic impedance of the outer medium next to the boundary walls and Z_{medium} is the acoustic impedance of the medium itself respectively.

The acoustic impedance is the product of the density of the medium and the sound speed in the medium, i.e., $Z = \rho c$.

There is an extensive use of what is called absorbing wall or attenuating wall where the impedance of the outer medium to the artery portion is considered to have impedance that is almost equal to the one of the artery. This is used to get eliminate the reflection effects on the sound waves that propagate inside the modeled medium of interest.

3.3.1.3. Wave Source generation and wave propagation

The design of the wave source has been widely studied for the IVUS. In the TLM model, flexibility is given in the code to design any kind of source waves. Since Matlab is the platform where the code was developed, SIMULINK toolbox is used for the source wave specifications. This toolbox offers a variety of signals some of them are illustrated in Figure 3-25.

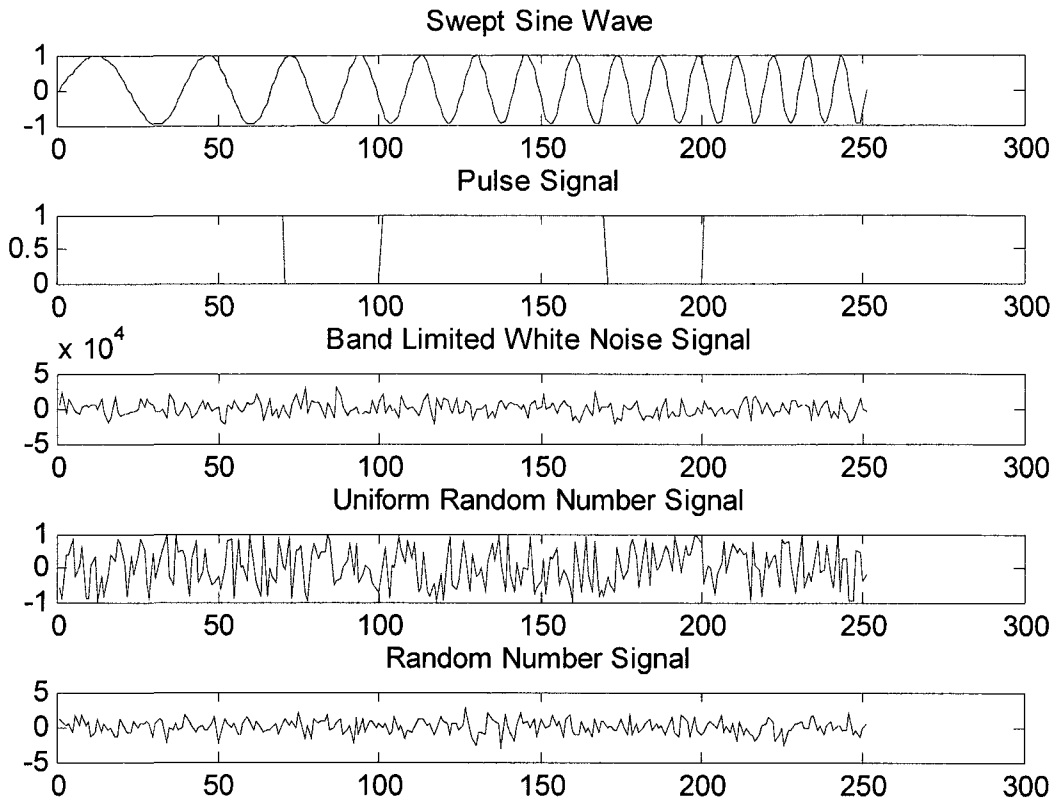

Figure 3-25 Examples of different source waves designed by SIMULINK

In addition to the wide range of source waves, this model gives the possibility of specifying any location in the mesh to be the source point where the ultrasonic wave starts to propagate. For instance the source could be in one node of the edges of the medium, inside the medium or in different nodes at the same time.

The propagation process is based in the Huygens principle where for a given node in the mesh, the reflected amplitudes going out at time k will serve as the incident waves to the surrounding nodes at time $k + 1$ (Figure 3-26) (1).

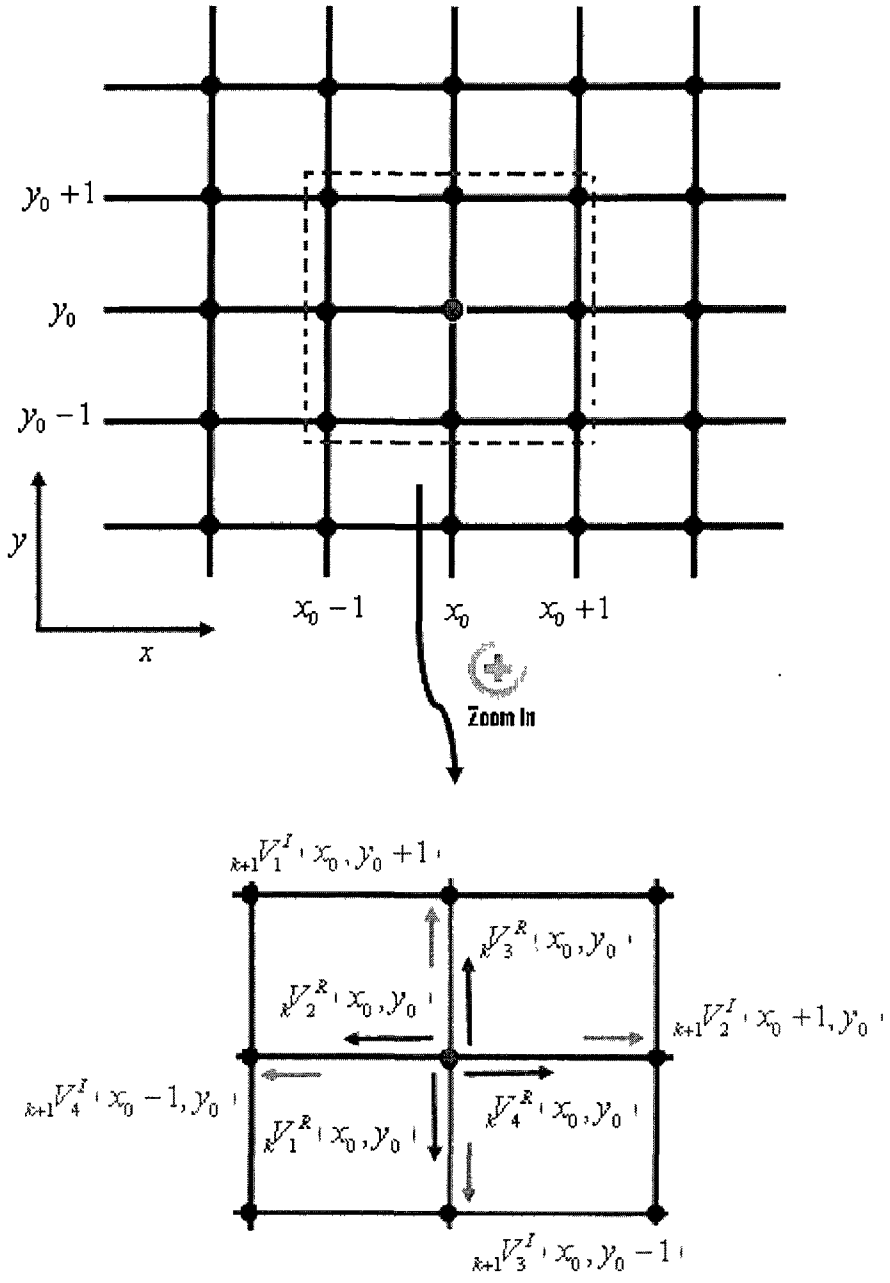

Figure 3-26 Traveling process of the wave between the nodes

$$
\begin{aligned}
{}_kV_1^R(x_0, y_0) &= {}_{k+1}V_3^I(x_0, y_0-1) \\
{}_kV_2^R(x_0, y_0) &= {}_{k+1}V_4^I(x_0-1, y_0) \\
{}_kV_3^R(x_0, y_0) &= {}_{k+1}V_1^I(x_0, y_0+1) \\
{}_kV_4^R(x_0, y_0) &= {}_{k+1}V_2^I(x_0+1, y_0)
\end{aligned}
\tag{3-54}
$$

3.3.2. Model Validation:

The regular TLM models were established in numerous fields in the literature. Since the IVUS regular TLM model was developed independently in Matlab, the results generated will be compared to a model developed in the literature to validate the code (28). A square medium composed of 215 by 215 nodes is investigated. The source location is taken at node (2,100) where the source wave is a sinusoidal excitation (Figure 3-27).

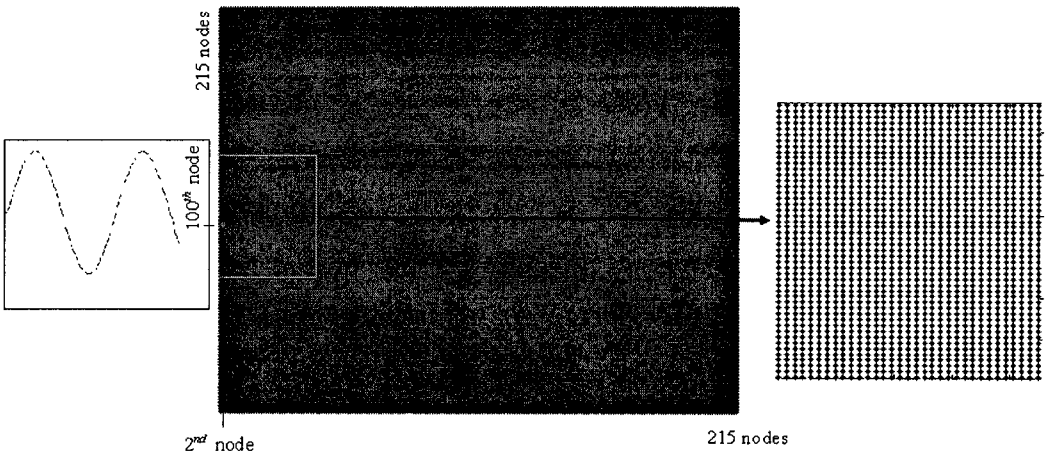

Figure 3-27 Validation model of the regular TLM

The amplitudes of the propagation wave can be recorded in different locations of the medium at any time. Using the developed code and the TLM model from the literature the recorded signals are plotted and compared. Three different locations were taken to compare the ultrasonic wave that is propagating. Nodes (2,100), (20,100) and (30,100) were taken. In Figure 3-28 the waves are plotted for both models. Superposition of the plots from the two models proves that the waves are the same (Figure 3-29).

Once the developed TLM code is validated, this method will be used to model the anomalies and artifacts that could form inside the artery cross-section. This will lead to a deeper analysis and understanding of the ultrasound wave propagation through healthy and plaque burden (hard and soft plaque) segments.

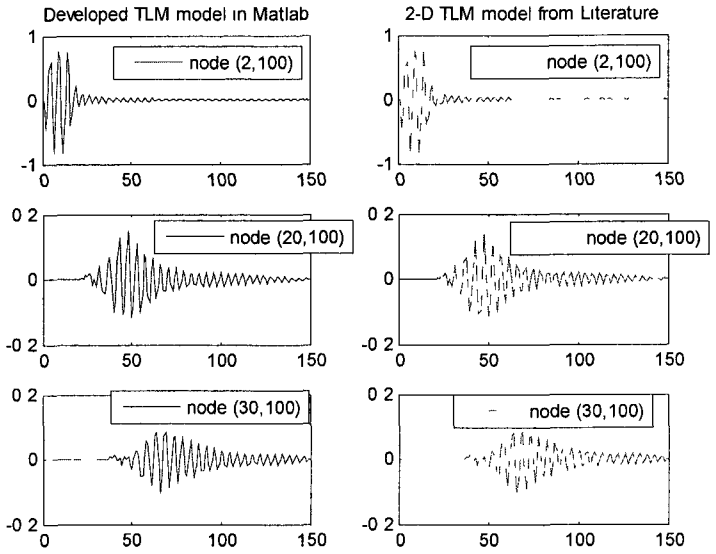

Figure 3-28 Generated waves for different locations of the medium

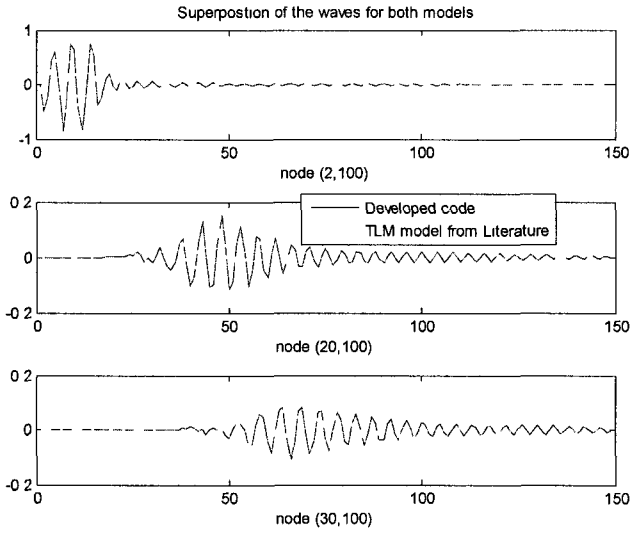

Figure 3-29 Validation of the results for the developed TLM code versus an established literature model

3.3.3. Plaque model

The main goal of this work besides mimicking the ultrasound propagation in the artery cross-section is the characterization of the different tissues especially the abnormalities that could form in the artery. In this section, a plaque model will be developed where an inclusion in inserted in the rectangular medium. In addition to the

geometric shape of the inclusion that is added to the TLM model, the interactions between the medium (artery/ normal tissue) and the abnormal formation will be established. Illustrated in Figure 3-30 is the case where artery contains a plaque (Yellow colored region).

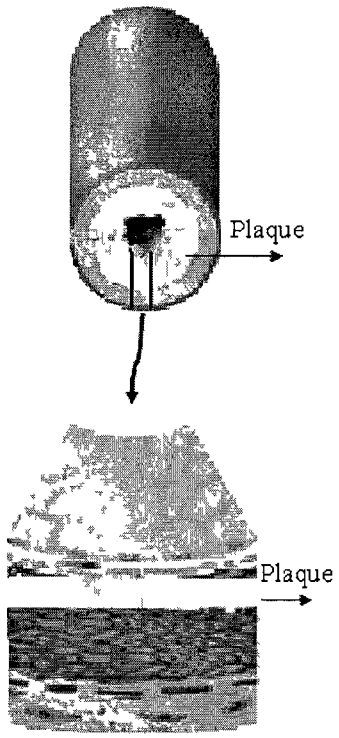

Figure 3-30 Plaque in the artery (http://yoursurgery.com)

The TLM model will consider the plaque as a rectangular object that is inserted inside the artery portion presented by the rectangular medium (Figure 3-31).

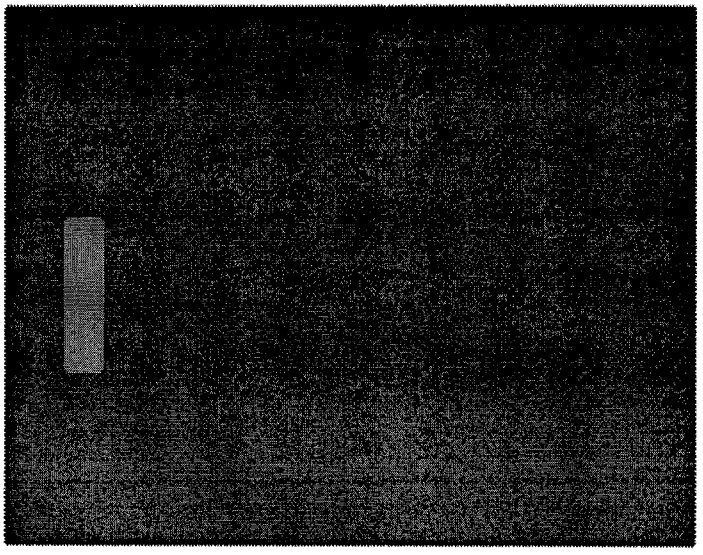

Figure 3-31 Structure of the TLM model where a plaque is inserted

The plaque (inclusion) that is formed inside the artery is characterized by different acoustic properties. In fact the ultrasound speed and density are not the same as of the normal tissue (i.e. different acoustic impedances). This will produce a boundary between the healthy portion of the artery and the abnormality edge. This boundary characterizes a change in impedances. This will produce a reflection/transmission phenomenon due to this change along the four edges of the plaque. Considering $Z_{Plaque} = c_{Plaque}\rho_{PLaque}$ and $Z_{Artery} = c_{artery}\rho_{Artery}$ to be the acoustic impedances of the plaque and artery, then the reflection and transmission coefficients are

$$R = \frac{Z_{Plaque} - Z_{Artery}}{Z_{Plaque} + Z_{Artery}}$$

$$T = 1 - \frac{Z_{Plaque} - Z_{Artery}}{Z_{Plaque} + Z_{Artery}}. \tag{3-55}$$

The transmission and reflection that occur on both sides of the boundary are function of these coefficients. The reflected and transmitted components of the wave amplitudes in the nodes neighboring the four edges of the plaque will be derived from the voltages traveling between the lines of the mesh.

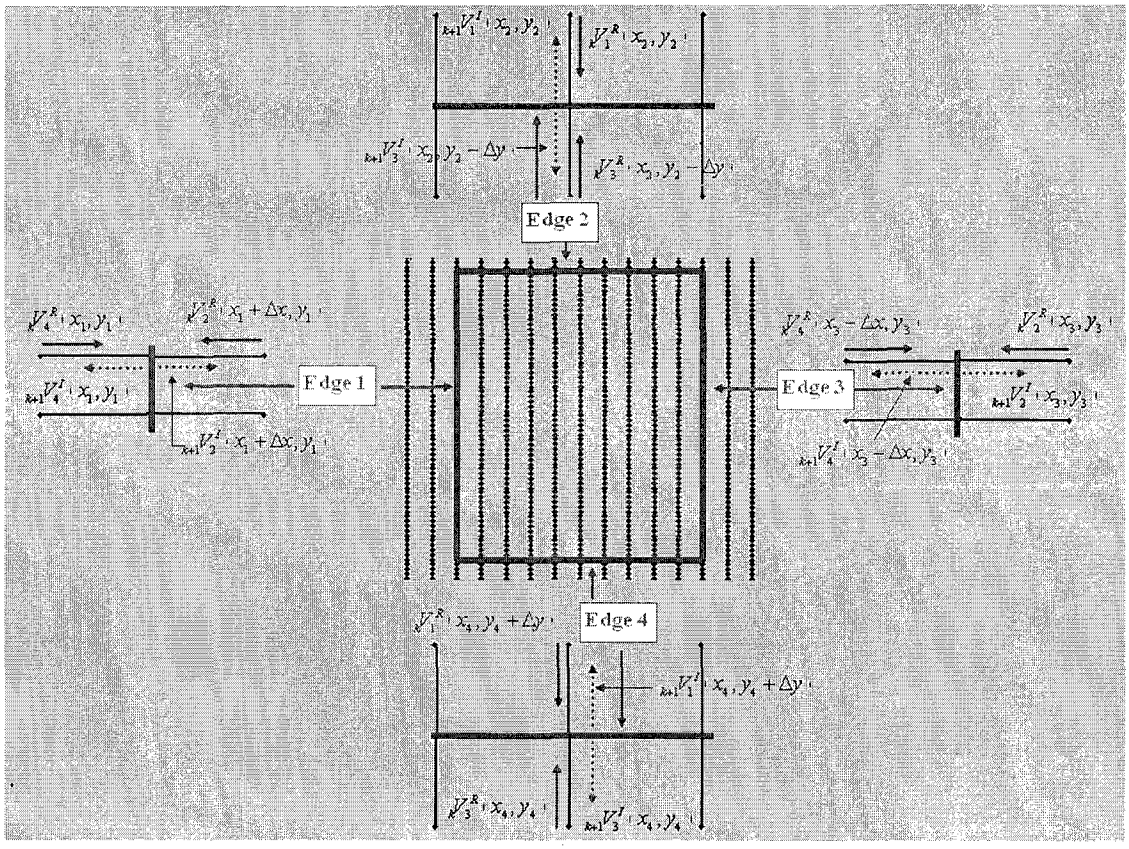

Figure 3-32 Reflection and transmission of the wave at the four edges of the plaque

In Figure 3-32, the dotted arrows are the reflected and transmitted ultrasound wave components. Whereas the solid arrows are the scattered amplitudes of the wave coming from the nodes surrounding the plaque edges before hitting these edges. The reflected and transmitted waves' expressions will be detailed for all edges of the plaque

<u>Edge 1</u>

$$
\begin{aligned}
{}_{k+1}V_4^I(x_1,y_1) &= R_k V_4^R(x_1,y_1) + (1+R)_k V_2^R(x_1+\Delta x, y_1) \\
{}_{k+1}V_2^I(x_1+\Delta x, y_1) &= -R_k V_2^R(x_1+\Delta x, y_1) + T_k V_4^R(x_1,y_1).
\end{aligned}
\tag{3-56}
$$

<u>Edge 2</u>

$$
\begin{aligned}
{}_{k+1}V_1^I(x_2,y_2) &= R_k V_1^R(x_2,y_2) + (1+R)_k V_3^R(x_2, y_2-\Delta y) \\
{}_{k+1}V_3^I(x_2,y_2-\Delta y) &= T_k V_1^R(x_2,y_2) - R_k V_3^R(x_2, y_2-\Delta y).
\end{aligned}
\tag{3-57}
$$

<u>Edge 3</u>

$$
\begin{aligned}
{}_{k+1}V_2^I(x_3, y_3) &= R_k V_2^R(x_3, y_3) + (1+R)_k V_4^R(x_3 - \Delta x, y_3) \\
{}_{k+1}V_4^I(x_3 - \Delta x, y_3) &= T_k V_2^R(x_3, y_3) - R_k V_4^R(x_3 - \Delta x, y_3).
\end{aligned}
\tag{3-58}
$$

Edge 4

$$
\begin{aligned}
{}_{k+1}V_3^I(x_4, y_4) &= R_k V_3^R(x_4, y_4) + (1+R)_k V_1^R(x_4, y_4 + \Delta x) \\
{}_{k+1}V_1^I(x_4, y_4 + \Delta x) &= T_k V_3^R(x_4, y_4) - R_k V_1^R(x_4, y_4 + \Delta x).
\end{aligned}
\tag{3-59}
$$

Depending on the acoustic characteristics of the plaque the propagation of the wave will show different behavior. As an example to illustrate the effect of the plaque, three different acoustic impedances are taken. A swept sine wave is designed to be the source signal at the node (1st horizontal, 45th vertical). The medium is composed of 751 by 76 nodes and the plaque is located between the 20th and 30th node in the horizontal direction and the 25th and 65th node in the vertical direction (Figure 3-33).

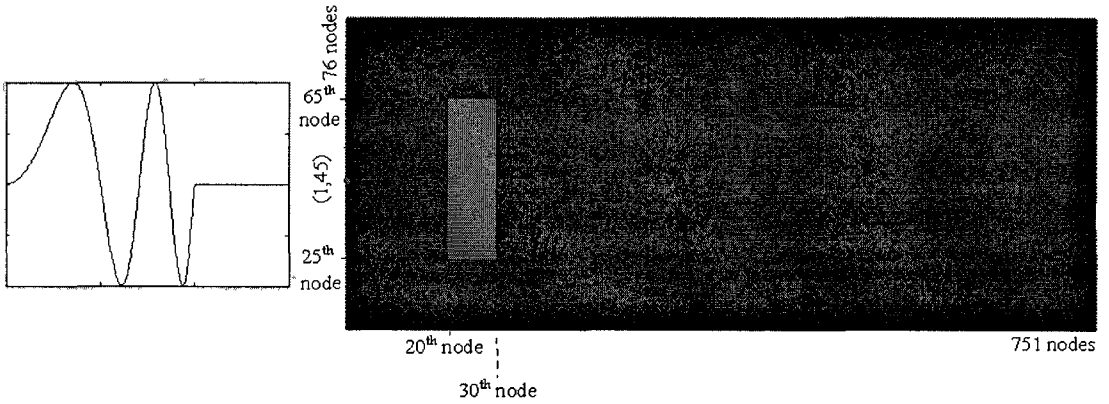

Figure 3-33 Plaque example generated by the developed 2-D TLM model

The time signals are plotted in different locations (Figure 3-34). The plots show how the plaque nature plays an important role in determining the ultrasound wave behavior. As mentioned before, the IVUS is just providing the experimental record of the radio-frequency signals that are reflected back. Thus building several models that present different inclusions in terms of geometry and acoustic properties will be of great benefit to study the behavior of the waves in the presence of such abnormalities. Figure 3-35 is an illustration of the plaque influence on the determination of the wave shape. This model could be extended to study numerous cases where all combinations of abnormalities can be constructed.

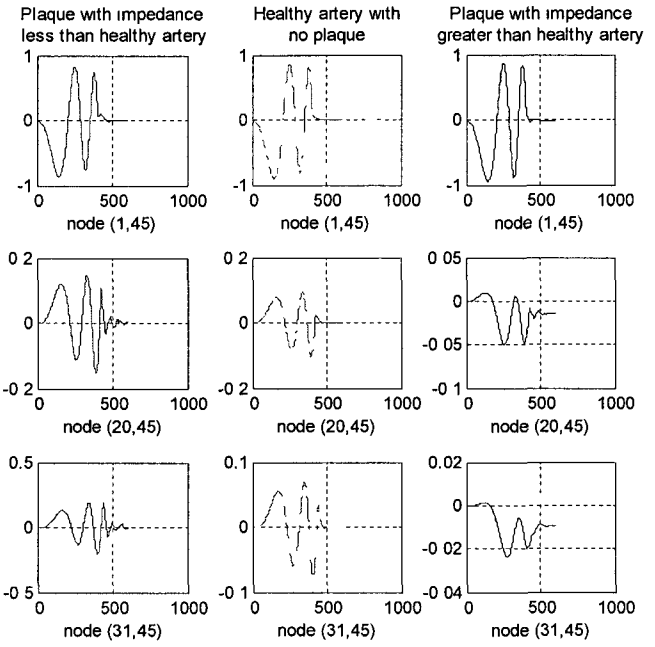

Figure 3-34 plaque effect on the signals at different locations ($Z_{Hardinclusion} = 7.4Z_{Healthyartery}$ and $Z_{Softinclusion} = 0.074Z_{Healthyartery}$)

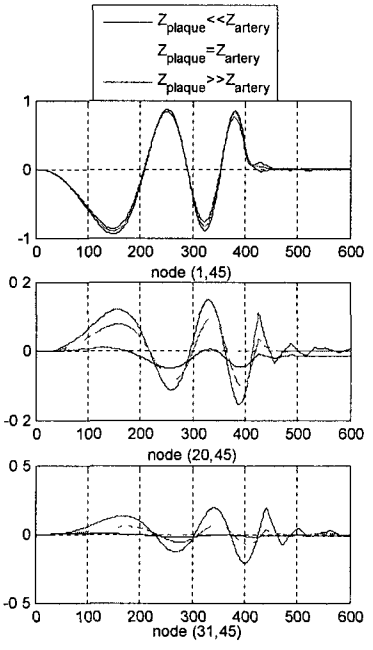

Figure 3-35 Comparison of the time signals ($Z_{Hardinclusion} = 7.4Z_{Healthyartery}$ and $Z_{Softinclusion} = 0.074Z_{Healthyartery}$)

3.4. Summary

In this chapter, the basis of the TLM method was introduced. Then 1-D model was studied where the propagation process of the voltages was defined. The 1-D TLM form was extended to a two dimensional model. After that, it was shown how a 2-D TLM model can serve as a numerical tool to capture the sound wave propagation in a regular medium. Specifically this model was employed to mimic the ultrasound propagation inside an artery cross-section. Consequently a model for the IVUS was built where abnormalities could be introduced and studied. The information provided in terms of time signals will serve later on as a niche from which system identification techniques are used to analyze and characterize the plaques.

Given that the established model represents just a portion of the artery cross-section, a more realistic approach in modeling the IVUS would be more appropriated and accurate to characterize all the artery tissue components. The following chapter will be dedicated to establish a new model that takes into account the whole irregular (circular) geometry of the artery cross-section.

Chapter 4 Irregular transmission line matrix model for intravascular ultrasound

The regular TLM models presented in Chapter 3 have been used extensively to solve general sound wave propagation problems in two dimensions. It was shown in the previous chapter that TLM can capture the dynamics of ultrasound wave propagation through the wall of an artery. However these models are limited to a mesh comprised of nodes forming a square. There are applications, such as arteries, when the medium geometry is complex (curved or circular shapes) that the use of the regular TLM method is not appropriate to solve numerically the sound wave equation. This restriction on the shape and size of the mesh affects the capability of the conventional regular TLM method. Moreover the employment of the conventional TLM where the shape is irregular necessitates the use of finer meshes to represent these irregularities accurately. This represents a burden in terms of memory use and run time for numerical computations. In this chapter, TLM mesh and model will be developed for the whole artery cross-section. Having an irregular mesh, a new generalized TLM formulation will be derived. This model will be adapted to the circular shape of the artery case. This irregular model will be validated against a well established regular Cartesian TLM model. The IVUS model will be, finally, constructed through the new established irregular TLM method.

4.1. Irregular TLM model Formulation

The regular TLM model is characterized by equally spaced nodes. Thus the scattering matrix is independent of the lines lengths and the medium properties. In the case of irregular mesh, the scattering process is function of the medium properties as well as the lines linking the different nodes of the discretized medium. Presented is the foundation of the irregular TLM method in the two dimensional case.

4.1.1. Governing Equations

Equivalence between electrical circuit parameters and electromagnetic field parameters for the regular TLM were derived without introducing any of the line lengths. These lengths were in fact normalized to unity since the length is always the same in all directions. A two dimensional element of a medium having differing dimensions u and v, is represented by a node intersected by two transmission lines in x and y directions.

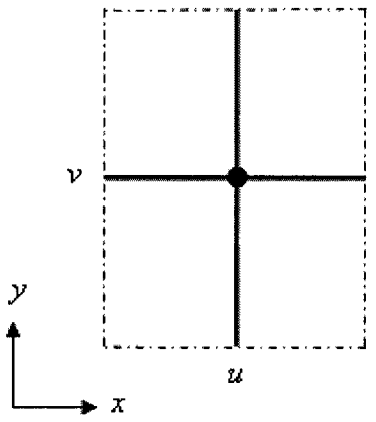

Figure 4-1 Irregularly spaced element

If C is the total capacitance and L_x, L_y are the total inductances for the two lines in x and y directions respectively, then the voltage/current differential equations are (27):

$$\begin{cases} \dfrac{\partial V_z}{\partial x} = -\dfrac{L_x}{u}\dfrac{\partial I_x}{\partial t} \\ \dfrac{\partial V_z}{\partial y} = -\dfrac{L_y}{v}\dfrac{\partial I_y}{\partial t} \\ -u\dfrac{\partial I_x}{\partial x} - v\dfrac{\partial I_y}{\partial y} = C\dfrac{\partial V_z}{\partial t} \end{cases} . \tag{4-1}$$

Taking the system of equations in (3-50), some intermediate modifications must be done to make the analogy with EMF TM mode (sound waves). Let w be an arbitrary distance inserted to retain the correct dimensionality when dividing I_x and I_y by v and u respectively,

$$\begin{cases} w\dfrac{\partial\left(\dfrac{V_z}{w}\right)}{\partial x} = v\dfrac{L_x}{u}\dfrac{\partial\left(-\dfrac{I_x}{v}\right)}{\partial t} \\ w\dfrac{\partial\left(\dfrac{V_z}{w}\right)}{\partial y} = -u\dfrac{L_y}{v}\dfrac{\partial\left(\dfrac{I_y}{u}\right)}{\partial t} \\ uv\dfrac{\partial\left(-\dfrac{I_x}{v}\right)}{\partial x} - vu\dfrac{\partial\left(\dfrac{I_y}{u}\right)}{\partial y} = wC\dfrac{\partial\left(\dfrac{V_z}{w}\right)}{\partial t} \end{cases} . \tag{4-2}$$

This is equivalent to

$$\begin{cases} \dfrac{\partial\left(\dfrac{V_z}{w}\right)}{\partial x} = -\dfrac{L_x v}{uw}\dfrac{\partial\left(\dfrac{I_x}{v}\right)}{\partial t} \\ \dfrac{\partial\left(\dfrac{V_z}{w}\right)}{\partial y} = -\dfrac{L_y u}{vw}\dfrac{\partial\left(\dfrac{I_y}{u}\right)}{\partial t} \\ -\dfrac{\partial\left(\dfrac{I_x}{v}\right)}{\partial x} - \dfrac{\partial\left(\dfrac{I_y}{u}\right)}{\partial y} = \dfrac{Cw}{uv}\dfrac{\partial\left(\dfrac{V_z}{w}\right)}{\partial t} \end{cases} . \tag{4-3}$$

Now consider the ultrasound wave equation

$$\begin{cases} \dfrac{\partial P}{\partial x} = -\rho \dfrac{\partial U_x}{\partial t} \\ \dfrac{\partial P}{\partial y} = -\rho \dfrac{\partial U_y}{\partial t} \\ -\dfrac{\partial U_x}{\partial x} - \dfrac{\partial U_y}{\partial y} = \sigma \dfrac{\partial P}{\partial t} \end{cases} . \tag{4-4}$$

Comparing equation (4-3) with equation (4-4) gives the following analogy

Ultrasound Waves Parameters	Electric Circuit Parameters for the Transmission Line (TL)
P	$\dfrac{V_z}{w}$
U_x	$\dfrac{I_x}{v}$
U_y	$\dfrac{I_y}{u}$
ρ	$\dfrac{L_y u}{vw}$ or $\dfrac{L_x v}{uw}$
σ	$\dfrac{Cw}{uv}$

Table 4-1 Analogy between EMF and TL parameters

From Table 4-1 the following relationships are obtained

$$\begin{cases} C = \sigma \dfrac{uv}{w} \\ L_x = \rho \dfrac{uw}{v} \\ L_y = \rho \dfrac{vw}{u} \end{cases} . \tag{4-5}$$

4.1.2.Cartesian two-dimensional irregular TLM

Time synchronism is conserved in the TLM (27). In fact, the transmitted pulse from one node must reach its surrounding nodes at the same time regardless the lines lengths linking these nodes in all direction (x and y directions in the 2-D case). This means that the velocity of propagation of the voltage in dependent on the lines lengths. Since the velocity is function of the total inductance and capacitance of the line ($V = \frac{1}{\sqrt{LC}}$), the inductance term is fixed and capacitance is calculated for each direction by taking into account the relationship between inductance, capacitance and velocity.

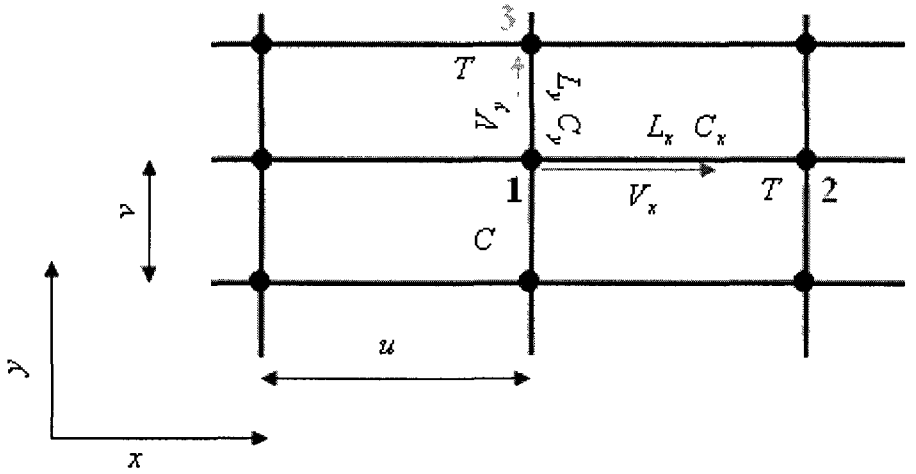

Figure 4-2 Time synchronism of the traveling process (T is constant)

For instance, in Figure 4-2 the time it takes for a given pulse to travel from node 1 to 2 and from node 1 to 3 must be equal. This is what is defined as the variable T in Figure 4-2.

In this section, a new approach is presented to circumvent the gridding irregularity such that time synchronism is realized. The following describes the steps for the calculation of the impedances based on this approach. An element of the mesh is taken with dimensions u and v in both directions (Figure 4-2). First a reference capacitance (which is the line compressibility in the sound wave case) $\frac{\sigma_0}{h}$ and inductance (which is the line density in the sound wave case) ρ_0 are assigned for the shortest piece of line that relates two consecutive nodes in the mesh. Here h is such that the following quantities are greater than zero

$$\begin{cases} \frac{wvh}{u}\rho_r - 1 \geq 0 \\ \frac{wuh}{v}\rho_r - 1 \geq 0 \end{cases}.$$

This is equivalent to

$$\begin{cases} \frac{wvh}{u}\rho_r \geq 1 \\ \frac{wuh}{v}\rho_r \geq 1 \end{cases} \Leftrightarrow \begin{cases} h \geq \frac{u}{wv\rho_r} \\ h \geq \frac{v}{wu\rho_r} \end{cases} \Leftrightarrow h \geq \sup\left(\frac{u}{wv\rho_r}, \frac{v}{wu\rho_r}\right)$$

$\rho_r = \frac{\rho}{\rho_0}$ is the ratio of a line inductance with respect to the smallest line inductance (which is the relative density in the sound wave case). Once the value of h is found, compressibility and density of this reference line are derived from the properties of the medium.

This line length is set to unity so the velocity along this reference line is equal to $V_{ref} = \frac{1}{\sqrt{L_{ref}C_{ref}}} = \frac{1}{T}$, with L_{ref} and C_{ref} being the inductance and capacitance of the reference line (i.e. $L_{ref} = \rho_0$ and $C_{ref} = \frac{\sigma_0}{h}$). The time T is the time that an impulse takes to travel along this link. This line is characterized by both speed and impedance,

$$\begin{cases} V_{ref} = \sqrt{\dfrac{h}{\rho_0 \sigma_0}} \\ Z_{ref} = \sqrt{\dfrac{h\rho_0}{\sigma_0}} \end{cases}. \tag{4-6}$$

From (4-5), the inductances per unit length in x and y directions are calculated

$$\begin{cases} L_{0x} = \dfrac{L_x}{u} \\ L_{0y} = \dfrac{L_y}{v} \end{cases},$$

$$\begin{cases} L_{0x} = \rho \dfrac{w}{v} \\ L_{0y} = \rho \dfrac{w}{u} \end{cases}. \tag{4-7}$$

From these inductances, the velocity in both directions are generated as

$$\begin{cases} V_x = \dfrac{1}{\sqrt{L_{0x} C_x}} = \dfrac{u}{T} \\ V_y = \dfrac{1}{\sqrt{L_{0y} C_y}} = \dfrac{v}{T} \end{cases}, \tag{4-8}$$

where C_x and C_y are capacitances per unit length in x and y directions. From the velocity of the reference line ($V_{ref} = \sqrt{\dfrac{h}{\rho_0 \sigma_0}} = \dfrac{1}{T}$) T is derived, $T = \sqrt{\dfrac{\rho_0 \sigma_0}{h}}$.

Solving for capacitances in equation (4-8) will lead to

$$\begin{cases} \dfrac{1}{L_{0x} C_x} = \left(\dfrac{u}{T}\right)^2 = \dfrac{u^2 h}{\rho_0 \sigma_0} \\ \dfrac{1}{L_{0y} C_y} = \left(\dfrac{v}{T}\right)^2 = \dfrac{v^2 h}{\rho_0 \sigma_0} \end{cases}.$$

Finally,

$$\begin{cases} C_x = \dfrac{\sigma_0 v}{u^2 h \rho_r w} \\ C_y = \dfrac{\sigma_0 u}{v^2 h \rho_r w} \end{cases}. \tag{4-9}$$

Once the capacitances per unit length are derived, the characteristic impedances in x and y directions are calculated based on the following formula $Z = \sqrt{\dfrac{L}{C}}$, giving

$$Z_x = \sqrt{\frac{L_{0x}}{C_x}} = \sqrt{\frac{\rho \dfrac{w}{v}}{\dfrac{\sigma_0 v}{u^2 h \rho_r w}}} = \sqrt{\frac{\rho w u^2 h \rho_r w}{v \sigma_0 v}} = \sqrt{\frac{\rho_0 \left(\dfrac{\rho}{\rho_0}\right) w^2 u^2 h \rho_r}{v^2 \sigma_0}} = \sqrt{\frac{w^2 u^2 \rho_r^2}{v^2} \frac{\rho_0 h}{\sigma_0}}.$$

Finally

$$\begin{cases} Z_x = \dfrac{w u \rho_r}{v} Z_{ref} \\ Z_y = \dfrac{w v \rho_r}{u} Z_{ref} \end{cases}. \tag{4-10}$$

Due to the irregular mesh grid, the total capacitances found in x and y directions, C_x and C_y are sometimes less than the total capacitance of the element C. A residual capacitance C_s is defined and modeled by an open-circuit stub at each node of the mesh (Figure 4-3).

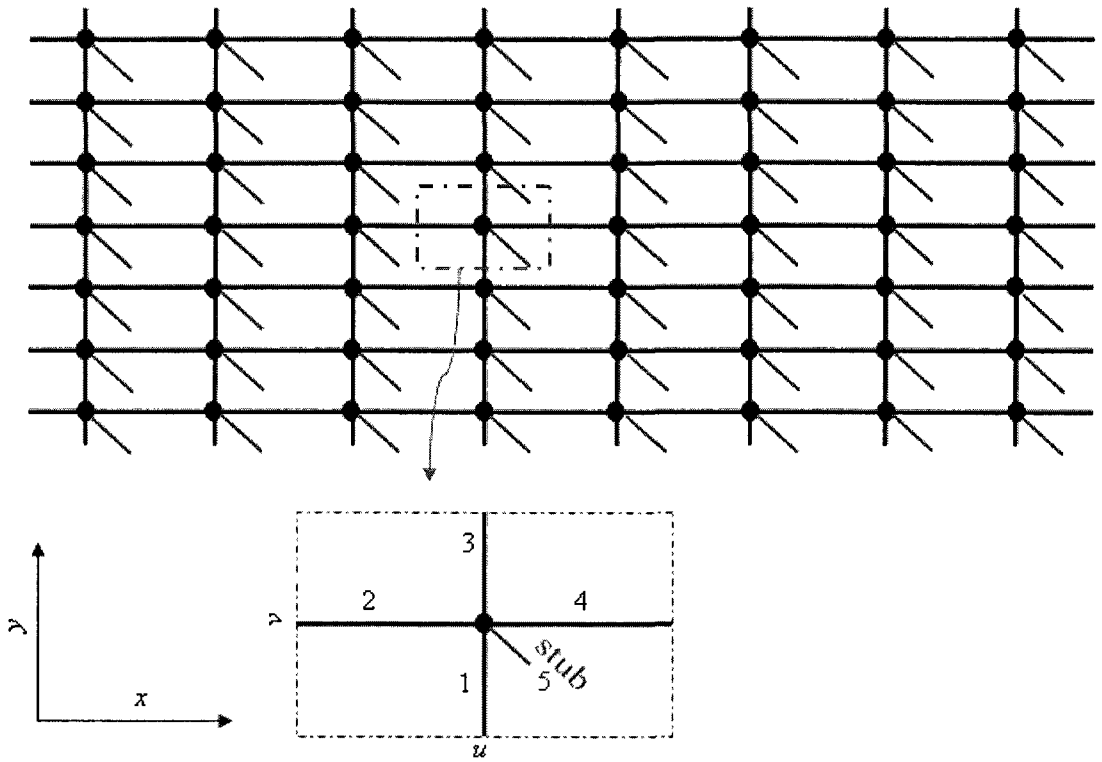

Figure 4-3 Stub represented by a new line added to the mesh at each node

$$C_s = C - (C_x + C_y) = \sigma\frac{uv}{w} - u\frac{\sigma_0 v}{u^2 h\rho_r w} - v\frac{\sigma_0 u}{v^2 h\rho_r w} = \sigma\frac{uv}{w} - \frac{\sigma_0 v}{uh\rho_r w} - \frac{\sigma_0 u}{vh\rho_r w}$$

$$C_s = \sigma\frac{uv}{w} - \frac{\sigma_0\left(u^2 + v^2\right)}{uvh\rho_r w} \tag{4-11}$$

The addition of the stub guarantees the time synchronism in irregular TLM. It is characterized by admittance $Z_5 = 2h\frac{C_s}{\sigma_0}$.

The admittance of the stub is

$$Z_5 = \frac{2\left[\sigma u^2 v^2 h\rho_r - \sigma_0\left(u^2 + v^2\right)\right]}{uvw\sigma_0\rho_r}. \tag{4-12}$$

Each element is characterized by four characteristic impedances corresponding to the four lines intersecting each node and an added stub characterized by its admittance.

4.1.3. Cylindrical Irregular TLM

The artery cross-section is presented by a disk. The coordinates system is characterized by the angle θ and the radial position r (polar coordinates) as illustrated in Figure 4-4.

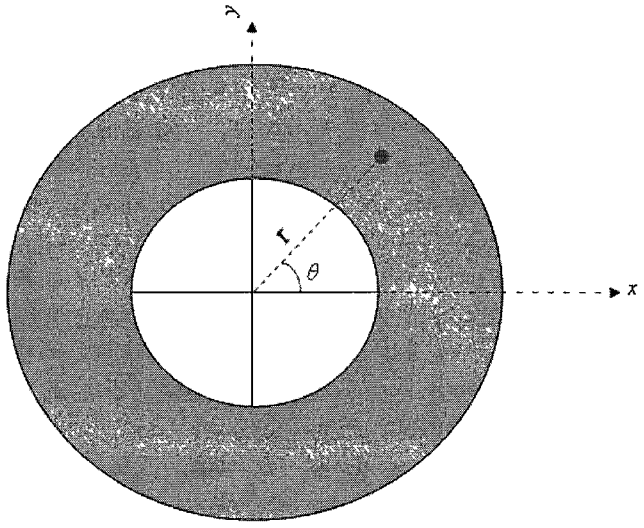

Figure 4-4 Circular geometry of the artery cross-section

In the TLM method, the discretization process of the medium will lead to an irregular gridding (Figure 4-5).

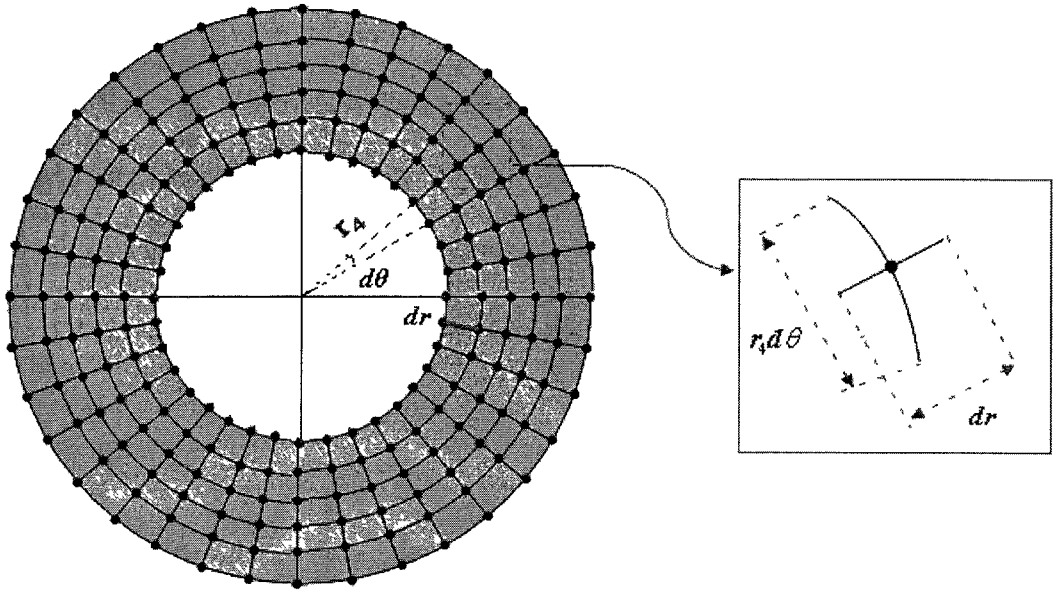

Figure 4-5 Irregular structure of a circular element of the cylindrical TLM model

In Figure 4-5, the node located in the 4th radial position is taken. The disk is discretized to a mesh characterized by a radial rate dr and angular rate $d\theta$. Since the selected node is located at a radial position equal to r_4, the radial and angular lines lengths intersecting this node are $u_r = dr$ and $u_\theta = r_4 d\theta$ respectively. In general for an arbitrary node that has a radial position r the element is characterized by the following lines lengths

$$\begin{cases} u_r = dr \\ u_\theta = r d\theta \end{cases}. \tag{4-13}$$

Obviously the nodes in this case are not equally spaced. Therefore the TLM model corresponds exactly to the same formulation detailed for the irregular Cartesian mesh. Consequently a stub line must be added to compensate for the residual capacitance caused by the length difference of the radial and angular lines of each element in the mesh. The element is characterized by radial and angular impedances and a stub admittance Z_r, Z_θ and Z_5.

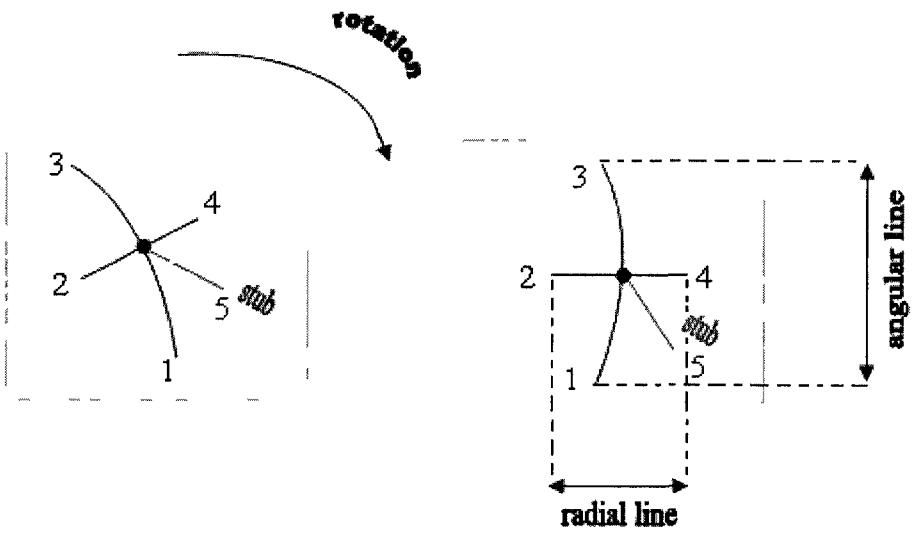

Figure 4-6 Added stub line to a circular element

In Figure 4-6, the radial line $[2,4]$, the angular line $[1,3]$ and the stub line are characterized respectively by Z_r, Z_θ and Z_5.

Recall (4-10) and (4-12), the radial, angular impedances and the stub admittance can be derived by replacing u by dr and v by $rd\theta$.

$$\begin{cases} Z_r = \dfrac{wdr\rho_r}{rd\theta} Z_{ref} \\ Z_\theta = \dfrac{wrd\theta\rho_r}{dr} Z_{ref} \\ Z_5 = \dfrac{2\left[\sigma(dr)^2(rd\theta)^2 h\rho_r - \sigma_0\left((dr)^2 + (rd\theta)^2\right)\right]}{(dr)(rd\theta)w\sigma_0\rho_r} \end{cases} \quad . \tag{4-14}$$

where $\rho_r = \dfrac{\rho}{\rho_0}$ is the ratio of a line inductance with respect to the smallest line inductance and $Z_{ref} = \sqrt{\dfrac{h\rho_0}{\sigma_0}}$ is the characteristic impedance of the smallest line as defined in the previous section (27).

4.1.4. Scattering and traveling processes of the irregular TLM

For both Cartesian and cylindrical geometry, each TLM element is characterized by a circuit structure of five transmission lines (Figure 4-7) (1).

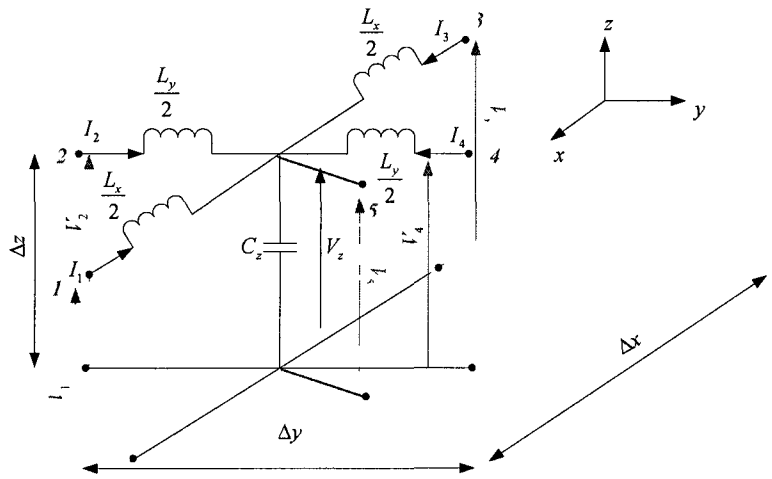

Figure 4-7 Shunt node for irregular Cartesian TLM

Each node is intersected by five lines where each line is characterized by two voltages (incident and reflected voltages) and its characteristic impedance (Figure 4-8).

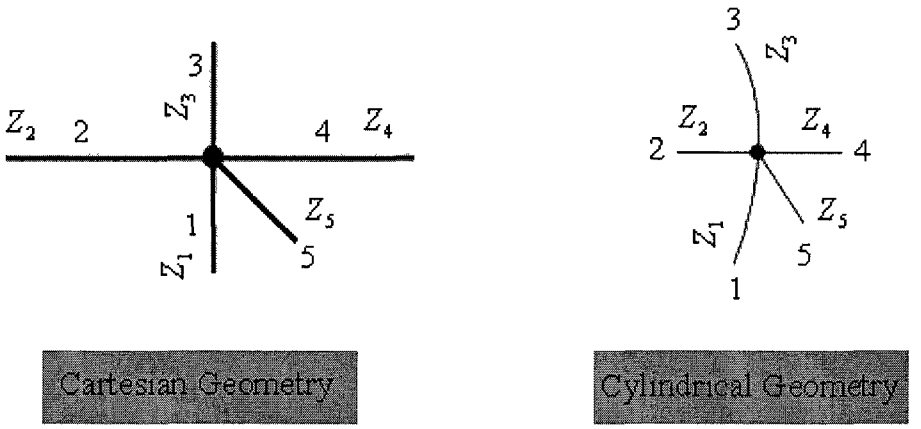

Figure 4-8 Lines intersecting an arbitrary node of irregularly spaced mesh

The equivalent Thevenin circuit will be composed of five Thevenin sources in series with five equivalent impedances corresponding to the five lines (Figure 4-9).

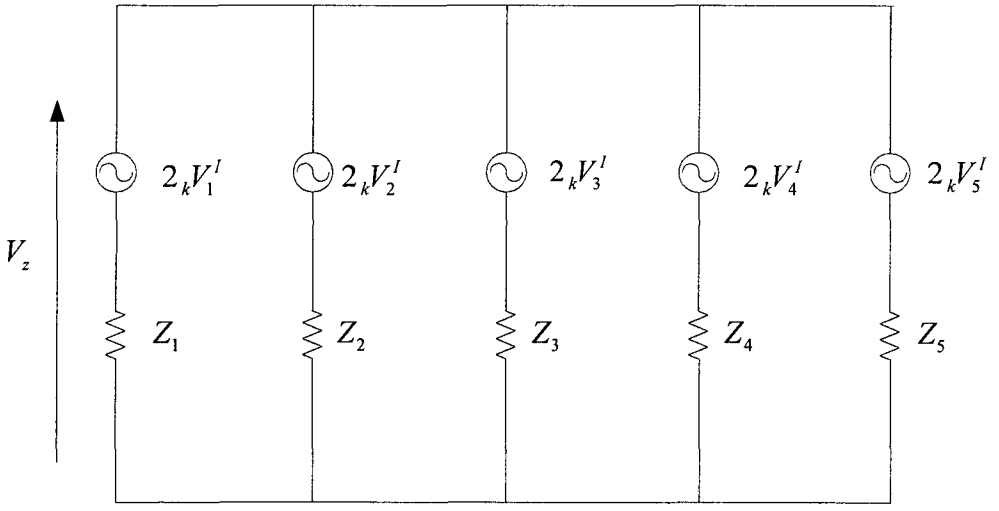

Figure 4-9 Thevenin equivalent circuit for the 5 lines intersecting an arbitrary node of the irregular mesh

The total voltage in the circuit presented in Figure 4-9 is

$$V_z = \frac{2\left(Z_1 {}_kV_1^I + Z_2 {}_kV_2^I + Z_3 {}_kV_3^I + Z_4 {}_kV_4^I\right) + 2 {}_kV_5^I Z_5}{Z_1 + Z_2 + Z_3 + Z_4 + Z_5}. \tag{4-15}$$

Using the same approach as in the previous chapter for the regular TLM the reflected voltages are obtained from

$$ {}_kV_i^R = V_z - {}_kV_i^I, i = 1,2,3,4,5. \tag{4-16}$$

From the circuit in Figure 4-9, equation (4-16) can be applied for the five voltages of each line of the TLM element,

$$\begin{aligned}
{}_kV_1^R &= \frac{2\left(Z_1 {}_kV_1^I + Z_2 {}_kV_2^I + Z_3 {}_kV_3^I + Z_4 {}_kV_4^I\right) + 2 {}_kV_5^I Z_5}{Z_1 + Z_2 + Z_3 + Z_4 + Z_5} - {}_kV_1^I \\
{}_kV_2^R &= \frac{2\left(Z_1 {}_kV_1^I + Z_2 {}_kV_2^I + Z_3 {}_kV_3^I + Z_4 {}_kV_4^I\right) + 2 {}_kV_5^I Z_5}{Z_1 + Z_2 + Z_3 + Z_4 + Z_5} - {}_kV_2^I \\
{}_kV_3^R &= \frac{2\left(Z_1 {}_kV_1^I + Z_2 {}_kV_2^I + Z_3 {}_kV_3^I + Z_4 {}_kV_4^I\right) + 2 {}_kV_5^I Z_5}{Z_1 + Z_2 + Z_3 + Z_4 + Z_5} - {}_kV_3^I \\
{}_kV_4^R &= \frac{2\left(Z_1 {}_kV_1^I + Z_2 {}_kV_2^I + Z_3 {}_kV_3^I + Z_4 {}_kV_4^I\right) + 2 {}_kV_5^I Z_5}{Z_1 + Z_2 + Z_3 + Z_4 + Z_5} - {}_kV_4^I \\
{}_kV_5^R &= \frac{2\left(Z_1 {}_kV_1^I + Z_2 {}_kV_2^I + Z_3 {}_kV_3^I + Z_4 {}_kV_4^I\right) + 2 {}_kV_5^I Z_5}{Z_1 + Z_2 + Z_3 + Z_4 + Z_5} - {}_kV_5^I
\end{aligned}. \tag{4-17}$$

The scattering matrix in this case

$$\begin{bmatrix} {}_kV_1^R \\ {}_kV_2^R \\ {}_kV_3^R \\ {}_kV_4^R \\ {}_kV_5^R \end{bmatrix} = \frac{1}{D} \begin{bmatrix} 2Z_1 - D & 2Z_2 & 2Z_3 & 2Z_4 & 2Z_5 \\ 2Z_1 & 2Z_2 - D & 2Z_3 & 2Z_4 & 2Z_5 \\ 2Z_1 & 2Z_2 & 2Z_3 - D & 2Z_4 & 2Z_5 \\ 2Z_1 & 2Z_2 & 2Z_3 & 2Z_4 - D & 2Z_5 \\ 2Z_1 & 2Z_2 & 2Z_3 & 2Z_4 & 2Z_5 - D \end{bmatrix} \begin{bmatrix} {}_kV_1^I \\ {}_kV_2^I \\ {}_kV_3^I \\ {}_kV_4^I \\ {}_kV_5^I \end{bmatrix}. \tag{4-18}$$

${}_kV_i^R$ and ${}_kV_i^I$ are the reflected and incident voltages to an arbitrary node of the line i at time k (Figure 4-10).

$D = \sum_{i=1}^{5} Z_i$ is the sum of the impedances of the four lines and the stub admittance.

The scattering matrix gives the relationship between the incident and reflected voltages at the same node.

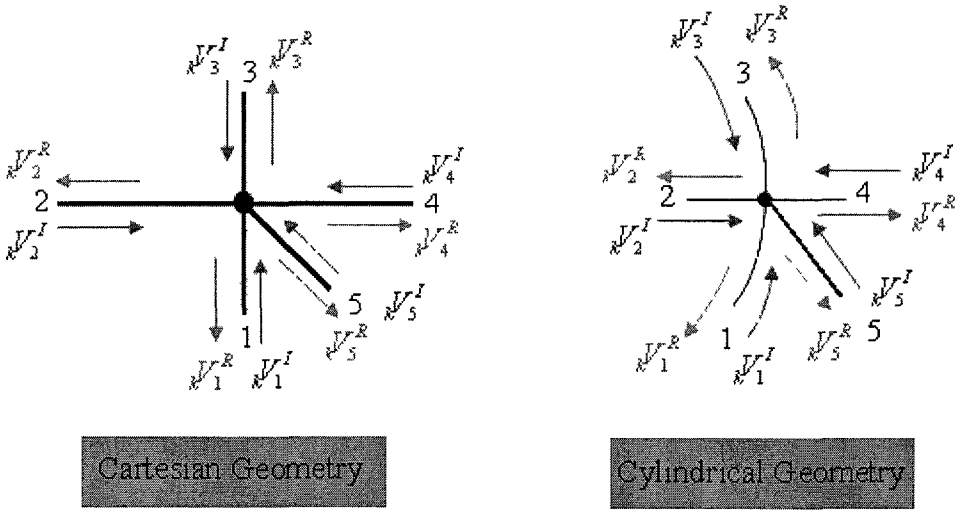

Figure 4-10 Scattering process of the voltages

Besides the scattering, there must be a traveling process of the voltages (or waves) between the nodes of a given mesh (Figure 4-11).

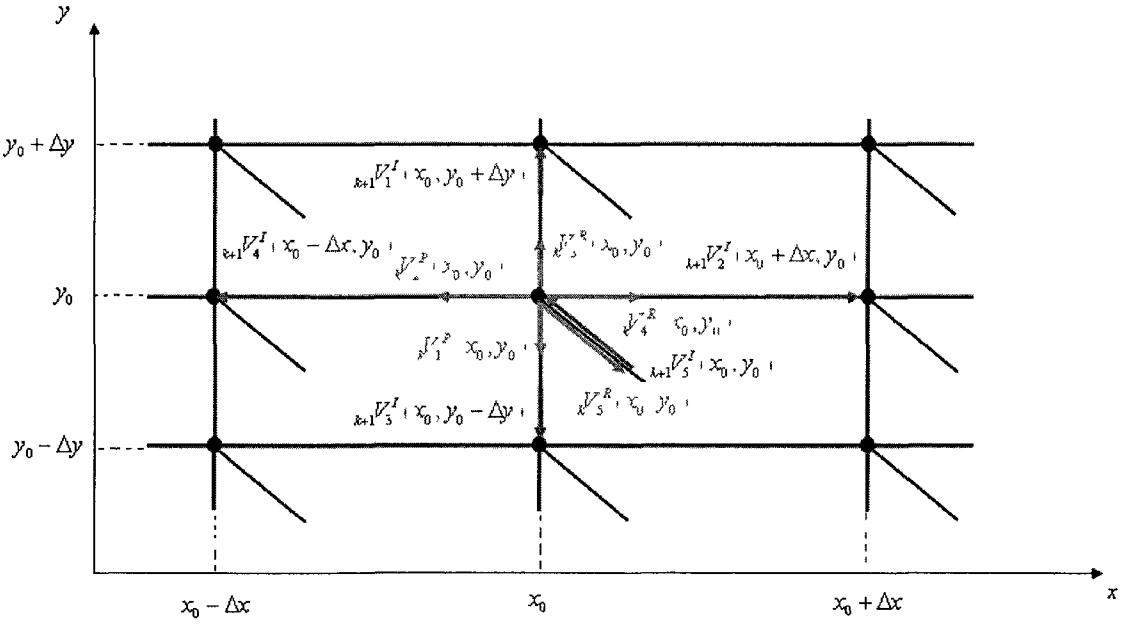

Figure 4-11 Traveling process in irregular Cartesian TLM mesh

In the Cartesian mesh the traveling process in described by the system of equations (4-19)

$$\begin{cases} {}_{k+1}V_1^I(x_0, y_0 + \Delta y) = {}_kV_3^R(x_0, y_0) \\ {}_{k+1}V_2^I(x_0 + \Delta x, y_0) = {}_kV_4^R(x_0, y_0) \\ {}_{k+1}V_3^I(x_0, y_0 - \Delta y) = {}_kV_1^R(x_0, y_0). \\ {}_{k+1}V_4^I(x_0 - \Delta x, y_0) = {}_kV_2^R(x_0, y_0) \\ {}_{k+1}V_5^I(x_0, y_0) = {}_kV_5^R(x_0, y_0) \end{cases} \tag{4-19}$$

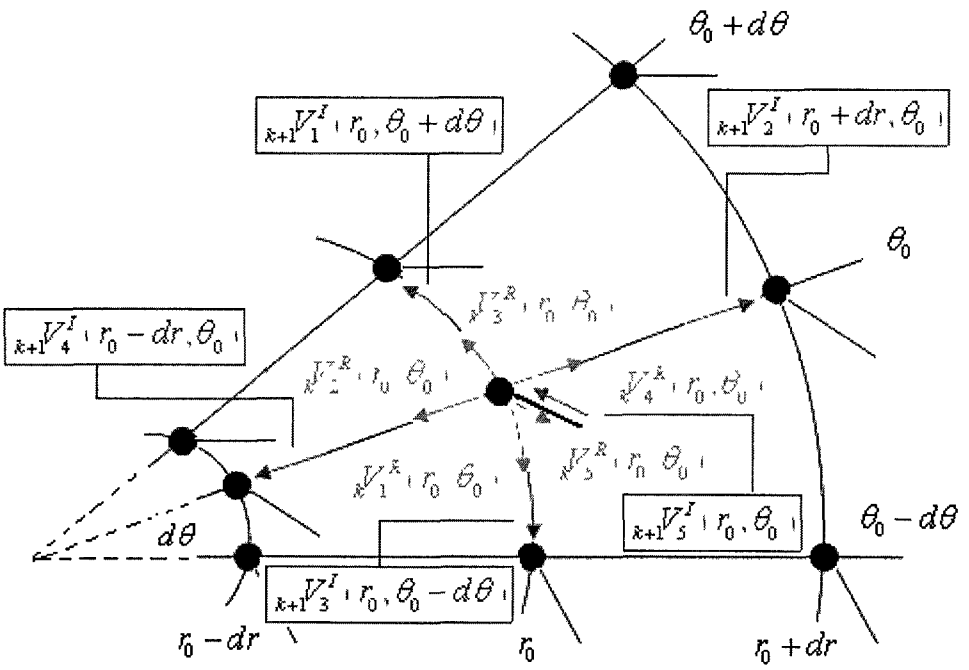

Figure 4-12 Traveling process in cylindrical TLM mesh

This traveling process ensures propagation of the waves over the entire medium. As seen in the regular TLM model, the reflected voltages from one node at time k will serve as incident voltages for the neighboring nodes at time $k+1$ with the exception of

the stub line where the reflected component at time k will serve as incident component to the same node at time $k+1$.

The traveling process in the cylindrical shape is described by the system of equations (4-20). The scattering matrix and the traveling process define the TLM propagation model of the wave in time and space. This model will be used in the next sections to simulate the ultrasound propagation across the artery.

$$\begin{cases} {}_{k+1}V_1^I(r_0,\theta_0+d\theta)={}_kV_3^R(r_0,\theta_0) \\ {}_{k+1}V_2^I(r_0+dr,\theta_0)={}_kV_4^R(r_0,\theta_0) \\ {}_{k+1}V_3^I(r_0,\theta_0-d\theta)={}_kV_1^R(r_0,\theta_0). \\ {}_{k+1}V_4^I(r_0-dr,\theta_0)={}_kV_2^R(r_0,\theta_0) \\ {}_{k+1}V_5^I(r_0,\theta_0)={}_kV_5^R(r_0,\theta_0) \end{cases} \tag{4-20}$$

4.2. Irregular TLM validation

The irregular TLM model will be compared to the conventional TLM models that exist in the literature. Some common case studies will be developed and the results will be compared in order to validate the irregular TLM. Two case studies will be developed where both Cartesian and cylindrical irregular TLM models will be adapted to the regular TLM model in order to compare the wave propagation in a rectangular medium.

4.2.1. Sine Wave propagation

A 100 by 100 nodes squared mesh is considered to be the medium where the wave will be propagating. A sine wave source of 100 time samples duration is injected to the center node of the medium (node (50,50)). Then the wave amplitudes are recorded as functions of time in all node locations (Figure 4-13).

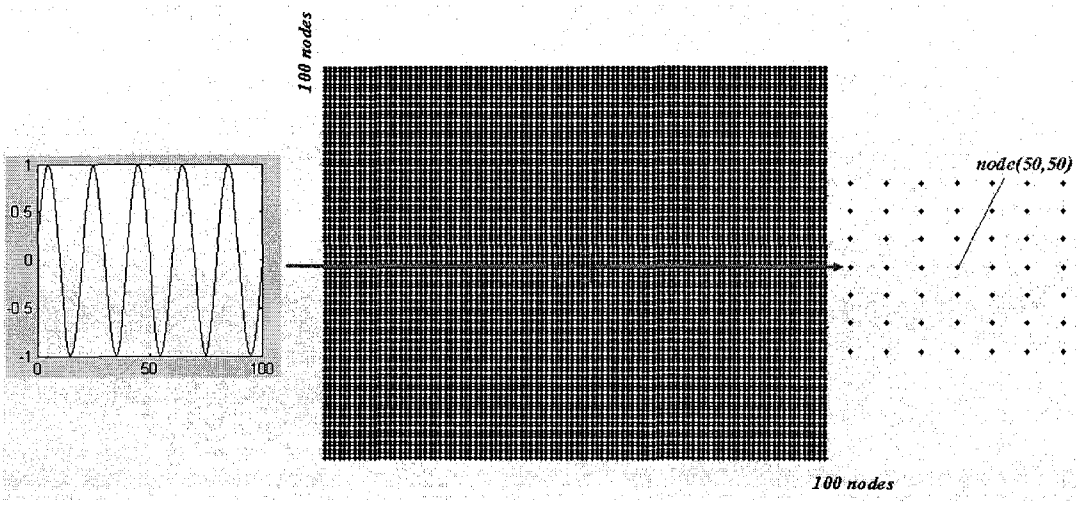

Figure 4-13 Generated regular model by conventional regular TLM

The gridding rates for the above mentioned model are equal in both directions.

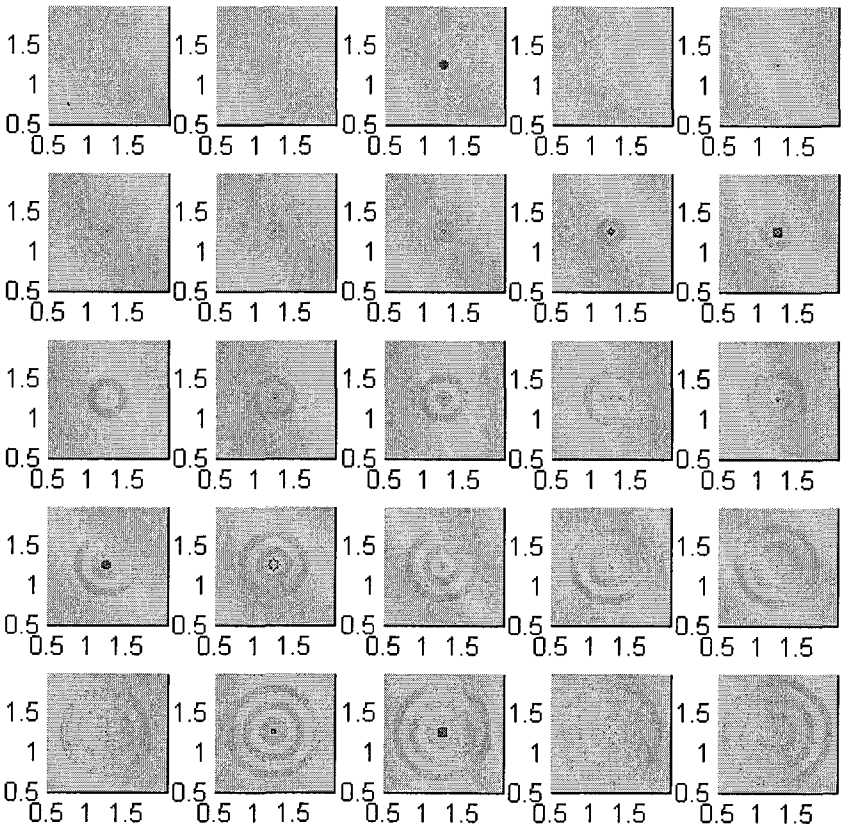

Figure 4-14 Sine wave propagation from the center of the medium (picture taken every three sample times)

The propagation occurs in a circular fashion as expected A rectangular medium is then constructed using the irregular Cartesian TLM model. The gridding rates Δx and Δy are such that $\Delta y > \Delta x$. This medium is composed of 100 by 100 nodes. The same sine wave of the regular TLM model is injected in the center of the medium (node(50,50)). The propagation of the wave in space and time is illustrated in Figure 4-15. The propagation is elliptic due to the difference in the gridding rate in both directions. If the gridding rate in y direction is reduced till $\Delta y = \Delta x$ then the sine wave propagation regains its circular shape exactly as for the regular TLM model (Figure 4-16)

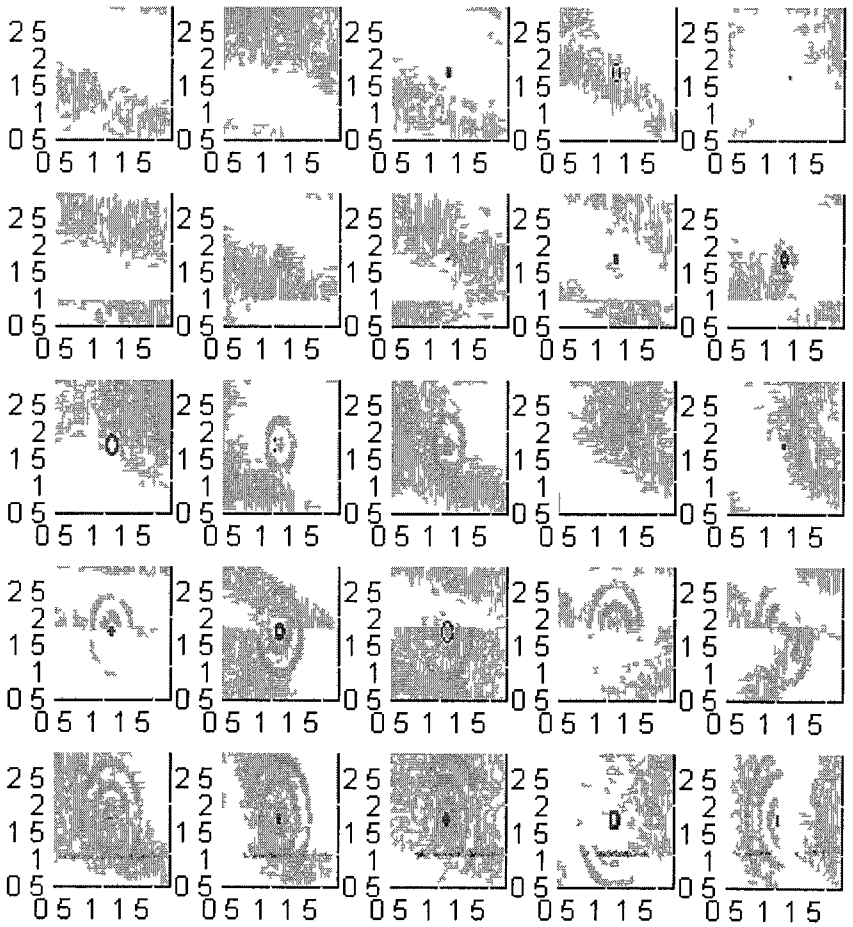

Figure 4-15 Sine wave propagation in the irregular mesh (picture taken every three time samples)

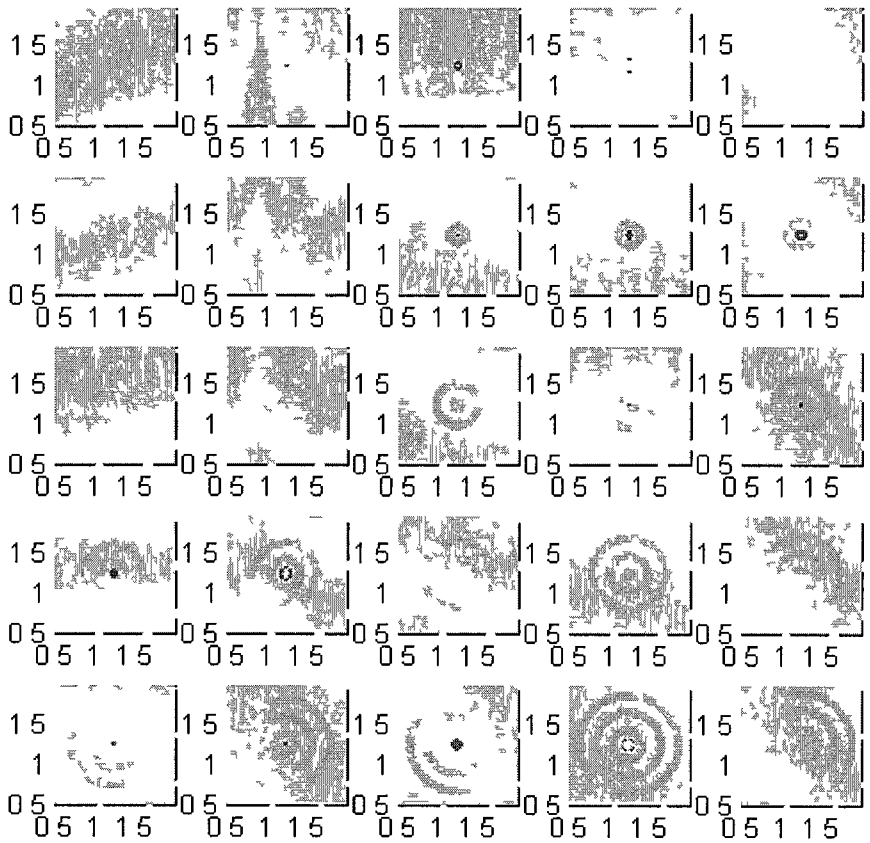

Figure 4-16 Propagation of the sine wave using the irregular Cartesian TLM model (picture taken every three time samples)

A rectangular medium can be generated also by the cylindrical irregular TLM model. By setting the radii to be much greater than the angular interval of the cylindrical shape of the medium, $R >> \theta$, a rectangular medium is created (Figure 4-17).

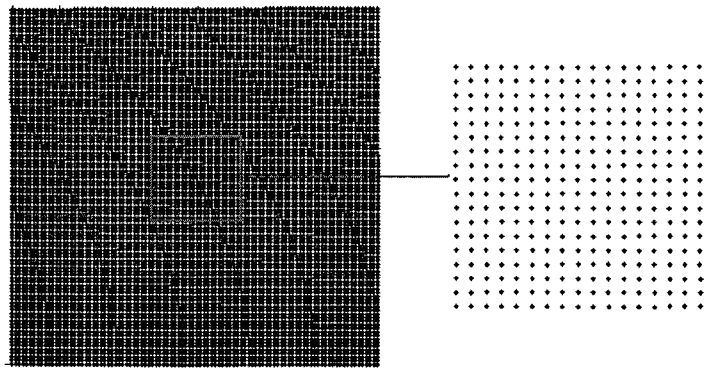

Figure 4-17 A 100 by 100 nodes rectangular medium created by irregular cylindrical TLM

The same sine wave is injected in the same location (center node) and the wave propagation is captured.

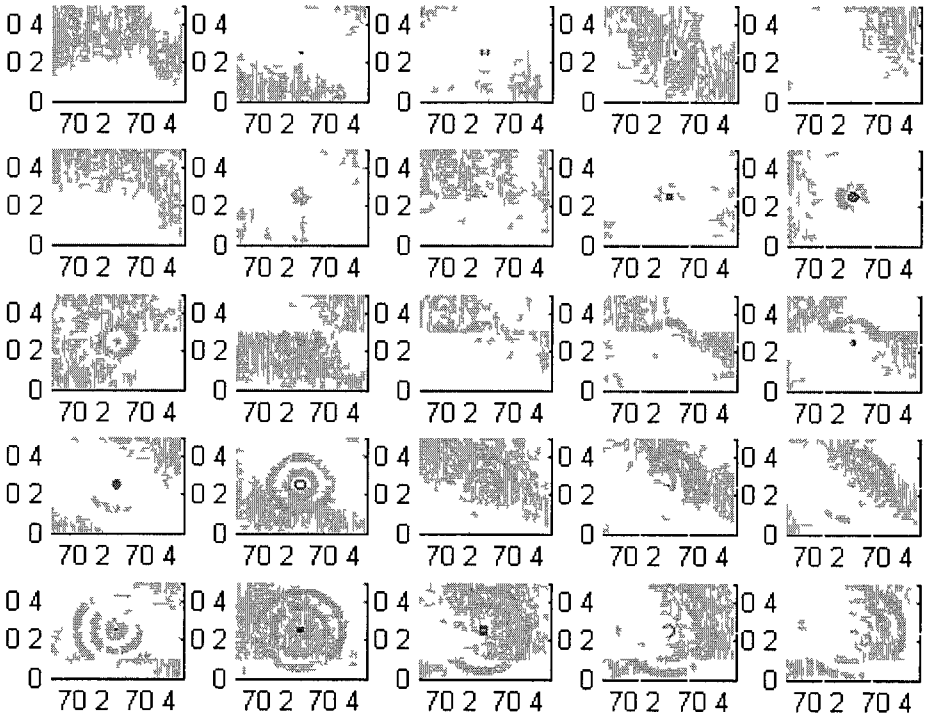

Figure 4-18 Simulated sine wave propagation in the irregular cylindrical TLM model (picture taken every three time samples)

From Figure 4-14,Figure 4-16 and Figure 4-18, it has been shown that regular and irregular TLM models gave the same propagation in space and time of the sine wave. The irregular TLM (Cartesian and cylindrical) models are then validated against the regular TLM method.

4.2.2. Ultrasound Wave Behavior against an obstacle

In this case the same medium composed of 200 by 100 nodes will be studied for all the models. An inclusion will be inserted in the medium. This obstacle is totally reflective and located between the 40th and 60th node in the x direction and 70th and 130th node in the y direction. The source wave will be injected in the vertical left edge of the medium from the 3rd node to the 198th node (black line in Figure 4-19) This source wave is a one period sinusoid that lasts 10 sample times.

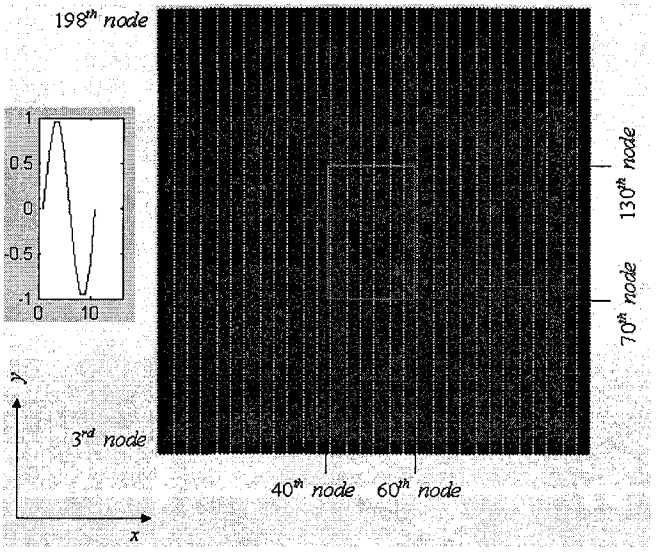

Figure 4-19 Medium composed of 200 by 100 nodes

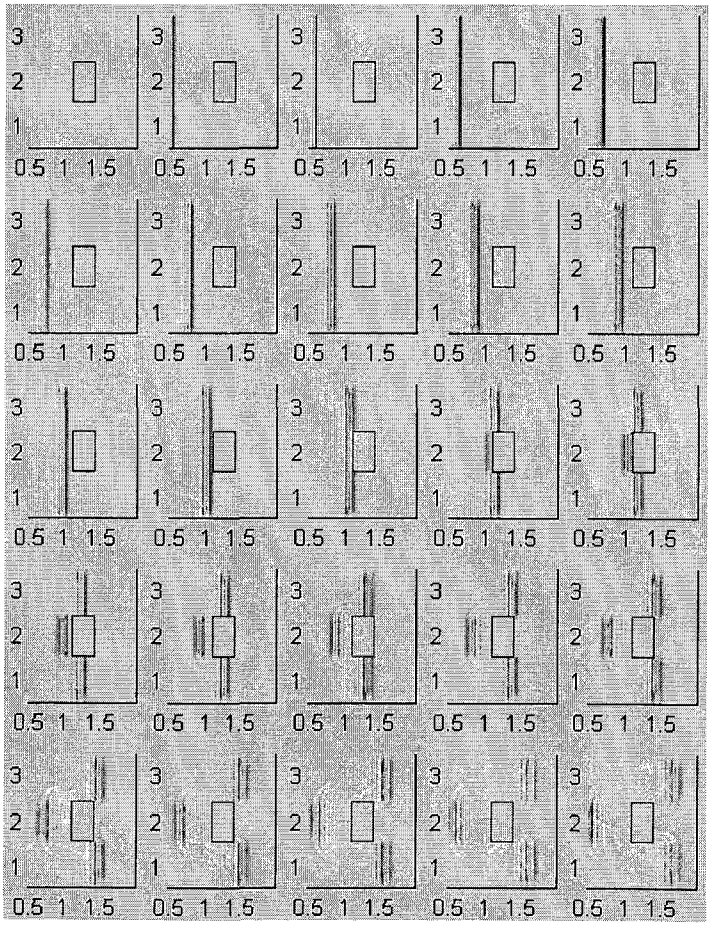

Figure 4-20 Wave propagation and behavior of the sound wave against a totally reflective obstacle.

The propagation of the wave is recorded in time and space Each picture is taken every 5 time samples The same medium is created using Cartesian and cylindrical irregular TLM The propagation of the same wave is captured in space and time It is shown from Figure 4-20 and Figure 4-21 that the propagation of the wave has the same fashion The Cartesian irregular TLM medium was constructed using the same gridding sample rates in both directions. Despites the difference in the scattering matrices for regular and irregular Cartesian models, the propagation is the same In fact the wave has shown similar behavior in both cases. This result ensures that the irregular Cartesian TLM model is valid for sound wave propagation modeling.

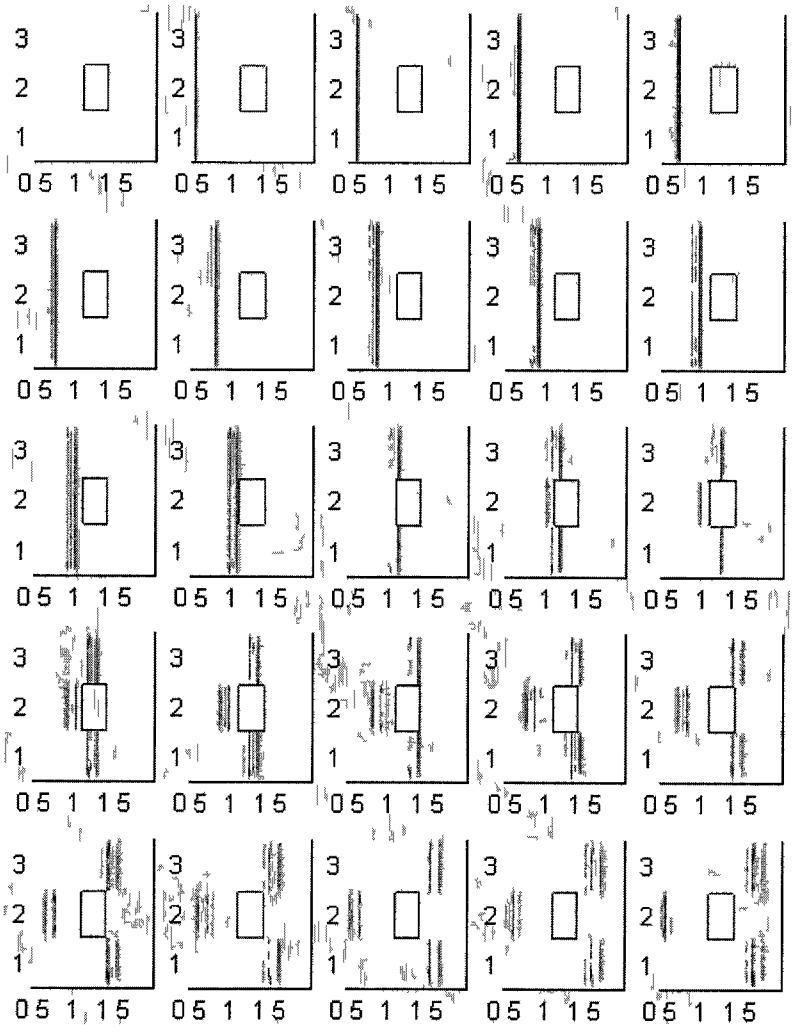

Figure 4-21 Ultrasound wave propagation and behavior against a totally reflective obstacle using irregular Cartesian TLM (pictures are taken every five time samples)

The medium in Figure 4-22 was constructed using the cylindrical irregular TLM model The inner and outer radii where set to be equal to 70 1 and 70 496 whereas the angular interval was set to be equal [-2*pi/890,2*pi/890] It can be seen clearly that the radii range is much bigger than the angular interval. Thus the circular shape of the medium converges to a rectangular geometry (Figure 4-23).

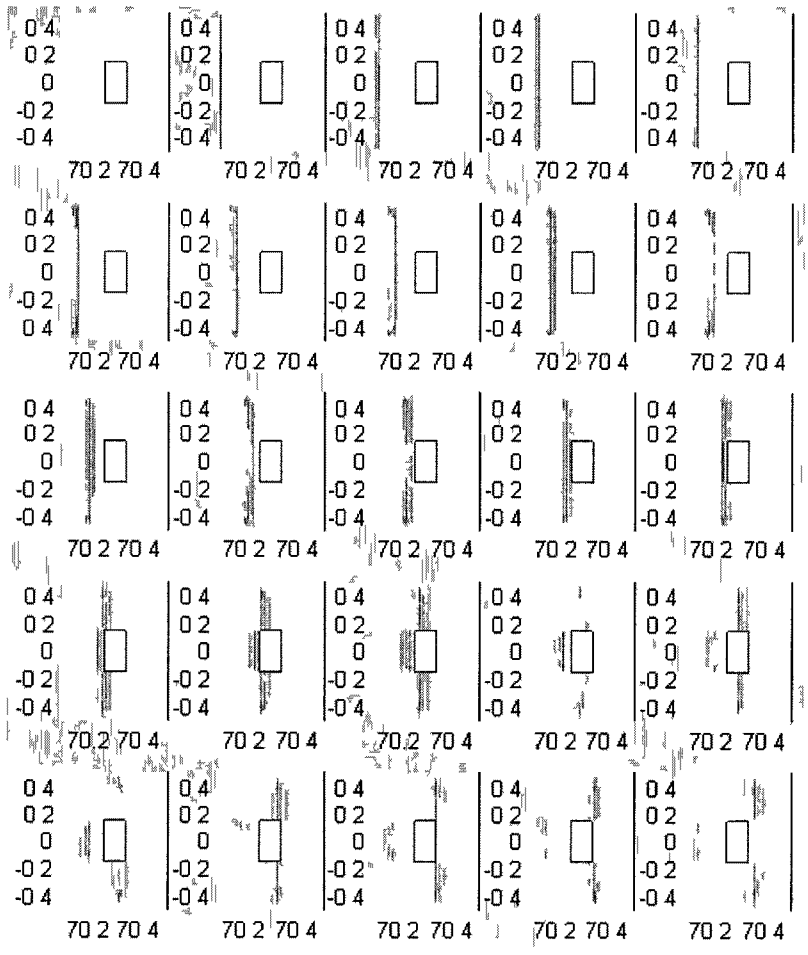

Figure 4-22 Ultrasound wave propagation and behavior against a totally reflective obstacle using irregular cylindrical TLM (pictures are taken every five time samples)

It can be seen from Figure 4-22 that the propagation of the wave is similar to the ones captured by the regular and Cartesian irregular TLM models Thus the cylindrical TLM model can be used to model the sound propagation in a circular medium to simulate the ultrasound wave behavior in an artery cross-section

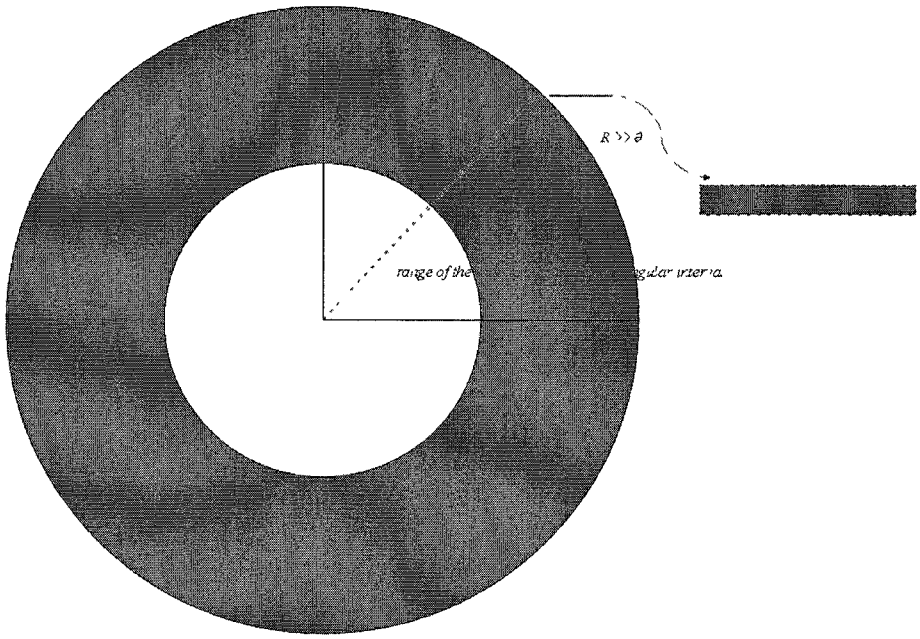

Figure 4-23 Rectangular medium construction using cylindrical TLM model

The following section will be dedicated to build a model for IVUS using the cylindrical TLM model.

4.3. IVUS TLM model

In this section an IVUS model will be constructed using TLM method. The code is developed in Matlab. Since the studied space is an artery cross-section which is circular, the distances between the nodes of the generated mesh are not equal. Thus the mesh is irregular and circular. Thus the cylindrical irregular TLM method will be used for the IVUS modeling. This model departs from a circular medium to a circular mesh of nodes. Each node in this medium is characterized by a radial distance r and an angular position θ. Given the position of each node, the impedances of the radial and angular line are calculated according to the relationships established in the "Cylindrical Irregular TLM" section. Hence the scattering matrix, which is function of these impedances, is derived. Finally, the amplitudes in the lines are calculated each time step. These values will capture the sound wave propagation in the medium. As the ultimate goal is to use this numerical model to collect the temporal and spatial data, (amplitude of the wave in each node at a given time) the model should emulate the physics of the sound wave propagation theory. Since the sound impulse is emitted from the transducer in a way such

that it reaches all the artery cross-section depth, the developed model should present the same way of propagation by reaching the outer radius of the modeled medium. By insuring that the wave reaches all the radial length, the behavior of the modeled wave can capture the geometry and the acoustic properties of all the components to be identified in the artery. The model developed hereafter will take into account all these physics-based aspects.

4.3.1. Auto-generated mesh grid for the IVUS TLM model

The TLM model departs from the inner and outer radii. A mesh grid based on the specified gridding rates in the radial and angular directions is then created. The choice of the gridding rate is essential for capturing the propagation of the ultrasound wave. The wave should reach the outer edge of the artery cross-section. In fact for an arbitrary mesh the propagation trend of the ultrasound wave is more pronounced in the angular direction of the circular medium. The choice of the mesh grid must be generated in a way that guarantees a conic wave propagation of the TLM method. This means that the propagation should occur in a conic way in the radial direction. The propagation as developed previously in the TLM model depends on the scattering matrix which is function of the lines impedances. These impedances are function of the gridding rates in both radial and angular directions. Thus a specific mesh grid should be developed to ensure this numerical stability. The propagation of the sound wave is expected to be like the one illustrated by Figure 4-24.

To investigate the effect of the grid on the impedances the ratio of the angular and radial impedances is examined. An arbitrary mesh is constructed and the TLM model is generated in order to capture the sound wave propagation through the circular medium. A pulse is injected in one node of the inner radius of the medium then the propagation recorded in space and time.

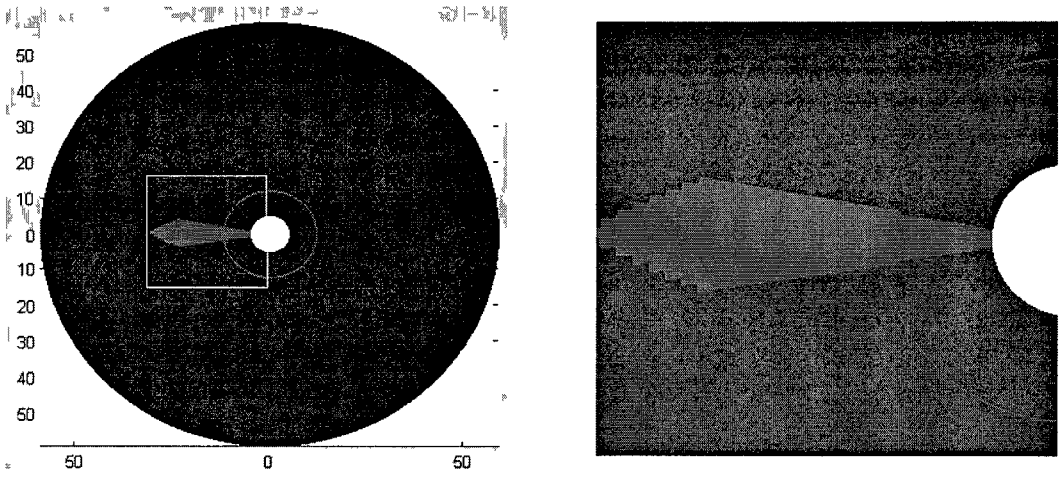

Figure 4-24 Conic propagation of the sent wave through the circular medium

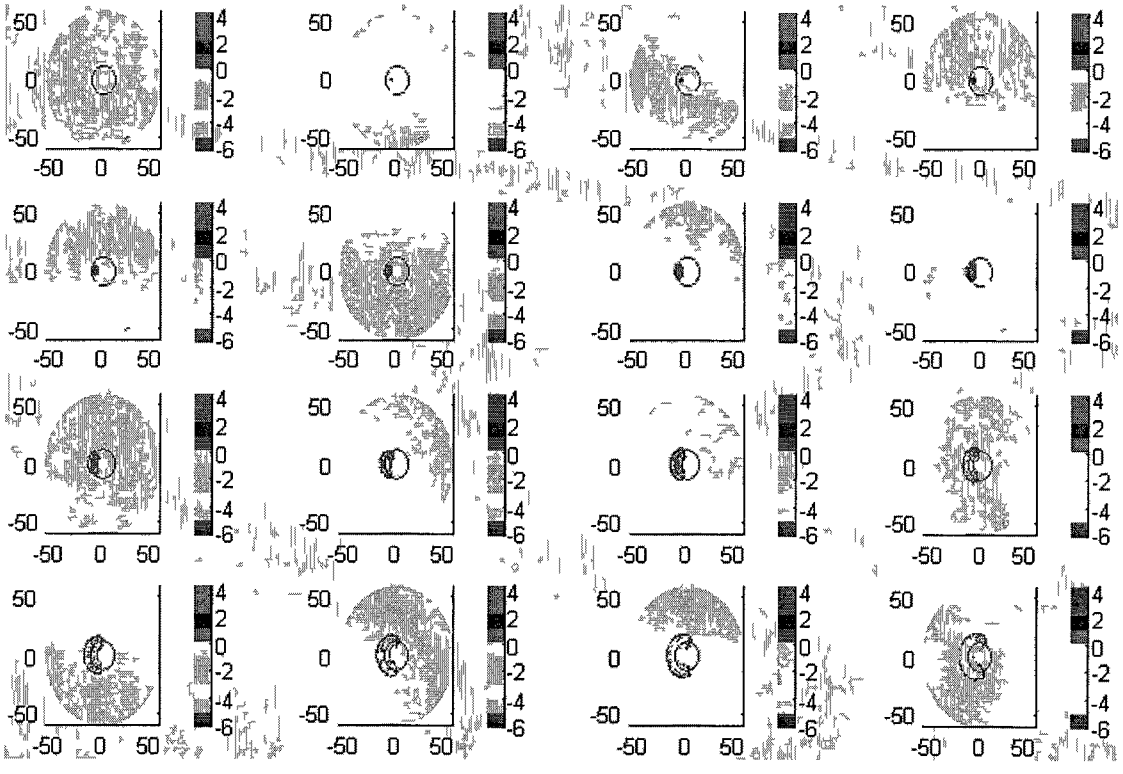

Figure 4-25 Angular direction of the propagation of the wave

It can be seen from Figure 4-25 that after a certain radial position the wave propagation deviates to the angular direction. This propagation fashion is related to the length of the lines in radial and angular direction. In fact the angular lines become bigger compared to the radial lines as the wave moves toward the outer radius (Figure 4-26).

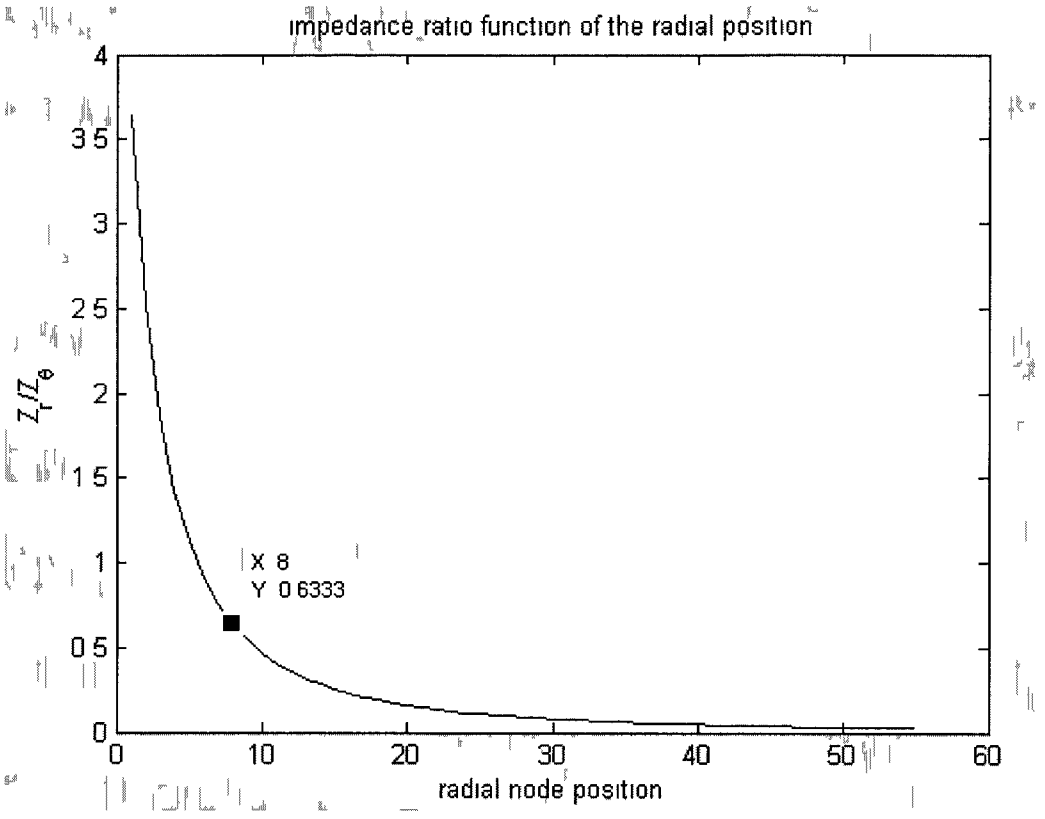

Figure 4-26 Impedance ratio function of the radial position

The angular deviation of the propagation occurs when the wave hit the red circular position in Figure 4-25. This position is characterized by $\frac{Z_r}{Z_\theta} = 0.633$. Since $\frac{Z_r}{Z_\theta} = \frac{(dr)^2}{(Rd\theta)^2}$, after this radial position, the ratio between the gridding rates has this condition $\frac{dr}{Rd\theta} < 0.8$. The mesh grid is designed such that $\frac{dr}{Rd\theta} \geq 0.8$. By imposing this numerical condition on the mesh grid, the propagation occurs in a conic fashion as illustrated in

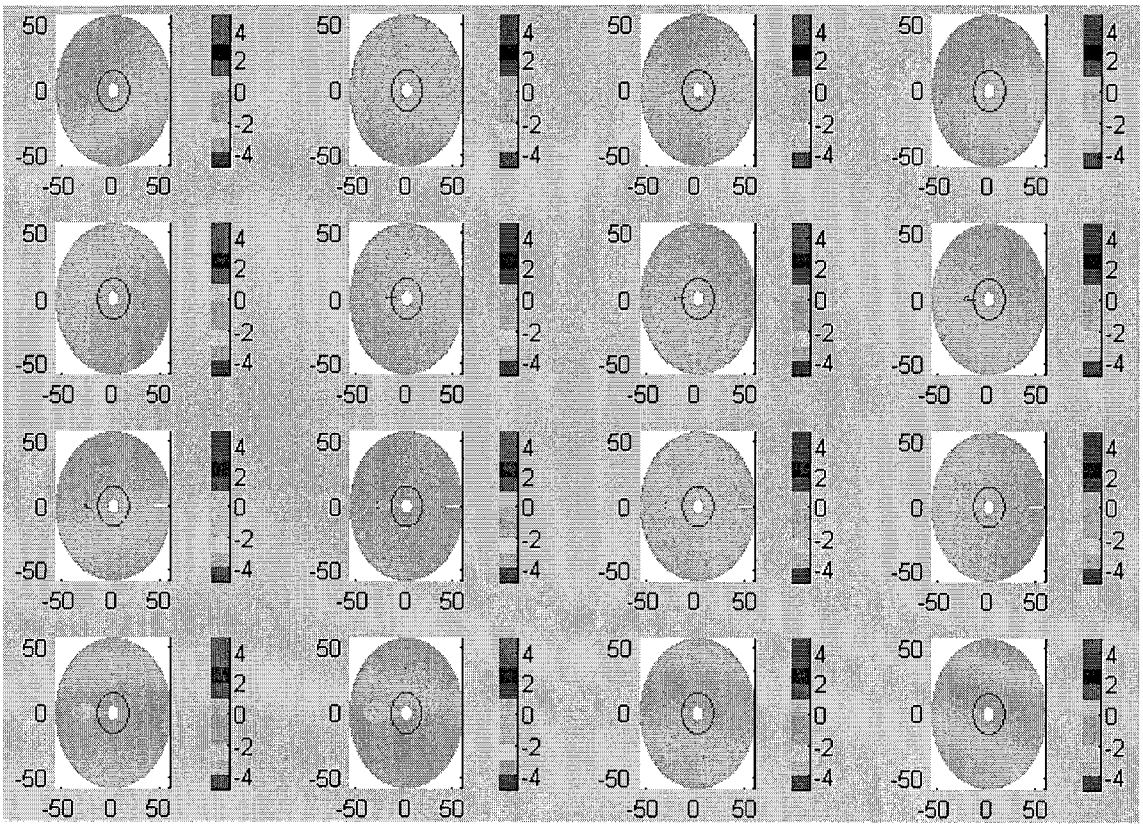

Figure 4-27 Propagation of the wave in radial direction with a conic shape

It can be shown that the numerical condition that was imposed on the irregular cylindrical TLM model ensures an appropriate propagation of the sound wave in the circular medium. From now on this numerical condition on the geometry will be taken into account for all the simulations.

4.3.2. IVUS TLM model for a healthy artery

Since IVUS is an imaging method based on the ultrasound wave for the artery cross-sections, the cylindrical irregular TLM model will be employed to mimic the ultrasound wave propagation in the circular medium. The cylindrical TLM model has been established in section "Cylindrical Irregular TLM". Since this is a numerical method that has been implemented in Matlab a finite number of nodes must be defined. Therefore a boundary termination of the medium is established in the developed Matlab code.

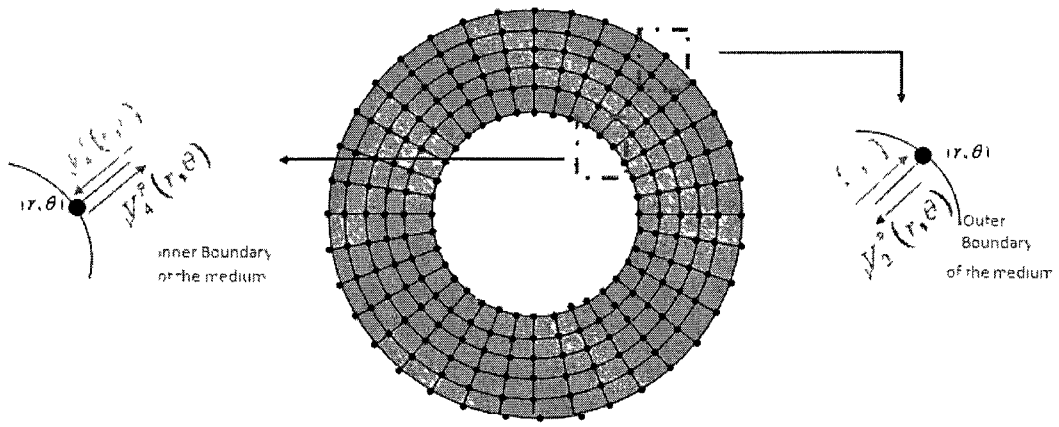

Figure 4-28 Boundary termination of the modeled artery cross-section

From Figure 4-28, the voltages of the nodes that are on the outer boundary are characterized by

$$ {}_kV_2^R(r,\theta) = \frac{Z_{outer_medium} - Z_2(r,\theta)}{Z_{outer_medium} + Z_2(r,\theta)} {}_kV_2^I(r,\theta). \tag{4-21} $$

And the voltages of the nodes on the inner boundary are characterized by

$$ {}_kV_4^R(r,\theta) = \frac{Z_{inner_medium} - Z_4(r,\theta)}{Z_{inner_medium} + Z_4(r,\theta)} {}_kV_4^I(r,\theta), \tag{4-22} $$

where Z_{inner_medium} and Z_{outer_medium} are the acoustic impedances of the media that are surrounding the artery cross-section from inside and outside respectively. Generally the outer and inner impedances are always equal to the ones of the surrounding medium itself. But for all the developed simulations the surrounding media impedances will be taken in such a way the boundary reflection effect is attenuated so that these reflected components do not influence the wave propagation inside the artery cross-section

The model in Matlab gives the possibility of using the Simulink toolbox to design a variety of wave signals to be considered as source signals in the simulation part (Same generated signals as for the developed regular TLM model in the previous chapter). These signals could be implemented anywhere in the medium.

For the healthy artery model, the same sinusoidal source in the previous chapter is designed and injected in one of the nodes from the inner radius specifically in the 199th angular and 1st radial position.

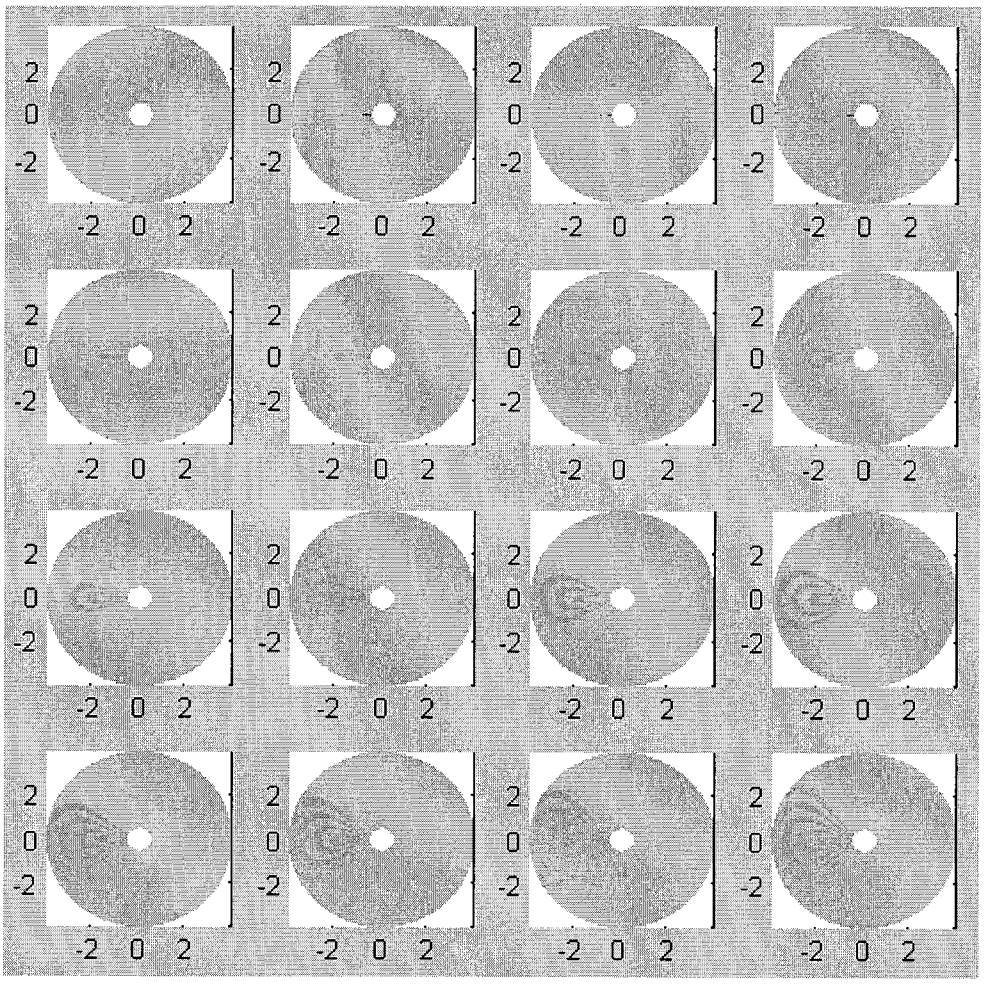

Figure 4-29 Snapshots of the spatial distribution of the wave amplitudes on the artery cross-section (pictures taken every 8 time samples)

The cylindrical TLM model offers the possibility of taking snapshots of the amplitude distribution along the entire medium surface. This distribution contributes to a visual inspection of the wave behavior in the medium. In fact a colorful snapshot is given for the artery. This picture is always the only mean for the medical doctors to diagnose the anomalies that could form inside these arteries.

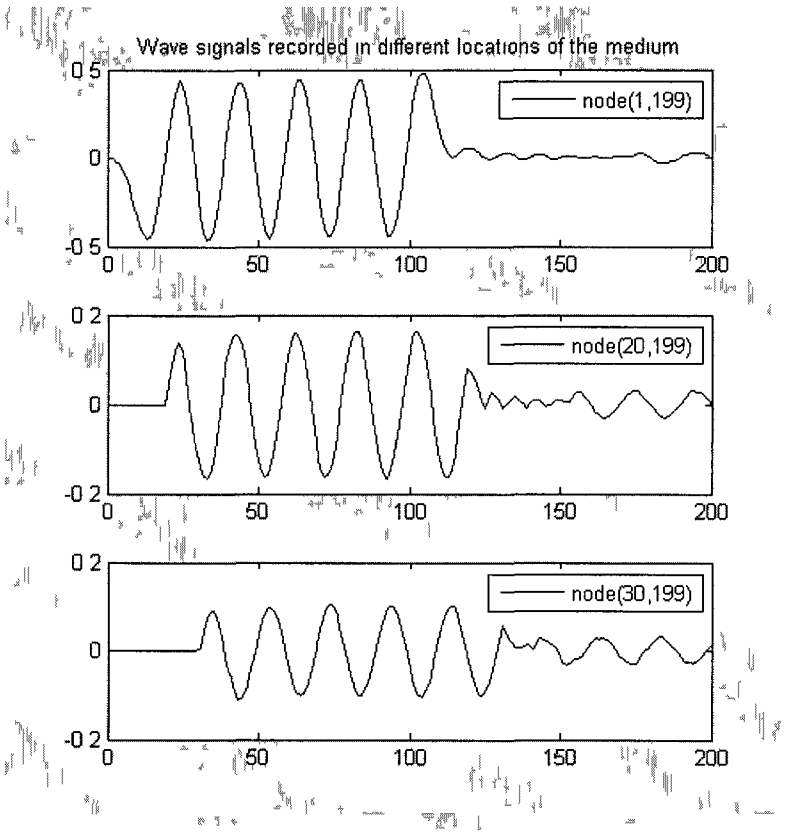

Figure 4-30 Time signals record of the wave propagation at different locations

This model offers also the possibility of recording the wave signals in time at all the nodes locations. This type of data gives the possibility of developing a more analytical and precise study of the wave behavior inside the artery.

4.3.3. IVUS TLM model for abnormal artery

Unhealthy artery cross-sections contain inclusions and anomalies. The purpose of this section is to show the ability of the cylindrical TLM method in modeling such abnormalities inside the artery. An obstacle will be embedded inside the mesh grid of the circular medium. Size and location of this obstacle or inclusion are made flexible to give the possibility of manipulating these parameters. In addition to the geometric properties, the acoustic properties can also be changed accordingly.

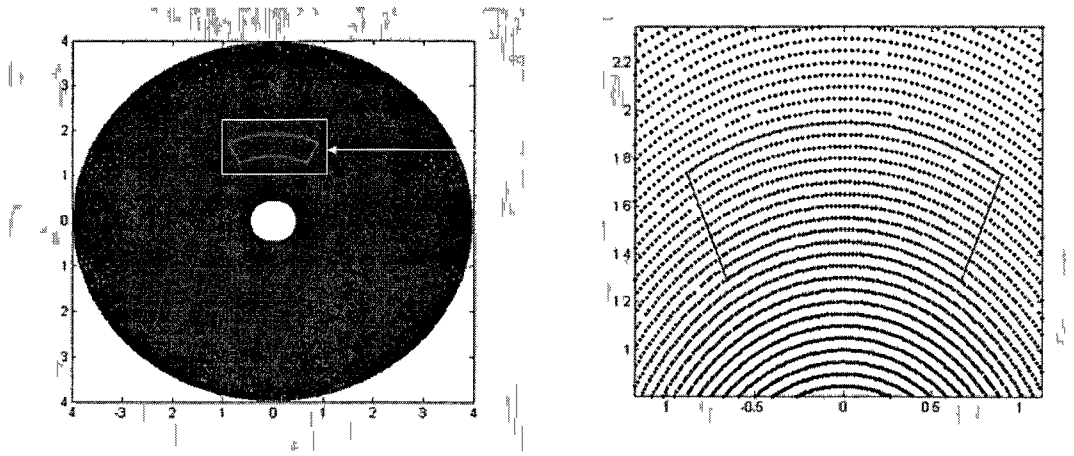

Figure 4-31 Inclusion inserted in the circular medium between the 70th and 130th angular nodes and 20th and 30th radial nodes

The inclusion is characterized by four edges where the transmission/reflection law is applied

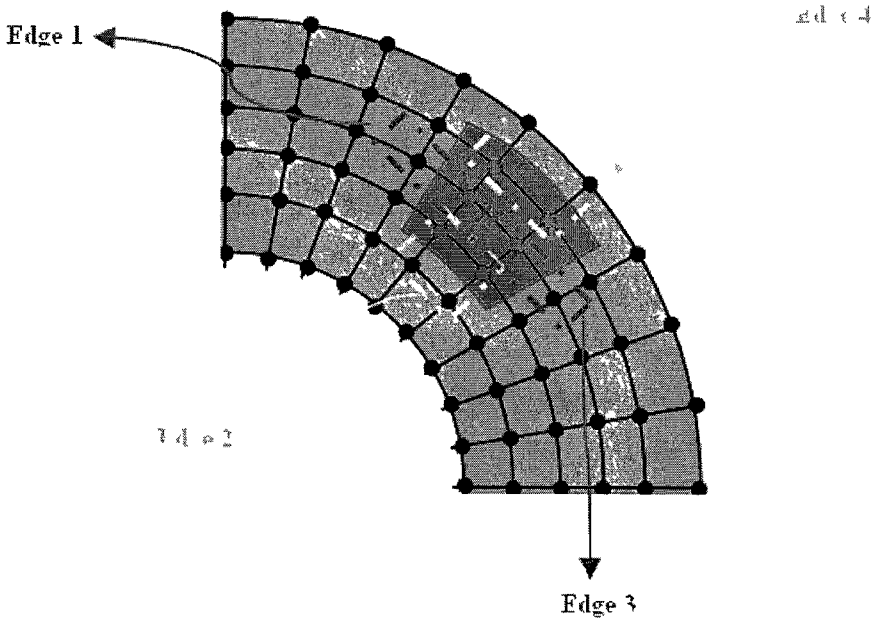

Figure 4-32 Common edges between the healthy artery (blue region) and the inclusion (red region)

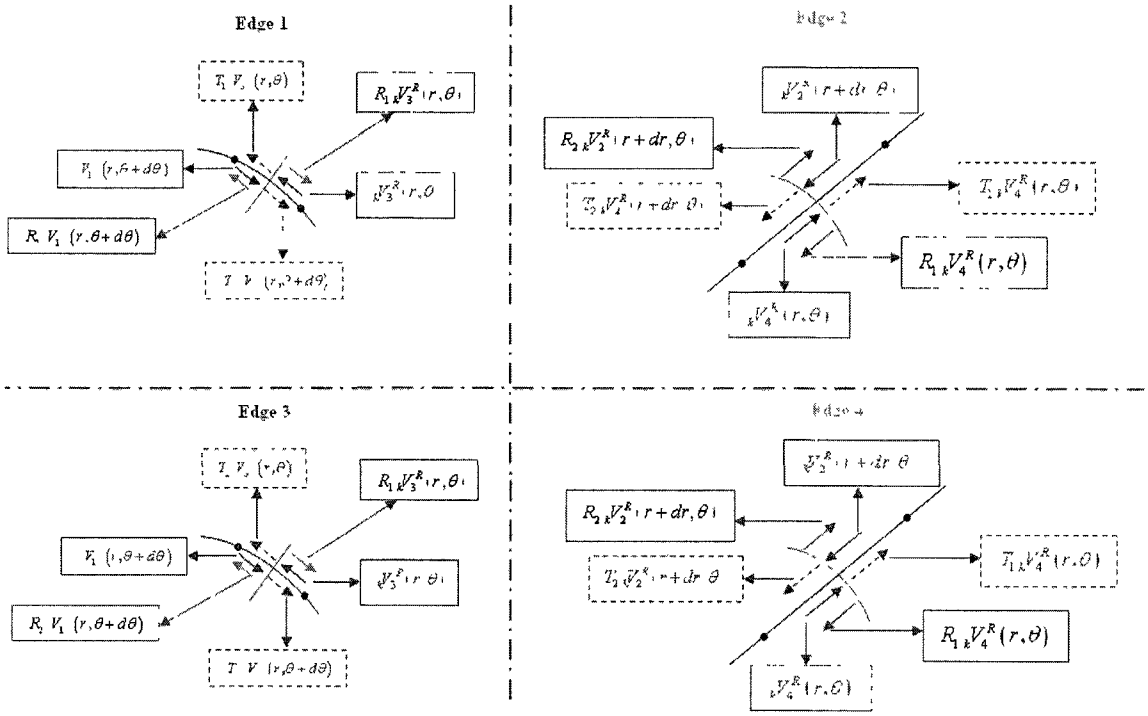

Figure 4-33 Reflection/transmission of the wave components between the inclusion and the artery

Edge 1 and Edge 3:

$$\begin{cases} {}_{k+1}V_3^I(r,\theta) = R_{1\,k}V_3^R(r,\theta) + T_{2\,k}V_1^R(r,\theta+d\theta) \\ {}_{k+1}V_1^I(r,\theta+d\theta) = R_{2\,k}V_1^R(r,\theta+d\theta) + T_{1\,k}V_3^R(r,\theta) \end{cases},$$

where $R_1 = \dfrac{Z_1(r,\theta+d\theta) - Z_3(r,\theta)}{Z_1(r,\theta+d\theta) + Z_3(r,\theta)}, T_1 = 1 - R_1$ and $R_2 = \dfrac{Z_3(r,\theta) - Z_1(r,\theta+d\theta)}{Z_3(r,\theta) + Z_1(r,\theta+d\theta)}, T_2 = 1 - R_2$

.

Edge 2 and Edge 4:

$$\begin{cases} {}_{k+1}V_4^I(r,\theta) = R_{1\,k}V_4^R(r,\theta) + T_{2\,k}V_2^R(r+dr,\theta) \\ {}_{k+1}V_2^I(r+dr,\theta) = R_{2\,k}V_2^R(r+dr,\theta) + T_{1\,k}V_4^R(r,\theta) \end{cases},$$

where $R_1 = \dfrac{Z_2(r+dr,\theta) - Z_4(r,\theta)}{Z_2(r+dr,\theta) + Z_4(r,\theta)}, T_1 = 1 - R_1$ and $R_2 = \dfrac{Z_4(r,\theta) - Z_2(r+dr,\theta)}{Z_4(r,\theta) + Z_2(r+dr,\theta)}, T_2 = 1 - R_2$

.

The same sine wave of the healthy case is injected from the inner radius (node (1st radial direction, 100th angular direction)) and the wave propagation is recorded.

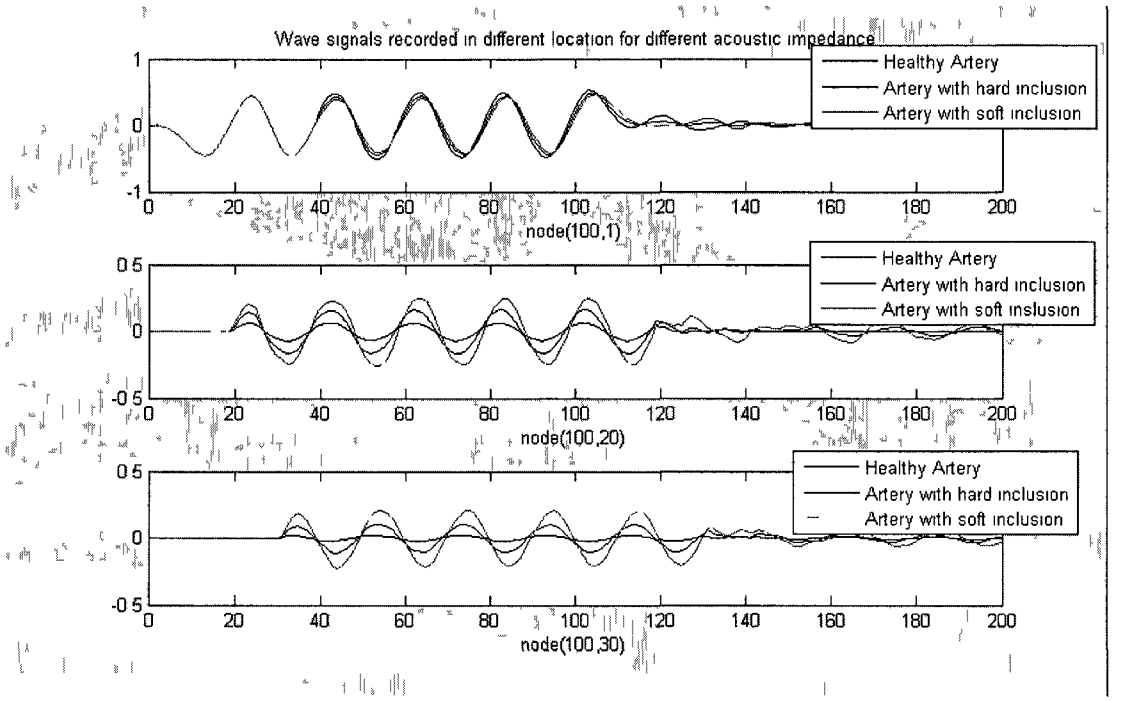

Figure 4-34 Time signals record of the wave propagation at different locations having different inclusion

$$(Z_{Hardinclsu\,ion} = 7.4Z_{\text{healthy artery}} \text{ and } Z_{Softinclsu\,ion} = 0.074Z_{\text{healthy artery}})$$

It can be shown from Figure 4-34, the effect of the acoustic properties of the inclusions that form inside the artery. This model will be employed in the next chapter to analyze these recorded signals and build a lumped parameter model of the different tissues types based on their size and acoustic properties

4.4. Summary

In this chapter, a new approach using TLM method was developed in order to solve for the ultrasound wave propagation in irregularly shaped media. This method departed from taking into account the difference in gridding rates in different direction and has built a new scattering process of the wave in order to circumvent the irregularities in the geometry. A new scattering process of the wave has been established that is dependent on the geometry of the lines linking the nodes of the medium mesh grid. This scattering process is also function of the acoustic properties of the studied medium.

Both irregular Cartesian and cylindrical irregular TLM models were developed. These models were validated against regular TLM models that exist in the literature.

Since IVUS images artery cross-sections which has a circular medium, cylindrical irregular TLM model was adopted in order to mimic the ultrasound wave propagation inside the medium. This model has shown its flexibility to design multiple source waves that could be injected in any location of the medium. The propagating signals could be recorded function of time and space. In addition to the healthy artery that was modeled, it has been shown that inclusion could be introduced anywhere in the medium with different geometric and acoustic properties.

This model will be used in the next chapter to characterize different inclusions using the recorded time signals.

Chapter 5 Tissue characterization using digital signal processing techniques

The ultimate goal of this study is to define a procedure by which arterial tissue characterization (healthy tissue and inclusions or plaques) can be realized. In the past, elaborate and meticulous approaches have been proposed that could differentiate ***quantitatively*** between the various tissue types and specifically between the different plaque burdens. This chapter departs from the traditional approaches appearing in the literature by considering the inclusion within a medium to be a dynamic system. A system identification approach will be adopted to characterize the dynamics of the plaque. Thus, the TLM models developed in chapters 3 and 4 will be used as a mean of acquiring the time signals transmitted and reflected in a region of interest within the medium (plaque or inclusion location). These signals will be considered as inputs and outputs to the dynamic system where digital signal processing techniques are employed to identify a parametric model for these plaques. To apply parametric system identification, the design of the wave source (i.e., the signal to be transmitted from the IVUS) should be identified. The traditional notion of the persistency of excitation condition will be exploited so that the dynamics of the plaques are captured. In this chapter an introduction on the system identification approach will be given. The conventional regular and cylindrical irregular TLM models will be then adopted to generate different parametric models of the plaques. To conclude this chapter, parametric models will be constructed for soft and hard plaques using both regular and cylindrical irregular TLM models.

5.1. Introduction to system identification technique for an artery tissue

Presented is a brief introduction to system identification. The approach adopted for this work will then be detailed. Finally the steps of the identification process will be presented.

5.1.1. System identification overview

System identification techniques have been widely used. These techniques usually lead to the modeling of a dynamic system using experimental measurements. In fact this dynamic system is excited by a rigorously selected input signal. Then the output and input are observed and recorded for processing (Figure 5-1). Generally these system identification techniques will identify a mathematical model which maps an input signal to an observed output signal. For a given model order, statistical methods will be applied on the input/output data to estimate the model parameters that best fit this set of data. The best fit criterion is based on the minimization of the error between the model output and the experimental output given by the dynamic system.

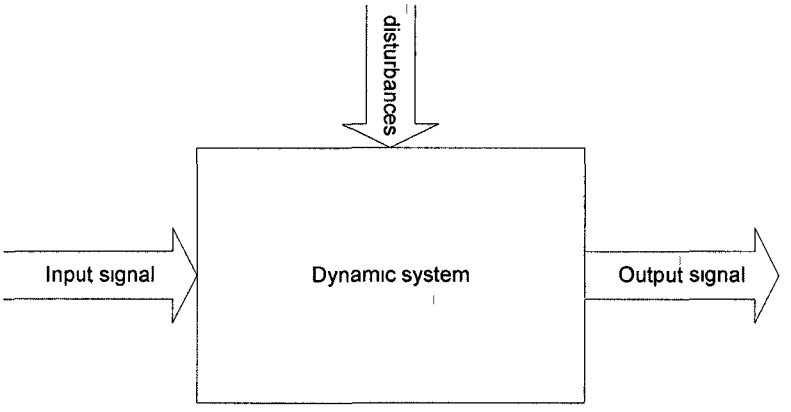

Figure 5-1 Dynamic system characterized by an input signal, an output response and a disturbance term

The system identification procedure can be summarized by the flowchart in Figure 5-2. In fact the model structure and the estimation of the unknown parameters of the model will be iterated until the validation process is fulfilled.

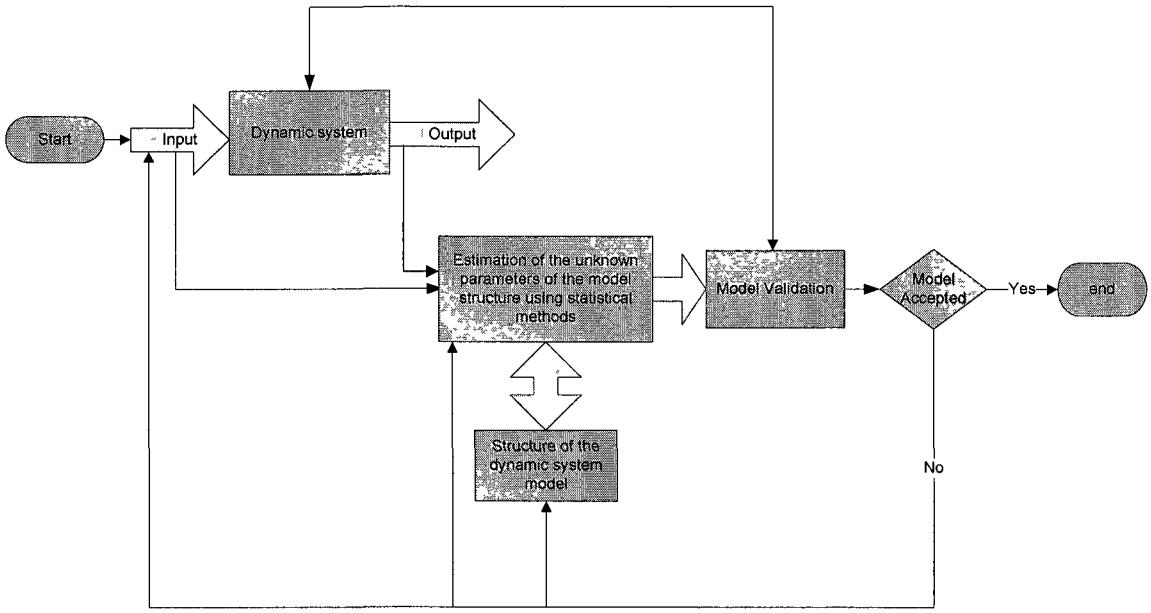

Figure 5-2 Schematic of the different steps for system identification

The need of system identification lies in the quantitative information that is provided for the dynamics of the system. Many properties could be determined and studied from these identified models (stability, performance, mechanistic discoveries, etc.) (29).

5.1.2. Arterial tissues and system identification

The idea of applying system identification techniques to soft biological tissue characterization dates to the early 80's. The purpose of using the input/output signals to a given tissue was to determine the wave amplitude attenuation coefficient dependence of the tissue in terms of the frequency. A homogeneous layer of the tissue is considered. The input signal is the transmitted source signal entering the front side of the tissue and the output signal is that portion of the signal leaving the medium on the backside. The Fourier transform is applied to these input and output signals and the ratio of these transforms, known as the frequency response function of the medium (soft tissue), is considered for the attenuation study (30; 31). In fact from Figure 5-3, $u(t)$ and $y(t)$ are transformed to $U(f)$ and $Y(f)$ (Fourier transforms). The frequency response is then derived $H_1(f) = \frac{Y(f)}{U(f)}\frac{U^*(f)}{U^*(f)} = \frac{S_{UY}(f)}{S_{UU}(f)}$, f is the frequency range, $S_{UY}(f)$ and $S_{UU}(f)$ are the cross-spectrum of u and y and auto-spectrum of u respectively. This response is

used to determine the relationship between the attenuation of the wave amplitudes the tissue thickness and the frequency.

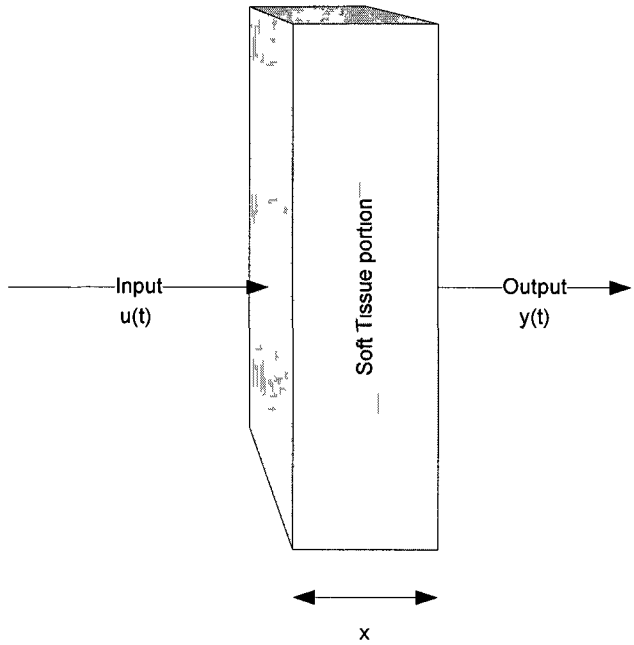

Figure 5-3 Input and output signals to a portion of a soft tissue

The same system identification approach is applied for the artery cross-section hereafter in the plaque characterization process. Since the TLM models were established previously in chapters 3 and 4, the wave which is propagating in the artery cross-section is taken from these models to serve as input and output signals to the regions of interest (inclusions on the artery or a portion of the healthy artery). Using either the regular conventional TLM model or the irregular cylindrical TLM model, the plaque location and size will be specified. Then the input and output signals to the plaque will be "recorded" via numerical simulations. These signals will be used in the system identification process to build a parametric model of this plaque. Figure 5-4 and Figure 5-5 show how the system identification process is applied to the plaque using both regular and irregular TLM models. The source signal design is paramount in capturing the arterial dynamics to be studied. Equally, the system identification method is of the same importance for the modeling process. The system identification procedure of the plaque and healthy artery will be detailed in the next section. This process will lead to different parametric models of these tissues depending of their geometric and acoustics properties.

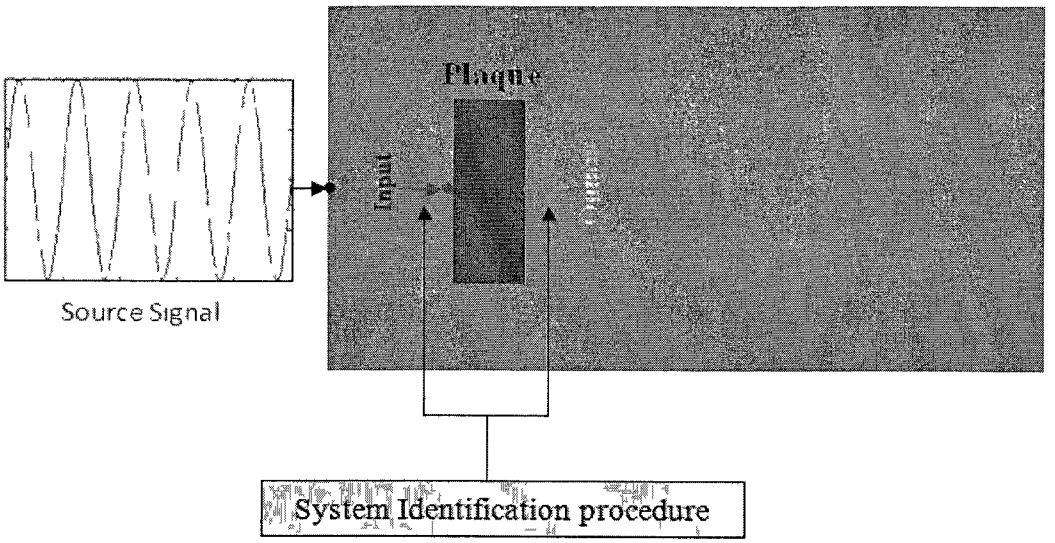

Figure 5-4 System identification approach applied to the plaque portion using regular TLM model

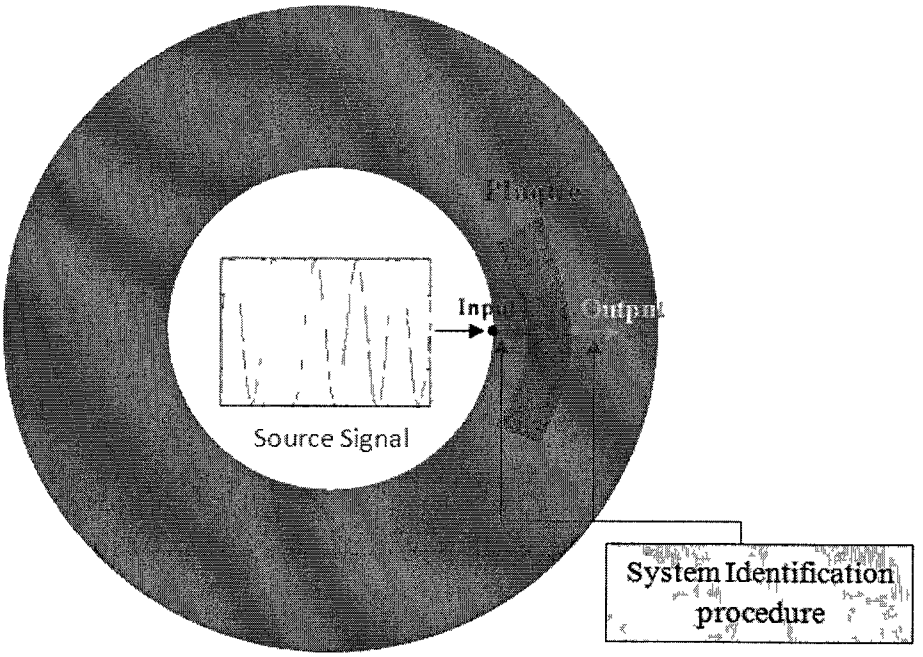

Figure 5-5 System identification approach applied to the plaque using cylindrical irregular TLM model

5.1.3. System identification process of the artery tissue components

Three essential components in the system identification include: the design of the input signal, the choice of the model structure and the choice of the system identification method.

5.1.3.1. Persistency of excitation of the input signal

Any input signal used in the context of system identification must meet certain condition. In particular, the input signal should be ***persistently exciting***. The frequency domain condition enforcing a persistency of excitation is:

A signal $u(t)$ *characterized by its spectrum* $\Phi_u(\omega)$ *is said to be persistently exciting if*

$$\Phi_u(\omega) > 0 \qquad \textit{for almost all } \omega \quad (32)$$

Thus the spectrum may be zero on a set of number of points (almost all definition).

One classical frequency-rich signal is the swept sine signal which is also known as the "chirp signal". The chirp signal is a single sine wave with a frequency that is changing continuously as a function of time.The general mathematical presentation of the swept sine wave is

$$u(k) = A\sin\left(2\pi\beta(k) * \frac{(k-1)}{f_s} + \varphi\right) + B$$

$$\beta(k) = f_{\min} + \frac{(f_{\max} - f_{\min})}{2t_{target}}\left(\frac{k-1}{f_s}\right) \text{ where } f_s \geq 2f_{\max}$$

A is the wave amplitude, B is the signal bias term, φ is the phase angle of the wave and $\beta(k)$ is the time varying frequency of the swept sine in Hertz. The frequency f_s is the sampling frequency. The frequency $\beta(k)$ in this case is a linearly varying frequency over the interval $[f_{\min}, f_{\max}]$. The target time, denoted as t_{target}, is the time for which the upper bound of the frequency range is achieved.

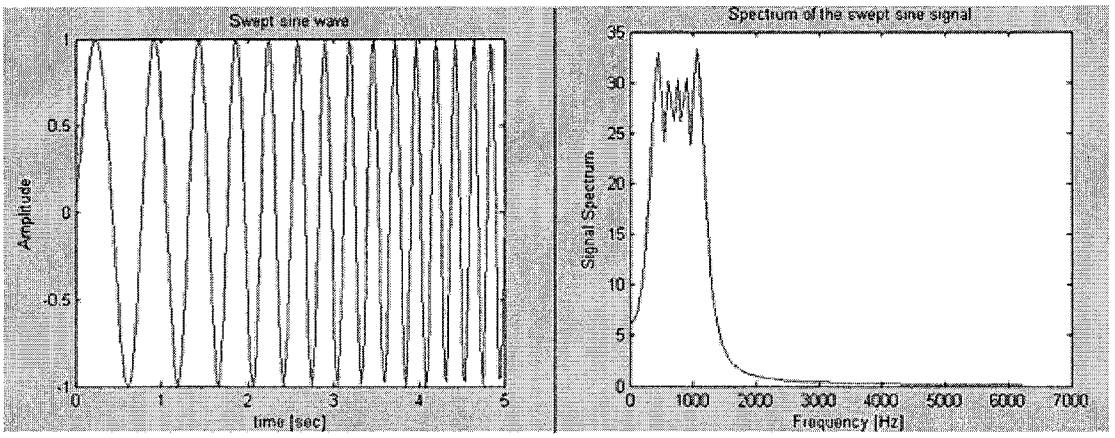

a) b)

Figure 5-6 a) Swept sine signal, b) Swept sine power spectrum

Illustrated in Figure 5-6 a), is a swept sine that is constructed using Matlab. It can be seen from Figure 5-6 b) that the auto-spectrum satisfies the condition of persistent excitation (auto-spectrum is non zero in almost all the frequency range).

During the system identification process of the plaque and healthy tissue characterization, a swept sine will be designed as the source signal. From literature, the frequency range used in the signal processing for the soft tissue is in the range of $\lfloor 10^5, 10^7 \rfloor Hz$. The swept sine is therefore designed such that the frequency covers this range.

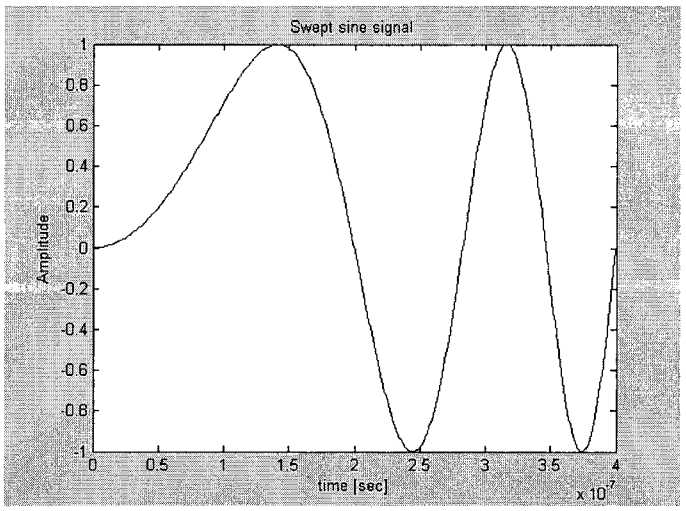

Figure 5-7 Swept sine signal where the frequency range is between $\lfloor 10^4, 10^7 \rfloor Hz$

This signal will be combined with a zero-element vector. As illustrated in Figure 5-8, a swept sine is designed to be the source signal of the simulation part for the TLM models. The sampling time of this signal is equal to 10^{-9} sec

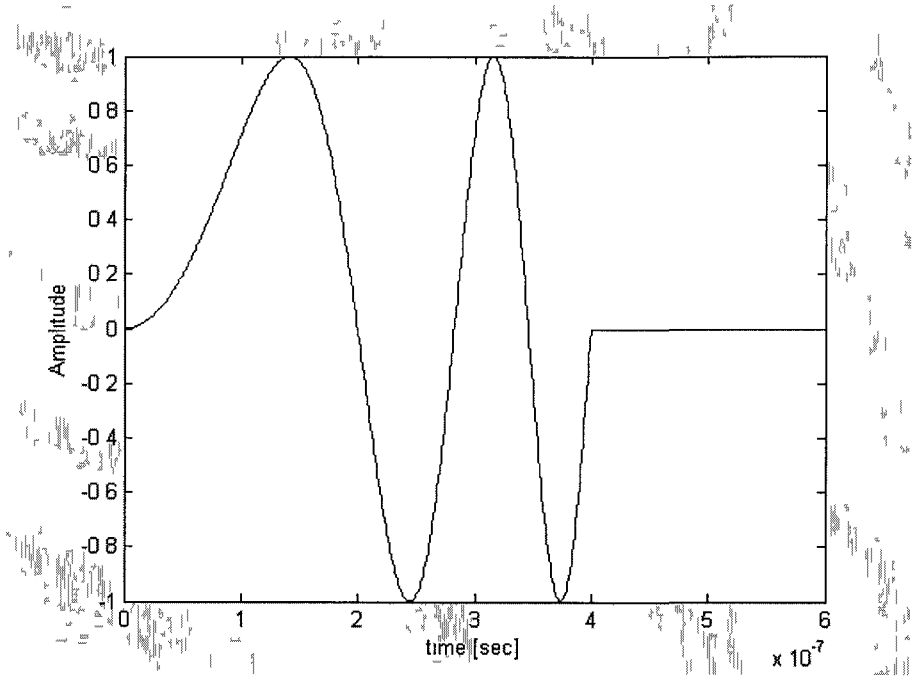

Figure 5-8 Constructed swept sine pulse

5.1.3.2. Model structure

For a given dynamic system, it is necessary to introduce tools that determine how its parameters relate to each other. This relationship is called the model of the dynamic system. These models can be divided into two main categories: non-parametric and parametric models. Non-parametric models are presented in the form of graphs mainly Bode plots (magnitude and phase of the transfer function of the system). These frequency response functions (FRFs) are mainly used for linear system to analyze its dynamics. Parametric models on the other hand are described by a mathematical relationship (difference equations relating the input and output signals). These models offer a sophisticated and rigorous quantitative analysis of the system properties. They are also used for simulations and forecasting purposes.

Since the purpose of this study is quantitative tissue characterization, a parametric modeling approach will be sought. The model structure for the different tissue components of the artery cross-section will be unknown a priori. The collected input and output signals will be inputted to an appropriate system identification technique to determine the model structure.

5.1.3.3. System identification method

This process is composed of two stages. **In the first stage**, the identification technique that is used for modeling purposes is the so-called *Orthogonal Least Squares* (OLS) method (53,54). This method is a discrete time domain based approach where the time signals are used for model determination. In fact, the transient time domain information generated from the TLM artery models and their delayed components will be used as possible input regressors. This method will determine the most significant regressors from a broad range of possible candidates to identify the best parametric model. The general model structure can be linear or nonlinear. However for this work, it is anticipated that only a linear model will be needed.

A discrete time model generally resembles a polynomial structure. Considering a general case, a discrete system model with unknown coefficients (model parameters to be estimate) can be transformed into the linear-in-the-parameters representation by means of the expansion

$$z(k) = \sum_{i=1}^{M} p_i(k)\theta_i + \xi(k), \quad k = 1,\ldots,N, \tag{5-1}$$

where $z(k)$ is the output, $p_i(k)$ are the monomials of the different inputs up to certain degree M, θ_i are the unknown parameters of the model to be estimated, $\xi(k)$ is the modeling error and N is the data length.

Equation (5-1) can be transformed to the matrix form

$$Z = P\Theta + \Xi. \tag{5-2}$$

Given this formulation, a linear least squares problem emerges. The proposed Orthogonal Least Squares (OLS) method systematically searches the entire regressor space (monomials) as precised in equation (5-2) to find the best error reduction set, transforms these optimal regressors into orthogonal components, and then perform final regressor identification based on the new orthogonal system. These estimates will be mapped back to the original parameter estimates with their relative regressors given in equations (5-1) and (5-2). This is called Parameter Estimation (PE). Structure Selection (SS) algorithm is then applied where it is anticipated that a linear model will emerge. This procedure takes the estimated parameters and statistically prioritizes these regressors into the most significant regressor, second most significant regressor and so on until accuracy of the model output is realized (see Figure 5-9).

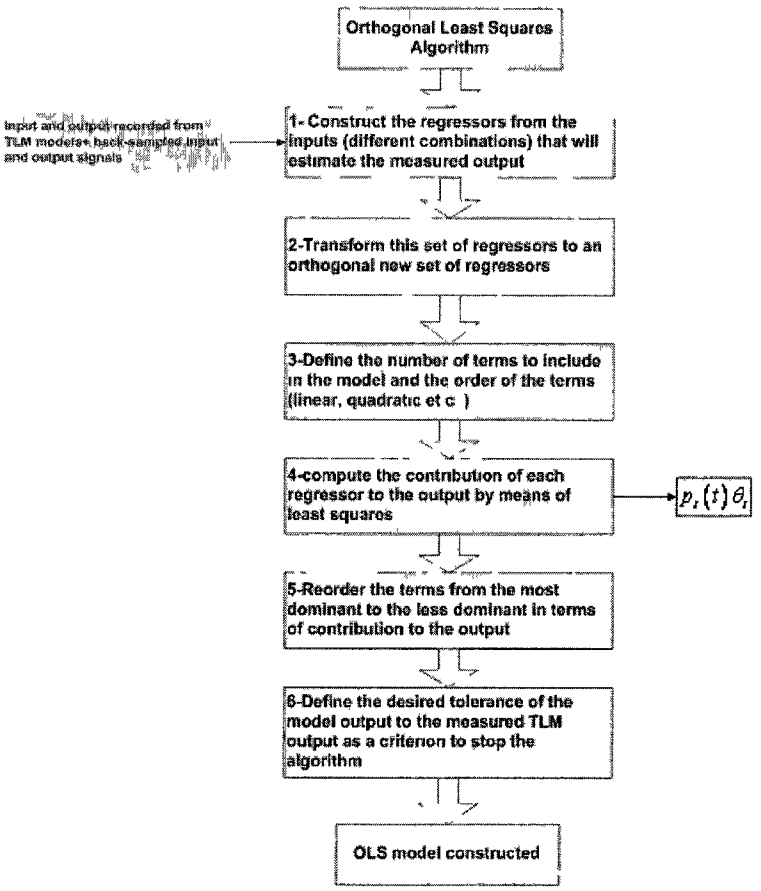

Figure 5-9 Flowchart of the orthogonal least squares method

The second stage is characterized by the estimation of the model coefficients. A second system identification technique called *recursive least squares* (RLS) is used (29). This method departs from a system of linear equations in the matrix form

$$Y = P\Theta, \tag{5-3}$$

where $\Theta \in \Re^{M\times 1}$ is the unknown parameters of the model to be determined, $Y \in \Re^{N\times 1}$ is the output vector $P \in \Re^{N\times M}$ is the information matrix which is function of the input and output vectors.

The utility of this method is to calculate the inverse of the information matrix. Based on an algorithm that is composed of three equations, the inverse matrix is simply calculated by means of additions and multiplications. The RLS method details are included in the implementation appendix RLS. Finally once the inverse of the information matrix is found, the model coefficient vector Θ can be calculated from equation (5-3).

5.2. Tissue characterization using regular and cylindrical irregular TLM models

As developed in the previous section, a swept sine wave will be considered as the source signal. This choice of the input came out from a thorough investigation on the impact of some designed inputs on the model structure to be identified by OLS. A set of inputs were designed. This set was composed of a swept sine, a Schroeder wave, a pulse and a band limited white noise. Swept sine and Schroeder wave signals were the more appropriate candidates since they are characterized by their frequency-rich content and their persistent excitation property. During the model structure identification all the considered inputs except the swept sine gave different model structure of the plaque while its properties were changed. That is why, the swept sine signal was considered to be the best input that captures the dynamics of the studied plaques.

First a regular TLM model will be developed where a plaque having different acoustic/physical properties will be included. A parametric model will be generated for the plaque portion in the regular TLM model. An irregular TLM model will then be

generated where the same plaque will be inserted. Using the same system identification technique, a plaque model will be constructed for both cases.

5.2.1. Tissue characterization using regular TLM model

5.2.1.1. Model structure determination

A medium composed of 90 by 300 nodes in the horizontal and vertical directions respectively is constructed using the regular TLM model. The plaque is located between the 10th and 30th horizontal nodes and 25th and 65th vertical nodes.

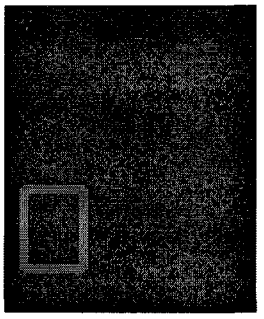

Figure 5-10 Plaque inserted in the regular medium

The designed swept sine signal is composed of 600 data points with a sampling time that is equal to 10^{-9} sec and a frequency range of $[10^4, 10^7]Hz$. This input was injected at the 1st horizontal and 45th vertical node. The 45th vertical direction coincides with the middle line crossing the plaque. The input (10th radial position) and output (31st radial position) signals to the plaque are recorded. Since the plaque characterization lies on parametric modeling, these input/output signals will be used in the OLS algorithm to construct such models. In fact, the OLS algorithm is applied for the input/output data according to each plaque characteristics (acoustic density and speed). The results generated by OLS are presented in a form of parametric model linking the current output to the previous outputs and inputs

$$y(t) = \sum_{i=1}^{n_a} a_i y(t-i) + \sum_{j=0}^{n_b} b_j u(t-j). \tag{5-4}$$

The OLS will be the decisive tool of *the model structure determination for the plaque* The system identification approach is always seeking a model which gives the maximum of accuracy with respect to the real dynamic system.

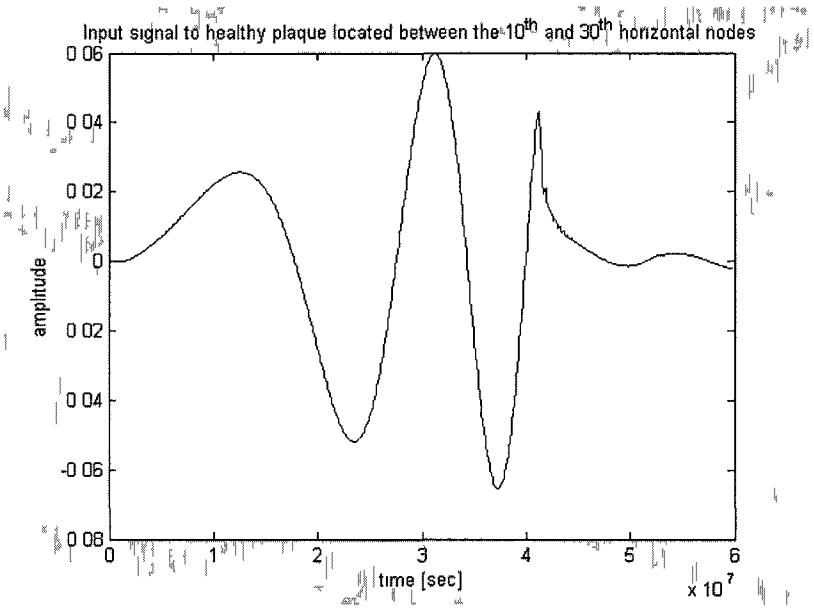

Figure 5-11 Input signal to healthy plaque that has a delay of 10 time samples

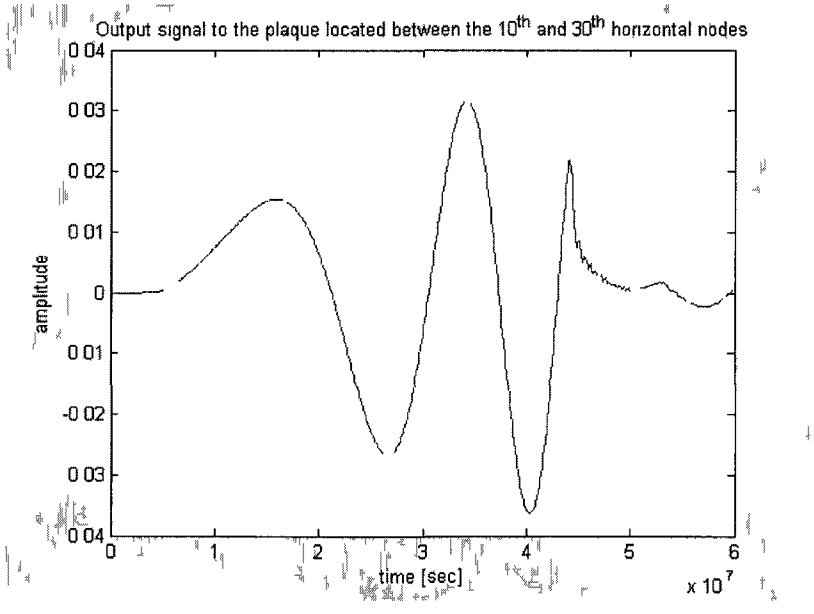

Figure 5-12 Output signal to healthy plaque that has a delay of 30 time samples

A preprocessing step should be done for the input and output signals obtained as illustrated in Figure 5-11and Figure 5-12 before applying the system identification

technique. In this step the trend value of the signals are eliminated to guarantee the zero-trend value property of the data. This elimination is performed via Matlab by means of "detrend" commands which removes any trend that could exist in the signal. In addition, the delay between both signals is taken out. The way this delay was removed is by just getting rid of the time delay resulted from the propagation time that the wave is taking from the considered input node to the output node.

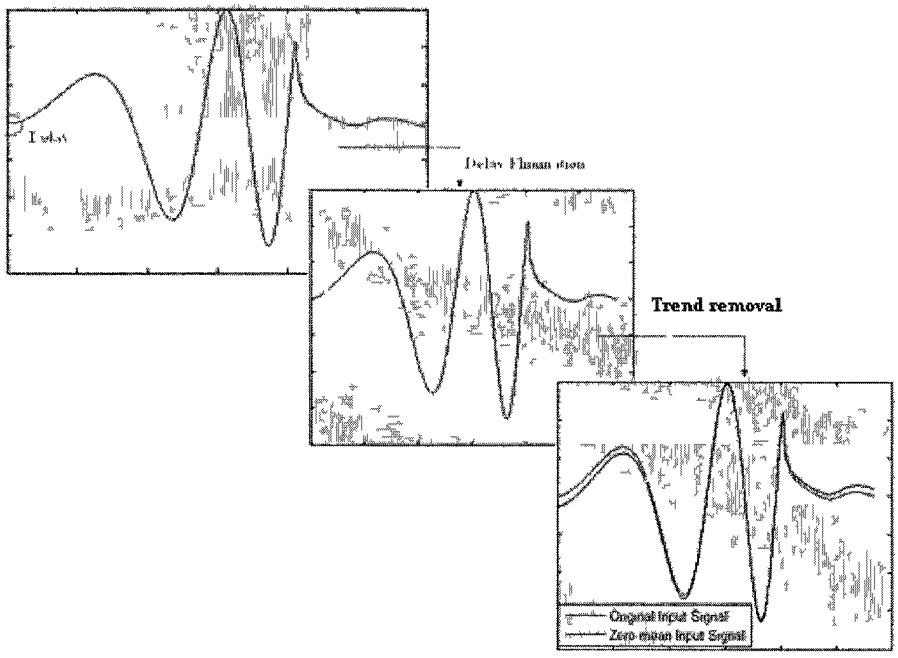

Figure 5-13 Preprocessing of the input and output signals to the plaque

After preprocessing, the OLS algorithm is applied to the input/output sets of data and a discrete parametric model is established for the plaque. The following simple first order linear model is generated for the different plaques

$$y(k) = a_1 y(k-1) + b_0 u(k), \tag{5-5}$$

where $y(k)$ is the model output of the plaque and $u(k)$ is the input to the plaque.

The OLS provides the model output versus the actual TLM output to the plaque. Figure 5-14 and Figure 5-15 illustrate the generated model output and the error estimation between this model output and the actual TLM output.

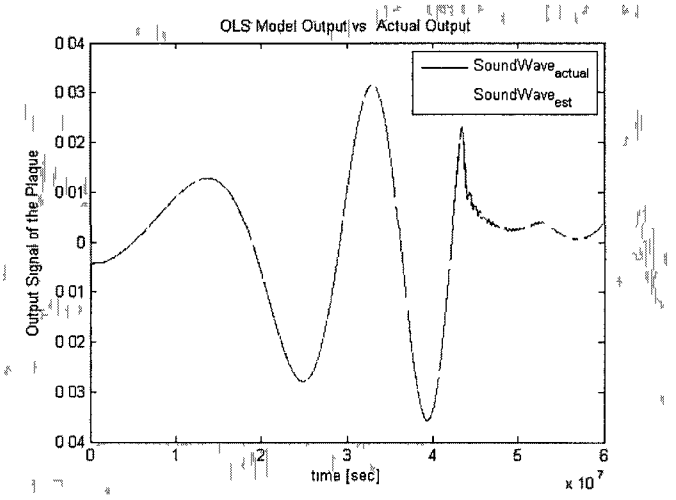

Figure 5-14 model and actual outputs for a healthy tissue

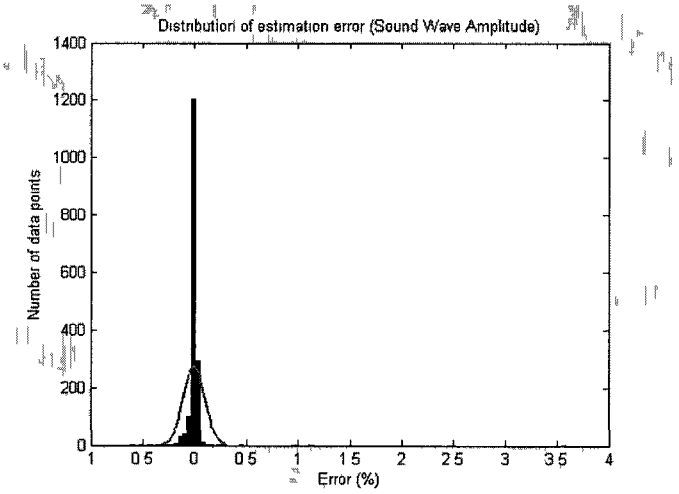

Figure 5-15 Error histogram between the model output and the actual output

5.2.1.2. Model Coefficients determination

In order to investigate the effect of plaque acoustic properties variation on the model, a first order continuous model is derived from the input/output data sets

$$\tau y(t) + y(t) = du(t). \tag{5-6}$$

d is the DC gain and τ the time constant

The DC gain and the time constant are determined using different approximations of the first derivative of the output, $\dot{y}(t)$. These approximations calculations were performed to test the robustness of the model coefficients when recovering continuous model from

discrete model. Multiple first time derivate approximations were performed to recover the continuous model calculations. The model coefficients were calculated and compared using these approximations and the error variation was negligible. The results are detailed hereafter.

Centered first order derivative approximation: The first derivative is approximated by $\dot{y}(t) = \frac{y(i+1) - y(i-1)}{2\Delta t}$.

Equation (5-6) becomes $\tau \frac{y(i+1) - y(i-1)}{2\Delta t} + y(i) = du(i)$,

$$y(i) = -\tau \frac{y(i+1) - y(i-1)}{2\Delta t} + du(i). \tag{5-7}$$

Forward second order derivative approximation: The first derivative is approximated by $\dot{y}(i) = \frac{-y(i+2) + 4y(i+1) - 3y(i)}{2\Delta t}$,

Equation (5-6) becomes $\tau \frac{-y(i+2) + 4y(i+1) - 3y(i)}{2\Delta t} + y(i) = du(i)$,

$$y(i) = -\tau \frac{-y(i+2) + 4y(i+1) - 3y(i)}{2\Delta t} + du(i). \tag{5-8}$$

Backward second order derivative approximation: The first derivative is approximated by $\dot{y}(i) = \frac{3y(i) - 4y(i-1) + y(i-2)}{2\Delta t}$.

Equation (5-6) becomes $\tau \frac{3y(i) - 4y(i-1) + y(i-2)}{2\Delta t} + y(i) = du(i)$,

$$y(i) = -\tau \frac{3y(i) - 4y(i-1) + y(i-2)}{2\Delta t} + du(i). \tag{5-9}$$

Centered fourth order derivative approximation: The first derivative is approximated by $\dot{y}(i) = \frac{-y(i+2) + 8y(i+1) - 8y(i-1) + y(i-2)}{12\Delta t}$.

Equation (5-6) becomes $\tau \frac{-y(i+2)+8y(i+1)-8y(i-1)+y(i-2)}{12\Delta t}+y(i)=du(i)$,

$$y(i)=-\tau \frac{-y(i+2)+8y(i+1)-8y(i-1)+y(i-2)}{12\Delta t}+du(i). \qquad (5\text{-}10)$$

Equations (5-7), (5-8), (5-9) and (5-10) reduce to the matrix equality

$$Y=P\Theta, \qquad (5\text{-}11)$$

where $\Theta=[b \quad \tau]^T$ is the unknown parameters to be determined, Y is the output vector and P is the information matrix which is function of the input and output vectors.

The identification of the model parameter vector Θ is found using ***least-squares-based algorithms.*** Generally the four-step instrumental variable method is used to improve the least squares estimates by reducing bias generated by noise or un-modeled disturbances.

Since the output/input data sets are recorded from a purely computational model, these signals are noise free. Hence ***the recursive least squares*** technique is used to identify the model coefficients in equation (5-6).

As developed in Chapter 3, the plaque inserted inside the healthy tissue will produce a reflection/transmission phenomenon due to this change along the four edges of the plaque. Considering $Z_{Plaque}=c_{Plaque}\rho_{PLaque}$ and $Z_{Artery}=c_{artery}\rho_{Artery}$ to be the acoustic impedances of the plaque and artery, then the reflection and transmission coefficients are

$$R=\frac{Z_{Plaque}-Z_{Artery}}{Z_{Plaque}+Z_{Artery}},$$

$$T=1-\frac{Z_{Plaque}-Z_{Artery}}{Z_{Plaque}+Z_{Artery}}. \qquad (5\text{-}12)$$

The characterization of the plaque will be linked to the model coefficients and mainly the DC gain. The DC gain is expected to decrease if the impedance is increasing. This is explained by the fact that if the acoustic impedance is going up then the density of the plaque is increasing, meaning that this portion of tissue is getting harder and denser

mechanically. A denser material has a repulsive effect and the transmitted signal into it is minor. This means that the denser the material is the more resistive effect it shows. Therefore if the impedance goes up then the DC gain is expected to decrease.

In the TLM model, the plaque acoustic impedance is increased gradually and the input/output data sets to this plaque are recorded. The model coefficients (DC gain and pole location) are calculated using the different approximations described in equations (5-7), (5-8), (5-9) and (5-10). The same coefficients values are obtained using these different approximations.

Acoustic Impedance $[Kgm^{-2}s^{-1}]$	DC gain d
$Z_{healthyTissue} = 1559216$	0.5634
$Z = 1.2 \times Z_{healthyTissue}$	0.5171
$Z = 1.4 \times Z_{healthyTissue}$	0.4778
$Z = 1.6 \times Z_{healthyTissue}$	0.4442
$Z = 1.8 \times Z_{healthyTissue}$	0.4149
$Z = 2 \times Z_{healthyTissue}$	0.3893

Table 5-1 DC gain variation as function of the acoustic impedance of the plaque (regular TLM model)

Table 5-1 confirms that the DC gain is indeed decreasing when the acoustic impedance of the plaque in increased.

Table 5-2 shows that the pole location or the time constant τ (indicator of the time response of the system) is decreasing likewise the DC gain when the acoustic impedance is increased. This is could be explained physically by the fact that the increase of the hardness of the tissue (the plaque) will affect the speed of the system response.

Acoustic Impedance $[Kgm^{-2}s^{-1}]$	Time constant τ
$Z_{healthyTissue} = 1559216$	22.15
$Z = 1.2 \times Z_{healthyTissue}$	21.95

$Z = 1.4 \times Z_{healthyTissue}$	21.81
$Z = 1.6 \times Z_{healthyTissue}$	21.71
$Z = 1.8 \times Z_{healthyTissue}$	21.64
$Z = 2 \times Z_{healthyTissue}$	21.61

Table 5-2 Time constant variation as function of the acoustic impedance of the plaque (regular TLM model)

It has been shown that both DC gain and time constant of the first order model are decreasing when the acoustic impedance of the plaque is increasing. This result confirms what is expected to happen physically. The coefficients variations are summarized in Table 5-3 and Table 5-4.

Acoustic Impedance $[Kgm^{-2}s^{-1}]$	Acoustic impedance change [%]	DC gain d	DC gain change [%]
$Z = 1.2 \times Z_{healthyTissue}$	20	0.5224	−8.22
$Z = 1.4 \times Z_{healthyTissue}$	40	0.5090	−15.19
$Z = 1.6 \times Z_{healthyTissue}$	60	0.4910	−21.16
$Z = 1.8 \times Z_{healthyTissue}$	80	0.4699	−26.36
$Z = 2 \times Z_{healthyTissue}$	100	0.4472	−30.90

Table 5-3 DC gain variation in percentage (regular TLM model)

Acoustic Impedance $[Kgm^{-2}s^{-1}]$	Acoustic impedance change [%]	Time Constant τ	Time Constant change [%]
$Z = 1.2 \times Z_{healthyTissue}$	20	25.04	−0.9
$Z = 1.4 \times Z_{healthyTissue}$	40	23.28	−1.5
$Z = 1.6 \times Z_{healthyTissue}$	60	21.34	−1.99
$Z = 1.8 \times Z_{healthyTissue}$	80	19.3	−2.3
$Z = 2 \times Z_{healthyTissue}$	100	17.28	−2.44

Table 5-4 Time constant variation in percentage (regular TLM model)

5.2.2. Tissue characterization using cylindrical irregular TLM model

Using the cylindrical irregular TLM model, a disk can be deformed to a rectangular shape by making the radius range much bigger than the angular interval. The shape is transformed exactly to a rectangular shape that has the same thickness and number of radial nodes as of the regular TLM case (Figure 5-16). The same plaque size and location as of the regular TLM model is considered. The plaque is located between the 10th and 30th radial nodes and 25th and 65th angular nodes.

The same designed swept sine signal is injected at the 1st radial and 45th angular node. The 45th angular direction coincides with the middle line crossing the plaque. The input (10th radial position) and output (31st radial position) signals to the plaque are recorded. Similarly to the regular data sets, the same preprocessing step is performed before applying the OLS algorithm for model identification.

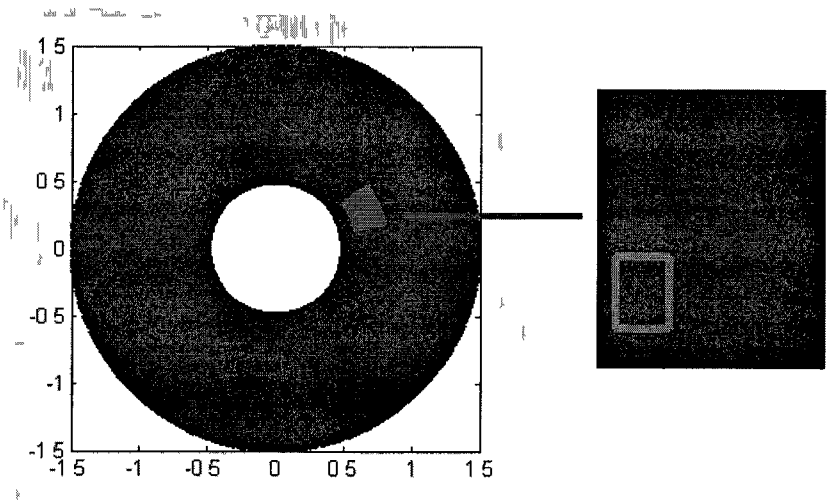

Figure 5-16 Plaque inserted in the circular irregular medium and transformed to a rectangular medium

The same model structure is found by OLS for the cylindrical irregular TLM model $y(t) = a_1 y(t - \Delta t) + b_0 u(t)$.

The acoustic wave leaving the plaque is $y(t)$, $u(t)$ is the acoustic input to the plaque and Δt the sampling time.

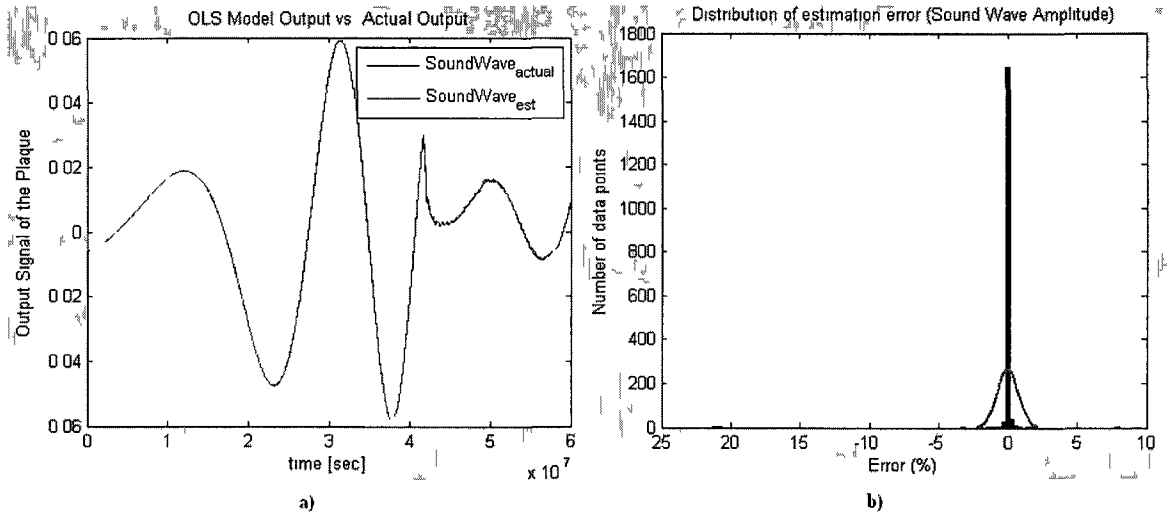

Figure 5-17 Plaque inserted in the circular irregular medium

Illustrated in Figure 5-17 a) is the actual plaque output versus the model output of the plaque. Shown in Figure 5-17 b) is the error histogram between those two signals for a given impedance value of the plaque.

In the cylindrical irregular TLM model the transmission/reflection phenomena as developed in Chapter 4 is function of the densities change between the healthy tissue and the plaque

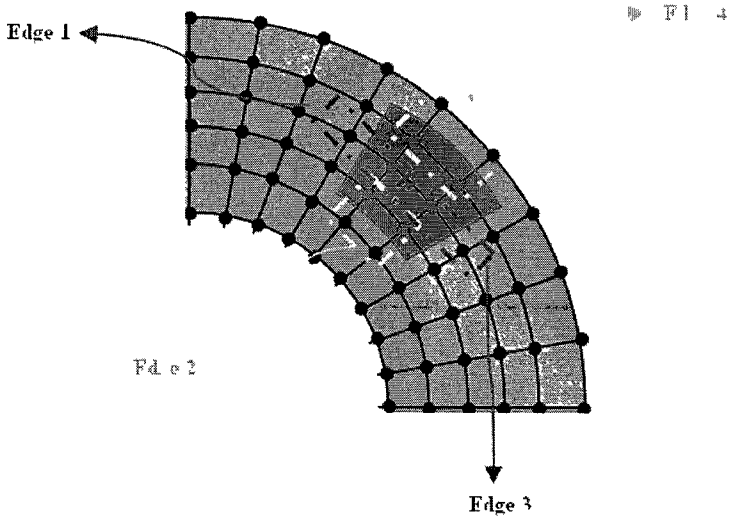

Figure 5-18 Reflection/transmission across the plaque edges

In fact, for Edges 2 and 4 the reflection and transmission coefficients are respectively given by:

$$R_1 = \frac{Z_2(r+dr,\theta) - Z_4(r,\theta)}{Z_2(r+dr,\theta) + Z_4(r,\theta)}, T_1 = 1 - R_1 \text{ and } R_2 = \frac{Z_4(r,\theta) - Z_2(r+dr,\theta)}{Z_4(r,\theta) + Z_2(r+dr,\theta)}, T_2 = 1 - R_2 .$$

It can be seen that theses reflection/transmission coefficients are function of the lines impedances. These impedances are function of the density of the medium where the lines are ($Z_r = \frac{wdr\rho_r}{rd\theta} Z_{ref}$ and $Z_\theta = \frac{wrd\theta\rho_r}{dr} Z_{ref}$). Thus to study the plaque type effect on the model coefficients, the variation of the DC gain and pole location is studied as function of the plaque density variation. Therefore the speed is set constant and the density of the plaque is varying with respect the healthy tissue density. The same approximations specified in *the model coefficients determination* section are used to determine the coefficients of the continuous model in equation (5-6).

Acoustic Impedance $[Kgm^{-2}s^{-1}]$	DC gain d
$Z_{healthyTissue} = 1559216$	0.5275
$Z = 1.2 \times Z_{healthyTissue}$	0.5224
$Z = 1.4 \times Z_{healthyTissue}$	0.509
$Z = 1.6 \times Z_{healthyTissue}$	0.491
$Z = 1.8 \times Z_{healthyTissue}$	0.4699
$Z = 2 \times Z_{healthyTissue}$	0.4472

Table 5-5 DC gain variation as function of the acoustic impedance of the plaque (cylindrical irregular TLM model)

Acoustic Impedance $[Kgm^{-2}s^{-1}]$	Time Constant τ
$Z_{healthyTissue} = 1559216$	26.42
$Z = 1.2 \times Z_{healthyTissue}$	25.04
$Z = 1.4 \times Z_{healthyTissue}$	23.28
$Z = 1.6 \times Z_{healthyTissue}$	21.34
$Z = 1.8 \times Z_{healthyTissue}$	19.3
$Z = 2 \times Z_{healthyTissue}$	17.28

Table 5-6 Pole location variation as function of the acoustic impedance of the plaque (cylindrical irregular TLM model)

As in the case of the regular TLM model section, it is expected that both the DC gain and the time constant to decrease when the acoustic impedance of the plaque is increased and this is what is presented in Table 5-5 and Table 5-6.

It can be seen from both models that a plaque could be characterized by a first order system. In fact the coefficients variation of this model is inversely proportional to the acoustic impedance variation. The coefficients variations are summarized in the following tables.

Acoustic Impedance $[Kgm^{-2}s^{-1}]$	Acoustic impedance change [%]	DC gain d	DC gain change [%]
$Z = 1.2 \times Z_{healthyTissue}$	20	0.5224	−0.97
$Z = 1.4 \times Z_{healthyTissue}$	40	0.509	−3.51
$Z = 1.6 \times Z_{healthyTissue}$	60	0.491	−6.92
$Z = 1.8 \times Z_{healthyTissue}$	80	0.4699	−10.92
$Z = 2 \times Z_{healthyTissue}$	100	0.4472	−15.22

Table 5-7 DC gain variation in percentage (cylindrical irregular TLM model)

Acoustic Impedance $[Kgm^{-2}s^{-1}]$	Acoustic impedance change [%]	Time Constant τ	Time Constant change [%]
$Z = 1.2 \times Z_{healthyTissue}$	20	25.04	−5.22
$Z = 1.4 \times Z_{healthyTissue}$	40	23.28	−11.88
$Z = 1.6 \times Z_{healthyTissue}$	60	21.34	−19.23
$Z = 1.8 \times Z_{healthyTissue}$	80	19.3	−26.95
$Z = 2 \times Z_{healthyTissue}$	100	17.28	−34.6

Table 5-8 Time constant variation in percentage (cylindrical irregular TLM model)

5.3. Soft and hard plaque characterization:

The model coefficients identification can be applied to differentiate between soft and hard plaques in arteries. The difference between soft and hard plaque are dictated by the difference in their acoustic properties. A hard plaque is characterized by high acoustic impedance with respect to the healthy artery tissue whereas a soft plaque has low acoustic impedance compared to the healthy tissue.

Acoustic Impedance	DC gain d	Time constant τ
Soft plaque	0.727	22.776
Hard plaque	0.201	21.026

Table 5-9 Model coefficients variation as function of the plaque type (regular TLM model)

Acoustic Impedance	DC gain d	Time constant τ
Soft plaque	0.439	24.97
Hard plaque	0.11	0.46

Table 5-10 Model coefficients variation as function of the plaque type (cylindrical irregular TLM model)

Despites the difference in the coefficients variation between the regular TLM and cylindrical irregular TLM models, it has been shown that both the DC gain and time constants are decreasing when the acoustic impedance is increasing. The soft plaque is characterized by a high DC gain compared to the hard plaque.

The considered hard plaque is characterized by an acoustic impedance that is five times higher than the normal tissue. The soft plaque is characterized by an acoustic impedance that is half of the healthy tissue.

Considering the model structure found during the tissue characterization, the plaque can be viewed as ***a first order low pass filter***. This first order filter illustrated in Figure 5-19 is characterized by a DC gain and a time constant that decrease when the resistance R_1 is increasing.

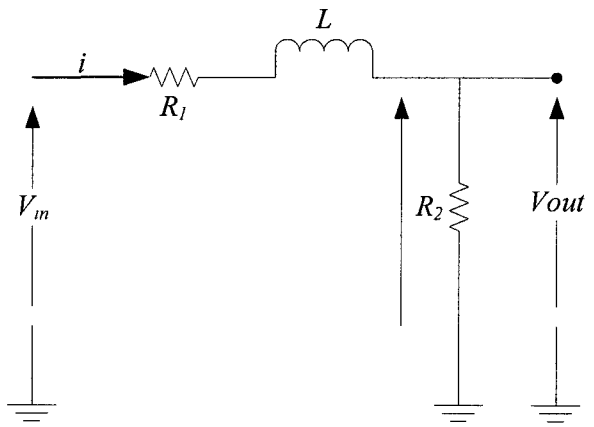

Figure 5-19 RL low pass filter

$$V_{out} = R_2 i \Leftrightarrow i = \frac{V_{out}}{R_2}.$$

$$V_{in} = R_1 i + L\frac{di}{dt} + V_{out}$$
$$\Leftrightarrow V_{in} = \frac{R_1}{R_2}V_{out} + \frac{L}{R_2}\frac{dV_{out}}{dt} + V_{out}.$$

Applying Laplace transform for the above equation

$$V_{in} = \left[\frac{R_1}{R_2} + 1 + \frac{L}{R_2}s\right]V_{out}$$
$$\Leftrightarrow \frac{V_{out}}{V_{in}} = \frac{1}{\frac{R_1 + R_2}{R_2} + \frac{L}{R_2}s}.$$

The transfer function of this filter is the following

$$TF = \frac{\dfrac{R_2}{R_1 + R_2}}{1 + \dfrac{L}{R_1 + R_2} s} . \tag{5-13}$$

The resistance R_1 and R_2 can be linked to the acoustic impedance of the medium. From the transfer function above, if R_1 and R_2 increases the DC gain and the time constant decrease.

5.4. Summary

In this chapter both regular and irregular TLM models were considered to emulate ultrasound information transmitted through the studied tissue. System identification techniques were used to differentiate between the healthy tissue and different plaques (inclusions inserted in the healthy tissue in the TLM models). Special attention was given to parametric identification methods to construct a plaque model. This model is characterized by quantifiable coefficients that vary according to each plaque characteristics. The identification was characterized by a two-stage process. The model structure was firstly determined by means of *the orthogonal least squares method.* The plaque inclusion was found to be a first order system. Secondly the model coefficients estimation was performed by means of *the recursive least squares method.*

By varying the acoustic properties of the plaque the model coefficients were calculated accordingly. It has been shown that when the acoustic impedance of the plaque is increased the DC gain and time constant are decreasing. The DC gain decrease could be explained physically by the fact that the increase of the acoustic impedance implies the increase of the resistance of the plaque which is inversely proportional to the DC gain. The same thing applies for the time constant behavior.

It has been shown that the plaque characteristics can be characterized quantitatively based on the ultrasound waves using the system identification approach. This methodology could be applied on the real IVUS Radio-Frequency signals.

Chapter 6 Conclusions

This work was composed of two main parts. ***A modeling process***, which produced a set of data describing the ultrasound propagation in rectangular and circular media, was developed. ***A post-processing process*** that used the generated data from these developed models for tissue characterization.

In the first part of this thesis, ultrasound wave propagation through biological tissues and specifically through arterial wall was studied. This modeling work was twofold. First it departed from a simple regularly-shaped medium (rectangular geometry) where a transmission line matrix (TLM) model was employed to capture the ultrasound wave propagation. In a second step an irregular TLM model was constructed based on a circular-shaped medium (disk) to simulate IVUS. Both of these models were based on the discretization of the medium where the Huygens principle was applied in the propagation process from one node to another. These models offered the possibility of introducing any kind of inclusion inside the simulated medium in terms of geometric and acoustic properties. Additionally, any type of ultrasonic wave source could be inserted anywhere in these models. Moreover the propagating ultrasound waves were recorded in a digitized format in any location at any time specified during the numerical simulation.

In the second part, advanced system identification techniques were introduced and applied to characterize tissues. This approach used specific simulated waves in terms of locations to serve as the input/output data sets for the dynamic identification of these regions of interest. This characterization was based upon the construction of parametric models in the form of transfer function where its coefficients are directly related to each plaque type. A first order structure was thus found for all plaque types with different DC gain and time constant values depending on the properties of these inclusions.

A quantitative study was performed to link the variation of these two parameters with respect to acoustic properties. it has been shown consequently that these plaque characteristics were identified quantitatively based on the ultrasound waves using the system identification approach.

In the rest of this chapter, contributions of this work will be enumerated. Then future directions will be proposed to extend the use of our system identification approach for arterial plaque characterization.

6.1. Contributions

The contributions in this work involved both modeling and tissue characterizations parts. These contributions are enumerated herein. In the modeling section our inputs have touched many aspects:

- Ultrasound propagation model has been extended from regular medium (rectangular geometry) to the circular case to simulate appropriately IVUS (disk shape in accordance with the artery cross-section).
- Flexibility of the model to design any ultrasound source wave at any preferred location.
- Easiness of inserting inclusions to model plaques (size, location and acoustic properties).
- Ability of recording propagating ultrasound wave time signals in all locations in the medium.

In the tissue characterization parametric system identification was for the first time used:

- An optimized ultrasound source signal was designed. In fact a broadband frequency signal that is persistently exciting was applied to guarantee full dynamic response of the tissue or plaques.
- Robust system identification techniques that are invulnerable towards noise effects were employed.
- An accurate procedure consisted of model structure determination of the plaque followed by model coefficients determination was adopted.
- A real quantitative characterization of the arterial tissue and plaques was achieved based on the identified parametric models.

6.2. Future work

The performed modeling part served as a tool to simulate IVUS. This simulated IVUS helped to acquire ultrasound time signals which replaced the real radio-frequency echoes of IVUS. These signals were used after that for the tissue characterization process.

This characterization approach should be extended to be applied on real RF echoes of the IVUS. In this proposed future work line, the same technique to diagnose the presence of plaque in arteries will be used. An experimental setup will be developed by acquiring IVUS equipment. Experiments will be performed on human coronary artery-like tubes where all the acoustic properties will be preserved. Different plaques will be included in these tubes. Time domain identification techniques developed in this thesis will be applied to the recorded data via the IVUS system.

In a second stage, based on the parametric models generated by these techniques a HD image of the artery cross-section will be reconstructed. The colors of this image will be function of the model coefficients variations. As a mean of validation of these methods, the constructed HD images will be compared to the actual Artery like tube cross-sections.

A special attention should be directed to the design of the source wave. First, broadband excitation signals should be designed and used which in turn gives a full dynamic response of the artery cross-section. Second, a broadband frequency excitation completely eliminates the traditional trade-offs in IVUS imaging employing discrete frequency excitations. This broadband excitation will enable multiple identifications of the same tissue properties using different frequencies. These multiple identifications lead to significantly higher resolutions and deeper penetration depths simultaneously. This collectively, all-at-once artery wall characterization is precisely what will produce the higher-definition images from tissue property estimates

References

1.http://www.americanheart.org/downloadable/heart/1200594755071International%20Cardiovascular%20Disease%20%20Tables.pdf.

2.http://www.americanheart.org/presenter.jhtml?identifier=4478.

3. C. Christos. The Transmission-Line Modeling Method TLM. New York : John Wiley & Sons, 1995.

4. A. L. Gaster, U. Slothuus Skjoldborg, J. Larsen, L. Lorsholm, C. von Birgelen, S. Jensen, P. Thayssen, K. E. Pederson and T. H. Haghfelt: "Continued improvement of clinical outcome and cost effectiveness following intravascular ultrasound guided PCI: insights from a prospective, randomised study. " *Heart*, 2003, Vol. 89. 1043-1049.

5. C. Mueller, J.Mc. B. Hodgson, C. Schindler, A. P. Perruchoud, H. Roskamm and H. J. Buettner: "Cost-Effectiveness of Intracoronary Ultrasound for Percutaneous Coronary Interventions."*American Journal of Cardiology*, 2003, Vol. 91. 143-147.

6. P. N. Burns: "Introduction to the physical principles of ultrasound imaging and Doppler." *Fundamentals in Medical Biophysics*, 2005.

7. M. Rosales and P. Redeva: A basic Model for IVUS image simulation. Thesis, Universitat Autonoma de Barcelona, July 2005.

8. C. M. Grondin, I. Dyrda, A. Pasternac, L. Campeau, M. G. Bourassa and J. Lesperance: "Discrepancies between cineangiographic and post-mortem findings in patients with coronary artery disease and recent myocardial revascularization." *Circulation*, 1974, Vol. 49.

9. L. P. D. Ong: "Vulnerable Plaque." *Cardiovascular Research and scientific Development*. Sweidish medical center.

10. E. Regar and P. W. Serruys: "Ten years after introduction of intravascular ultrasound in the catheterization laboratory: tool or toy?" *Z Kardiol*, 2002, Vol. 91.

11. S. E. Nissen and P. Yock: "Intravascular Ultrasound : Novel Pathophysiological Insights and Current Clinical Applications." *Circulation*, 2001, Vol. 103.

12.: H. C. Stary: "Composition and classification of human atherosclerotic lesions." *Springer Berlin Heidelberg*, 1992, Vol. 421. 0945-6317.

13. H. C. Stary, A. B. Chandler, S. Glagov, J. R. Guyton, W. Jr. Insull, M. E. Rosenfeld, S. A. Schaffer, C. J. Schwartz, W. D. Wagner and R. W. Wissler: "A definition of initial, fatty streak, and intermediate lesions of atherosclerosis. A report from the Committee on Vascular Lesions of the Council on Arteriosclerosis, American Heart Association." *Circulation*, 1994, Vol. 89.

14. H. C. Stary, A. B. Chandler, R. E. Dinsmore, V. Fuster, S. Glagov, W. Jr. Insull, M. E. Rosenfeld, C. J. Schwartz, W. D. Wagner and R. W. Wissler: "A Definition of Advanced Types of Atherosclerotic Lesions and a Histological Classification of Atherosclerosis : A Report From the Committee on Vascular Lesions of the Council on Arteriosclerosis, American Heart Association." *Circulation*, 1995, Vol. 92.

15 H. Kostamaa, J. Donovan, S. Kasaoka, J. Tobis and L. Fitzpatrick: "Calcified plaque cross-sectional area in human arteries: correlation between intravascular ultrasound and undecalcified histology." *American heart journal*, 1999, Vol. 137.

16. M. P. Urbani, E. Picano, G. Parenti, A. Mazzarisi, L. Fiori, M. Paterni, G. Pelosi and L. Landini: "In vivo radiofrequency-based ultrasonic tissue characterization of the atherosclerotic plaque." *Stroke*, 1993, Vol. 24.

17. E. Picano, L. Landini,A. Distante, R. Sarnelli, L. Benassi and A. Abbate: "Different degrees of atherosclerosis detected by backscattered ultrasound: an in vitro study on fixed human aortic walls." *J Clin Ultrasound*, 1983, Vol. 11. 0091-2751.

18. R. Sarnelli, L. Landini and F. Squartini: "Atherosclerosis detection by ultrasounds. A comparative histologic study on aortic specimens." *Appl Pathol*, 1986, Vol. 4.

19. L. Landini, R. Sarnelli, E. Picano and M. Salvadori: "Evaluation of frequency dependence of backscatter coefficient in normal and atherosclerotic aortic walls." *Ultrasound in medicine & biology*, 1986, Vol. 12.

20. B. Barzilai, J. E. Saffitz, J. G. Miller and B. E. Sobel: "Quantitative ultrasonic characterization of the nature of atherosclerotic plaques in human aorta." *Circ Res*, 1987, Vol. 60.

21. M. G. M. de Kroon, L. F. van der Wal, W. J. Gussenhoven and N. Bom: "Angle-dependent backscatter from the arterial wall." *Ultrasound in medicine & biology*, 1991, Vol. 17.

22. E. Picano, L. Landini, M. P. Urbani, A. Mazzarisi, M. Paterni and A. M. Mazzone: "Ultrasound tissue characterization techniques in evaluating plaque structure." *Am J Card Imaging*, 1994, Vol. 8.

23. N. Komiyama, G. J. Berry, M. L. Kolz, A. Oshima, J. A. Metz, P. Preuss, A. F. Brisken, M. M. Paulina, P. G. Yock and P. J. Fitzgerald: "Tissue characterization of atherosclerotic plaques by intravascular ultrasound radiofrequency signal analysis: an in vitro study of human coronary arteries." *American Heart Journal*, 2000, Vol. 140.

24. M. Kawasaki, H. Takatsu, T. Noda, K. Sano, Y. Ito, K. Hayakawa, K. Tsuchiya, M. Arai, K. Nishigaki, G. Takemura, S. Minatoguchi, T. Fujiwara and H. Fujiwara: "In vivo quantitative tissue characterization of human coronary arterial plaques by use of integrated backscatter intravascular ultrasound and comparison with angioscopic findings." *Circulation*, 2002, Vol. 105.

25. M. Kawasaki, K. Sano, M. Okubo, H. Yokoyama, Y. Ito, I. Murata, K. Tsuchiya, S. Minatoguchi, X. Zhou, H. Fujita and H. Fujiwara: "Volumetric quantitative analysis of tissue characteristics of coronary plaques after statin therapy using three-dimensional integrated backscatter intravascular ultrasound." *Journal of the American College of Cardiology*, 2005, Vol. 45.

26. E. I. Cespedes, H. Ponnekanti, Y. Yazdi and X. Li. : "Elastography: a quantitative method for imaging the elasticity of biological tissues." *Ultrasonic Imaging*, 1991, Vol. 13.

27. C. L. de Korte, A. F. W. van der Steen, E. I. Cespedes, G. Pasterkamp, S. G. Carlier, F. Mastik, A. H. Schoneveld, P. W. Serruys and N. Bom. : "Characterization of plaque components and vulnerability with intravascular ultrasound elastography." *Physics in Medicine and Biology*, 2000, Vol. 45.

28. L. K. Ryan and F. S. Foster. : "Ultrasonic measurement of differential displacement and strain in vascular model." *Ultrasonic Imaging*, 1997, Vol. 19.

29. C.L. de Korte, E.I. Cespedes, A.F. van der steen, G. Pasterkamp and N. Bom: "Intravascular ultrasound elastrography: assessment and imaging of elastic properties of diseased arteries and vulnerable plaque." *European Journal of Ultrasound*, 1998, Vol. 7.

30. J. A. Schaar, C. L. De Korte, F. Mastik, C. Strijder, G. Pasterkamp, E. Boersma, P. W. Serruys and A. F. Van Der Steen: "Characterizing Vulnerable Plaque Features With Intravascular Elastography." *Circulation*, 2003, Vol. 108.

31. Y. Saijo, A. Tanaka, N. Owada, Y. Akino and S. Nitta: "Tissue velocity imaging of coronary artery by rotating-type intravascular ultrasound." *Ultrasonics*, 2004, Vol. 42.

32. B. M. Shapo, J. R. Crowe, R. Erkamp, S. Y. Emelianov, M. J. Eberle and M. O'donnell: "Strain imaging of coronary arteries with intraluminal ultrasound: experiments on an inhomogeneous phantom." *Ultrasonic Imaging*, 1996, Vol. 18.

33. C. L. de Korte, G. Pasterkamp, A. F. W. van der Steen, H. A. Woutman and N. Bom: "Characterization of Plaque Components With Intravascular Ultrasound Elastography in Human Femoral and Coronary Arteries In Vitro." *Circulation*, 2000, Vol. 102.

34. A. Koenig and V. Klauss: "Virtual Histology." *Heart*, 2007, Vol. 93.

35. A. Nair, B. D. Kuban, E. M. Tuzcu, P. Schoenhagen, S. E. Nissen and D. G. Vince: "Coronary Plaque Classification With Intravascular Ultrasound Radiofrequency Data Analysis." *Circulation*, 2002, Vol. 106.

36. E. N. Steven and Y. Paul: "Intravascular Ultrasound: Novel pathophysiological insights and current clinical applications." : *Circulation*, 2001, Vol. 103.

37. V. P. Kuznestov: "Equations of nonlinear acoustics." : *Soviet Physics - Acoustics*, 1971, Vol. 16.

38. Y. S. Lee and M. F. Hamilton : "Time-domain modeling of pulsed finite-amplitude sound beams." *Journal of the Acoustical Society of America*, 1995, Vol. 97.

39. J. Tavakkoli, D. Cathignol and R. Souchon: "Modeling of pulsed finite-amplitude focused sound beams in time domain." *Journal of the Acoustical Society of America*, 1998, Vol. 104.

40. A. Kendall and H. Weimin. Theoretical Numerical Analysis- A functional analysis framework. Springer, 2001.

41. R. B. Guenther And W. L. John. Partial differential equations of mathematical physics and integral equation. Dover, 1996.

42. J. A. Jensen: "A model for the propagation and scattering of ultrasound in tissue." Journal of the Acoustical Society of America , 1991, Vol. 89.

43. J. A. Jensen and N. B. Svendsen: "Calculation of pressure fields from arbitrarily shaped, apodized, and excited ultrasound transducers." *IEEE transcations on ultrasonics, ferroelectrics, and frequency control society*, 1992, Vol. 39.

44. R. Misael, and P. Radeva: "A basic model for IVUS image simulation." *Handbook of biomedical image analysis.* Springer Verlag GmBH, 2004.

45. I. Fontaine, M. Bertrand and G. Cloutier: "A system-based approach to modeling the ultrasound signal backscattered by red blodd cells." *Biophysical Journal*, 1999, Vol. 77.

46. D. de Cogan, W. J. O'Connor and S. Pulko. Transmission Line Matrix in Computational Mechanics. Boca Raton, Florida : Taylor & Francis, 2006.

47. U.A. Bakshi and V.U. Bakshi. Basic Electrical Engineering. India : Technical Publications Pune, 2009.

48. D.A. Al-Mukhtar and J.E Sitch: "Transmission-line matrix method with irregularly graded space." *IEE Proc,* 1981, Vol. 128, pp. 299-305.

49. T. Soderstrom and P. Stoica. System Identification. Prentice Hall, 2001.

50. K. V. Gurumurthy and R. Martin Arthur: "A dispersive model for the propagation of ultrasound in soft tissue." *Ultrasonic imaging*, 1982, Vol. 4.

51. A. C. Kak: "Signal processing of broadband pulsed ultrasound: Measurement of attenuation of soft biological tissues." *IEEE transactions on biomedical engineering*, 1978, Vol. 25.

52. L. Ljung. System identification: theory for the user. Prentice Hall, 1999.

53. M. Korenberg, S. A. Billings, Y. P. Liu and P. J. McIlroy: "Orthogonal parameter estimation algorithm for non-linear stochastic systems." *International Journal of Control*, 1988, Vol. 48.

54. S. Chen, S. A. Billings and W. Luo: "Orthogonal least squares methods and their application to non-linear system identification." *International Journal of Control*, 1989, Vol. 50.